LUND UNIVERSITY

Ultra-Wideband Wireless Channels - Estimation, Modeling and Material Characterization

Santos, Telmo

2009

Ultra-Wideband Wireless Channels

– Estimation, Modeling and Material Characterization

Thesis for the degree of Licentiate in Engineering

Telmo Santos

Dept. of Electrical and Information Technology
Lund University – 2009

Department of Electrical and Information Technology
Lund University
Box 118, SE-221 00 LUND
SWEDEN

This thesis is set in Computer Modern 10pt
with the LaTeX Documentation System

Series of licentiate and doctoral theses
No. 20
ISSN 1654-790X

Printed in Sweden by *Tryckeriet i E-huset*, Lund.
September 2009.

Aos que mais sentiram a minha falta
durante os últimos três anos.

Abstract

This licentiate thesis is focused on the characterization of ultra-wideband wireless channels. The thesis presents results on ultra-wideband communications as well as on the ultra-wideband characterization of materials.

The communications related work consisted in the measurement and modeling of outdoor scenarios envisioned for infostation systems. By infostation, we mean a communication system covering a small area, i.e., ranging up to 20 m, where mobile users can pass by or stop while receiving large amounts of data in a short period of time. Considering the expected (but perhaps overly optimistic) 480 Mbps for UWB systems, it should be possible to download a complete DVD in roughly two minutes, which is something not realizable with any of the current wireless technologies. Channel models, commonly based on measurements, can be used to evaluate the performance of such systems. We therefore, we started by performing measurements at one of the scenarios where infostation systems can exist in the future, namely, petrol stations. The idealized model, was one that could correctly describe the continuous evolution of the channel impulse response for a moving user within the system's range, and therefore it was deemed necessary to track the multipath components defining the impulse responses along a path of several meters. To solve this problem we designed a novel high-resolution scatterer detection method, which is described in Paper I, capable of tracking individual multipath components for a moving user by identifying the originating point scatterers in a two dimensional geometrical space. The same paper also gives insight on some properties of clusters of scatterers, such as their direction-selective radiated power.

The scatterer detection method described in Paper I provided us with the required tools to create the channel model described in Paper II. The proposed channel model has a geometrical basis, i.e., each realization of the channel is based on a virtual map containing point scatterers that contribute to the impulse response by multipath components. Some of the particular characteristics of the model include non-stationary effects, such as shadowing and cluster's visibility regions. At the end of Paper II, in a simple validation step, the output of

the channel model showed a good match with the measured impulse responses.

The second part of our work, documented in Paper III, consisted on the dielectric characterization of soil samples using microwave measurements. This project was made in cooperation with the Department of Physical Geography and Ecosystem Analysis at Lund University, which had been developing research work on methane emissions from the wetlands in Zackenberg, Greenland.

In recent years, a lot of attention has been put into the understanding of the methane emissions from soils, since methane is a greenhouse gas 20 times stronger than carbon dioxide. However, whereas the methane emissions from natural soils are well documented, the reason behind this effect is an open issue. The usage of microwave measurements to monitor soil samples, aims to address this problem by capturing the sub-surface changes in the soil during gas emissions. An experiment consisting on the monitoring of a soil sample was performed, and a good correlation was found between the variations of the microwave signals and the methane emissions. In addition, the soil dielectric constant was calculated, and from that, the volumetric fractions of the soil constituents which provided useful data for the elaboration of models to describe the gas emission triggering mechanisms.

Based on this laboratory experiment, a complete soil monitoring system was created and is at the time of writing running at Zackenberg, Greenland.

Preface

This thesis summarizes my research work in the Communications group of the department of Electrical and Information Technology, Lund University. The content of this thesis is based on the following publications:

[1] T. Santos, J. Karedal, P. Almers, F. Tufvesson, and A. F. Molisch, "Modeling the ultra-wideband outdoor channel – Measurements and parameter extraction method." *IEEE Transactions on Wireless Communications*, 2009.

[2] T. Santos, F. Tufvesson, and A. F. Molisch, "Modeling the ultra-wideband outdoor channel – Model specification and validation." submitted to *IEEE Transactions on Wireless Communications*, 2009.

[3] T. Santos, A. J. Johansson, and F. Tufvesson, "Dielectric characterization of soil samples by free-space microwave measurements," Series of Technical Reports, Department of Electrical and Information Technology, Lund University, no. 10, ISSN 1402-8840, September 2009.

My research activities in other projects, whose content are not included in this thesis, further resulted in the following publications:

[4] T. Santos, J. Karedal, P. Almers, F. Tufvesson, and A. F. Molisch, "Scatterer detection by successive cancellation for UWB – Method and experimental verification," in *Proc. IEEE Vehicular Technology Conference (VTC'08–Spring)*, pp. 445–449, Singapore, May 2008.

[5] S. Wyne, T. Santos, A. Singh, F. Tufvesson, and A. F. Molisch, "Characterization of a time-variant wireless propagation channel for outdoor short-range sensor networks," *IET Journal on Communications*, 2009. (in press)

[6] P. Almers, T. Santos, F. Tufvesson, A. F. Molisch, J. Karedal, and A. J. Johansson, "Antenna subset selection in measured indoor channels," *IET Microwaves, Antennas & Propagation*, vol. 1, pp. 1092-1100, October 2007.

[7] P. Almers, T. Santos, F. Tufvesson, A. F. Molisch, J. Karedal, and A. J. Johansson, "Measured diversity gains from MIMO antenna selection," in *Proc. IEEE Vehicular Technology Conference (VTC'06–Fall)*, pp. 1–6, Montreal, Canada, September 2008.

[8] S. Wyne, T. Santos, F. Tufvesson, and A. F. Molisch, "Channel measurements of an indoor office scenario for wireless sensor applications," in *Proc. IEEE Globecom*, Washington, USA, November 2007.

[9] S. Wyne, T. Santos, F. Tufvesson, and A. F. Molisch, "Measurement of small-scale fading for indoor wireless sensor networks," in *Proc. URSI*, Ottawa, Canada, July 2008.

Acknowledgments

Being a Ph.D. student at the department has been a challenging and fruitful experience. Looking back at these three years, I realize how much I have learned not only in terms of technical knowledge but also in life experience. It was very rewarding to participate in research, teaching, courses and project supervision, while interacting with so many exceptional people. While only mentioning a limited number of people in this short acknowledgment text, I would like to express my gratitude towards *all* the people that one way or the other were part of my life in Sweden.

First of all I would like thank Prof. Andreas F. Molisch, who was my main supervisor for the greater part of the time. It was an enriching experience to work with someone so knowledgeable in the field. His input to the research-related discussions was vital for the success of the final work, and his thoroughness in the writing of manuscripts taught me a lot. My admiration also goes to his ability to focus on the research being done in Sweden, while being on the other side of the globe.

My deepest gratitude also goes to my current main supervisor Dr. Fredrik Tufvesson. It was with him that I started to cooperate with the Communications group, as a Master student back in 2004, and it is to him that I owe the opportunity of enrolling at Lund University as a Ph.D. student in 2006. I thank Dr. Tufvesson for his constant support in both research and administrative matters, and for providing me with a non-stressful working environment.

I also have to thank many of my working colleagues. I thank Dr. Johan Kåredal for reminding me that it's possible to learn a foreign language in less than a year, Dr. Anders J. Johanson for teaching me how to kayak, Dr. Shurjeel Wyne for teaching me the meaning of the word "Lund" in Urdu, Dr. Peter Almers for proving that it is possible to complete a Ph.D. without working overtime (same holds true for Dr. JK), Peter Hammarberg for showing me that going from a 85°C sauna to 3°C sea water is not too bad after all, Palmi Thorbergsson for greeting me with his vast knowledge of the Portuguese language, Prof. Ove Edfors for always being available for interesting discussions, Johan

Löfgren for occasionally dropping by (i.e., everyday at 16h30), Ulrike Richter for baking such tasty cakes and cookies, Frida Sandberg for letting us go to Finn Inn twice a week, Dr. Joachim Rodrigues for providing me with quality espresso coffee during the writing of this thesis, and finally, Dr. Matthias Kamuf together with Dr. Fredrik Kristensen for always supporting me on the pitch, even though my football skills haven't improved in the last 20 years. My thankfulness also goes to the department's staff, especially Lars Hedenstjerna, Pia Bruhn, Birgitta Holmgren and Doris Glöck for always being so helpful.

A significant part of my social life in Lund was shared with another group of people to whom I would also like to show my gratitude, namely, the Portuguese gang. I thank Salome Santos for understanding how an electronic engineering guy behaves, Luís Pegado for organizing the Portuguese dinners and teaching me how to play squash, Bruno Medronho for teaching me better squash than Luís, Tiago Ferreira for giving me the chance of trying Kopi Luwak, the most expensive and probably the most disgusting coffee in the world, and Miguel Miranda for all the *more or less* scientific discussions late in the evening. I am also grateful to Çelen Cenker for always being up for a "downtown drink," and I could not forget to thank my Brazilian friends Juliana Bosco, Danilo Lima, Nádia Parachin and João Almeida for all the pleasant times spent together. Thank you all for your friendship.

Finally, I also want to acknowledge the sponsors of my Ph.D. studies, the Swedish Strategic Research Foundation (SSF) Center of High Speed Wireless Communications (HSWC) at Lund University and the Swedish Vetenskapsrådet.

While having been close to a lot of friends, I have been away from perhaps the most important persons in my life, i.e., my mother Benilde, my father Fernando, my brother Bruno and my girlfriend Inês. This thesis is dedicated to you.

Lund, September 24$^{\text{th}}$, 2009

Telmo Santos

List of Acronyms and Abbreviations

AIC	Akaike Information Criteria
BAN	Body Area Network
CDF	Cumulative Distribution Function
CDMA	Code Division Multiple Access
COST	COopération européenne dans le domaine de la recherche Scientifique et Technique
DC	Direct Current
DSO	Digital Sampling Oscilloscope
DS-UWB	Direct Sequence-Ultra-Wideband
EM	Expectation-Maximization
FCC	Federal Communications Commission
GOF	Goodness-Of-Fit
GPS	Global Positioning System
GSCM	Geometry-based Stochastic Channel Model
GSM	Global System for Mobile communications
GTD	Geometrical Theory of Diffraction
IEEE	Institute of Electrical and Electronics Engineers

IF	Intermediate Frequency
K-L	Kullback-Leibler
K-S	Kolmogorov-Smirnov
LNA	Low Noise Amplifier
LOS	Line-Of-Sight
LTE	Long Term Evolution
MB-UWB	Multiband-Ultra-Wideband
ML	Maximum-Likelihood
MPC	Multipath Component
NLOS	Non-Line-Of-Sight
PA	Power Amplifier
pdf	Probability Density Function
PEC	Perfect Electric Conductor
RF	Radio Frequency
SAGE	Space Alternating Generalized Expectation Maximization
SNR	Signal-to-Noise Ratio
S-V	Saleh-Valenzuela
ULA	Uniform Linear Array
US	Uncorrelated Scattering
USB	Universal Serial Bus
UTD	Uniform Theory of Diffraction
UWB	Ultra-Wideband
VNA	Vector Network Analyzer
WSS	Wide Sense Stationary

Contents

Part I

Overview of the Research Field

Chapter 1

Introduction

The interest on ultra-wideband (UWB) communications was initiated in the mid 90's with the pioneering work of Win and Scholtz [1, 2]. UWB-based technology had already been developed several decades before, but its use was restricted to military purposes, much like code division multiple access (CDMA) schemes. Following the interest from industry, the United States Federal Communications Commission (FCC) approved, in 2002, the unlicensed use of the frequency band between 3.1 and 10.6 GHz, and to ensure minimal interference to systems already operating within that band, FCC also defined a spectral mask limiting the power spectral density of UWB signals.

According with FCC, a signals to be UWB needs to have at least one of the two following properties: a bandwidth larger than 500 MHz (large *absolute* bandwidth) or a bandwidth 20% larger than its center frequency (large *relative* bandwidth). Signals covering the frequency band 3.1-10.6 GHz hold both these properties.

Soon after FCC's "green light" on UWB, two industry standards were formed: the IEEE 802.15.3a for *high data rates* and the IEEE 802.15.4a for *low data rates*. For high data rate applications (50 Mbps to 480 Mbps, ranging up to 10 m), UWB was envisioned for the transfer of multimedia content from different consumer electronics replacing the existing wired connections, e.g., the universal serial bus (USB) cables. Regarding low data rate applications (50 kbps to 1 Mbps, ranging up to 100 m) UWB was expected to enable precision ranging (becoming a possible solution for indoor positioning where global positioning system, GPS, does not work), body area networks including body worn sensors, see-through-wall imaging (for military and search-and-rescue purposes) and asset tracking and monitoring in industrial environments.

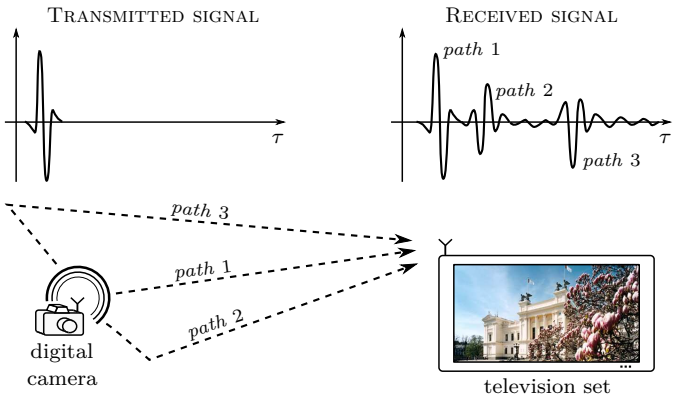

Figure 1.1: Multipath effect on ultra-wideband signals in a wireless-USB scenario. Note on the individual shape of each received multipath component, a unique characteristic of UWB.

The natural reaction from industry came in 2003 with the formation of several "start-ups" aiming to bring UWB products into the market.

From a propagation perspective, UWB also presented several challenges since many of the assumptions made for narrow- and wideband signals could not be taken for granted anymore. Such assumptions include the frequency-flat description of the multipath components (MPC), the wide sense stationary uncorrelated scattering (WSS-US) assumption [3], and the validity of the central limit theorem when describing small-scale fading. The need for the verification of the above assumptions, together with the fact that the existing channel models could not be used to describe the new target scenarios, initiated a wave of channel measurements and modeling from both industry and academia. Such research efforts are still ongoing. A comprehensive review of measurements and their results can be found in [4].

Fig. 1.1 illustrates the multipath effect of UWB communication systems. The plots in the upper part of the figure show one of the distinctive properties of UWB signals propagating in a wireless channel, namely, the individual pulse distortion of the multipath components.

The growth of UWB technology has faced many hurdles despite all the initial optimism. First, in 2006, two proposals were competing for the physical layer of the IEEE 802.15.3a standard, one supported by the UWB Forum based on Direct Sequence UWB (DS-UWB), and the second proposal backed by the WiMedia Alliance based on Multi-Band Orthogonal Frequency Division Multiplexing (MB-OFDM) UWB. The discussions between the two groups entered a

period of stalemate lasting several months, after which the standardization activities were canceled. The UWB Forum stopped, while the WiMedia Alliance proceeded with its activities in the specification of a physical and media layers, which became adopted by both Bluetooth 3.0 and Wireless USB. However, the WiMedia Alliance has recently announced that it will transfer the current and future specifications to its industry partners, after which it will cease operations. Adding to this, several of the 2003 "start-up" companies have not been able to introduce their products into the market and some of them have actually closed down, e.g., WiQuest Communications in 2008, and most recently, Tzero Technologies in 2009, revealing that the expected widespread adoption has not become a reality yet.

The future of UWB may, however, not be as dark as it seems. The technology of UWB chipsets improved and their prices are constantly dropping. In addition, the worldwide authorization of the spectrum started in 2002, has finally been completed. In another front, UWB at 60 GHz for high throughput in line-of-sight scenarios appears be gathering a lot of interest. The European Union has recently approved the use of spectrum between 57 GHz and 66 GHz [5]. If these factors converge, UWB will definitely have the chance to deliver what it was envisioned for, and finally establish itself as a long lasting technology.

The reminder of the Part I of this thesis is organized as follows. Chapter 2 discusses the unique properties of UWB in relation to both narrowband and wideband systems. Chapter 3 is dedicated to the description of channel measurement techniques, giving some insight on antenna distortions. Chapter 4 presents the parameter estimators used in our work and describes two statistical model selection approaches. Finally, Chapter 5 summarizes the content of the three included papers in Part II.

Chapter 2

Ultra-Wideband Channel Characteristics

THE MAIN PURPOSE of any communication system is to convey a message from the transmitter to the receiver. In the case of digital communication systems, the message to be sent is initially described by a group of information bits, which are then mapped into some type of physical signal to enable the transmission. The medium over which the message is transmitted is designated as "channel." In the delay-domain, the received signal, $y(\tau)$ is related with both the transmitted signal, $x(\tau)$, and the channel impulse response, $h(\tau)$, by the convolution operation, such that the input-output relation of the system can be described by

$$y(\tau) = h(\tau) * x(\tau) + n(\tau) \tag{2.1}$$

where $n(\tau)$ denotes the receiver noise. Due to channel limitations, and the need for simultaneous transmission of different messages over the same channel, signals are usually modulated onto specific carrier frequencies before transmission. Such transmitted signals are denoted band-pass signals.

From an analytical perspective, it is cumbersome to describe the input-output relation in the *real* band-pass form, and therefore the signals in (2.1) are commonly specified in their *complex* base-band equivalent form.[1] The relation between the real band-pass and complex base-band domains is given by $x_{\text{real}}(\tau) = \text{Re}\left\{x(\tau)e^{j2\pi f_c \tau}\right\}$, where f_c is the carrier frequency.

[1]The need for complex signals stems from the fact that band-pass signals can have both an *in-phase* and a *quadrature* component, which base-band signals cannot.

In this chapter we describe the properties of the channel impulse response $h(\tau)$, more specifically we focus on how its properties vary with the bandwidth [6]. Strictly speaking, the channel is not influenced by the bandwidth, as a physical channel does not depend on the signals that propagate through it. However, we are only interested in the part of the channel within the same bandwidth as the transmitted signal, since only this part actually plays a role. It is therefore common practice to refer to the "channel where UWB signals propagate," as the "UWB channel."

2.1 Channel Bandwidth

The different mathematical models used to describe the impulse response $h(\tau)$ for the different bandwidths are presented in this section in their most general form. Fig. 2.1, shows a representation of the same wireless channel for three different transmission bandwidths (solid lines), in both the frequency and the delay domain. The dashed lines represent the true channel behaviour, i.e., over a segment of very large bandwidth. The vertical and horizontal arrows indicate the strength of the amplitude and delay variations of the channel delay taps,[2] respectively, caused by the movement of one of the antennas in a small-scale area, i.e., an area within which the amplitude of each MPC does not vary significantly.

2.1.1 Narrowband

Narrowband systems are flat over frequency, as illustrated in Fig. 2.1a, such that their impulse response can be simply defined by a complex coefficient α, and a delay τ_0 as

$$h_{\text{NB}}(\tau) = \alpha\delta(\tau - \tau_0). \tag{2.2}$$

The delay resolution (inverse of the bandwidth) of narrowband systems is very small, and therefore no individual MPCs can be resolved (here, each MPC is characterized by an amplitude and phase, and is considered to be flat over frequency as well). Thus, all MPCs contribute to α, which can make $|\alpha|$ to vary strongly within a small-scale area. On the other hand, the variations of the delay τ_0 within the same area, are so small in proportion to the delay resolution, that they are always neglected.

An example of a narrowband communication system was the nordic mobile telephony NMT-900, which used 25 kHz of bandwidth.

[2]The terms "delay tap" and "resolvable MPC" are used interchangeably throughout the text.

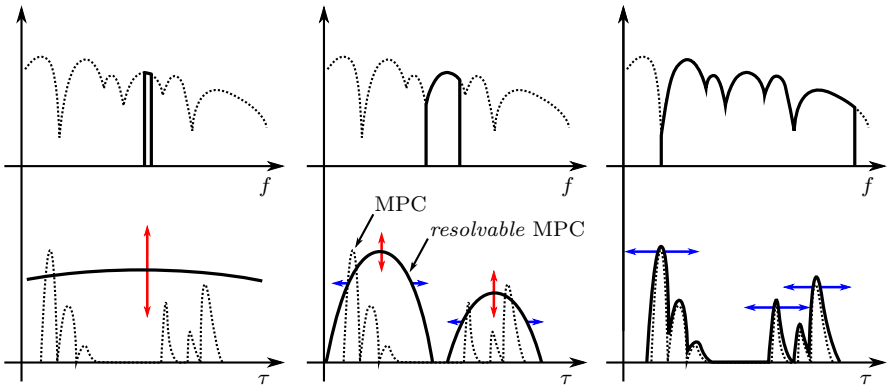

(a) Narrowband **(b)** Wideband **(c)** Ultra-wideband

Figure 2.1: Representation of the frequency-domain (upper plots) and delay-domain (lower plots) of the wireless channel for different bandwidths. The solid lines correspond to the different band-limited channels and the dashed lines correspond to the hypothetical infinite bandwidth channel. The arrows indicate the variations experienced by the channel when one of the antennas is moved.

2.1.2 Wideband

For wideband systems, the profile of the frequency spectrum varies significantly and cannot be considered flat (it is said to be frequency-selective), see Fig. 2.1b. This varying frequency-response is translated into a delay dispersive impulse response which can be described by a tapped delay line representation as

$$h_{\mathrm{WB}}(\tau) = \sum_{k=1}^{L} \alpha_k \delta(\tau - \tau_k), \tag{2.3}$$

where α_k is the complex amplitude of the k:th *resolvable* MPC and τ_k the corresponding delay (Fig. 2.1b shows two resolvable MPCs). The amplitude variations of α_k can still be large, however, the number of MPCs contributing to each α_k is less than for the narrowband case. It then becomes more likely that one of the MPCs dominates over the remaining ones, resulting in smaller amplitude variations. Due to the increase in delay resolution, variations of the antenna position will translate into variations of τ_k. However, even in the wideband case, these are small and most commonly ignored. The resolvable MPCs are still considered to be frequency flat.

Table 2.1: Comparison of the channel characteristics for different bandwidths.

	Delay resolution	No. of MPCs per tap	Small-scale fading per tap	MPC's frequency
Narrowband	low	large	large	flat
Wideband	medium	medium	medium	flat
Ultra-Wideband	high	small	small	selective

An example of a wideband communication system is Long Term Evolution (LTE) which can use a bandwidth up to 20 MHz. LTE-Advanced is expected to reach 100 MHz, but it still falls within the wideband category.

2.1.3 Ultra-Wideband

Channels having an ultra-wide bandwidth, as illustrated in Fig. 2.1c, have unique properties. Besides the frequency variations of the "complete" channel, each resolvable MPC is frequency selective as well, and to account for this *per-path* distortion, the channel must be described as

$$h_{\text{UWB}}(\tau) = \sum_{k=1}^{N} \alpha_k \chi_k(\tau) * \delta(\tau - \tau_k), \tag{2.4}$$

where $\chi_k(\tau)$ is the distortion function of the k:th resolvable MPC. The causes of the frequency variations are explained in detail in Section 2.2. In UWB systems, the small-scale variations of the amplitude of a resolvable MPC, are expected to be much smaller than for the above described systems due to its fine delay resolution. However, to correctly measure the amplitude variations of each resolvable MPC becomes a challenge since small variations of the antenna position will translate into large variations of τ_k in proportion to the delay resolution, making it difficult to track the exact delay of each MPC. Our scatterer detection method, described in Paper I, is able to track individual MPCs for a moving antenna.

Table 2.1 qualitatively summarizes the characteristics of the different band limited channels.

2.2 Frequency Dependence

The understanding of the frequency dependence of single MPCs is important from a channel description perspective because such MPCs become smeared

in the delay domain, possibly leading to correlation between the delay taps, which may in turn, violates the uncorrelated scattering (US) assumption. The frequency dependence of a single MPC can be caused by different propagation effects. In the following subsections, five of these effects are described and corresponding example expressions are given.

2.2.1 Free-Space Path Loss

In the case of two antennas transmitting in free-space, assuming that the antennas are lossless and matched in both impedance and polarization, the power at the receiver antenna, P_{Rx}, is well described by Friis's law as [7]

$$P_{\mathrm{Rx}}(f) = \frac{P_{\mathrm{Tx}}(f)G_{\mathrm{Tx}}(f)G_{\mathrm{Rx}}(f)}{L_0(f)}. \tag{2.5}$$

Here, P_{Tx} is the transmitted power, G_{Tx} is the gain of the transmitter antenna and G_{Rx} is the gain of the receive antenna. The free-space path loss is

$$L_0(f) = \left(\frac{4\pi f d}{c_0}\right)^2 \tag{2.6}$$

where c_0 is the speed of light in vacuum and d is the distance between the antennas. The variations of the received power over frequency are dependent on all four components of (2.5), and in some cases, it is even possible for all the frequency dependent terms to cancel out. For example, assuming constant transmit power, if the transmitter antenna has constant *gain* (e.g., a small electric-dipole) and the receiver antenna has constant *aperture* (e.g., a horn antenna) then the received power will also be constant over frequency [8]. Frequency independent received power is of course desirable. However, when it comes to mobile applications, it is not feasible to have the antennas facing each other at all times, and therefore constant gain antennas are chosen instead of the constant aperture ones, for both link ends. In this case, the received power follows the $1/f^2$ roll-off factor from the free-space path loss.

2.2.2 Dielectric Layer Transmission and Reflection

Dielectric materials influence both the attenuation and the propagation speed of electromagnetic waves. Real propagation scenarios often include layered materials, e.g., wooden doors, concrete walls and glass windows, and therefore the transmission through, and reflection of, dielectric layers becomes of interest when evaluating and modeling propagation effects. The transmission coefficient

through a dielectric layer of length L surrounded by air is defined by [9]

$$\mathrm{S}_{\mathrm{Tra}}(f) = \frac{\left(1-R^2\right)e^{-L\gamma(f)}}{1-R^2e^{-2L\gamma(f)}} \tag{2.7}$$

and the corresponding reflection coefficient is [9]

$$\mathrm{S}_{\mathrm{Ref}}(f) = \frac{\left(1-e^{-2L\gamma(f)}\right)R}{1-R^2e^{-2L\gamma(f)}}. \tag{2.8}$$

The function $\gamma(f)$, is related with the dielectric constant $\varepsilon_r(f)$ by

$$\gamma(f) = \frac{2\pi f}{c_0}\sqrt{-\varepsilon_r(f)}. \tag{2.9}$$

and R is defined as in Paper III. Equation (2.9) shows that $\gamma(f)$, and therefore also $\mathrm{S}_{\mathrm{Tra}}(f)$ and $\mathrm{S}_{\mathrm{Ref}}(f)$, vary with frequency even if ε_r does not. When looking at the properties of common building materials, ε_r has been found to be constant over the whole FCC allowed UWB bandwidth in the case of glass and wallboard, but shows variations in the case of wooden doors, cement and construction bricks [10, 11]. Humid or wet materials have a non-constant ε_r over frequency, since the dielectric properties of water vary largely with the considered band as is shown in Paper III.

The transmission and reflection coefficients can be measured by frequency domain techniques (see Section 3.2), which provide a way to determine the dielectric constant of unknown sample materials. This was the approach used in Paper III.

2.2.3 Diffraction

Diffraction effects are also dependent on frequency. Various diffraction models can be used to describe these propagation phenomena. Since the wavelength of the FCC allowed UWB frequencies (which ranges from 28 mm to 96 mm) is generally much smaller than the objects causing the diffraction, e.g., corner walls, it is reasonable to use high-frequency approximations as the geometrical theory of diffraction (GTD) or the uniform theory of diffraction (UTD). GTD describes in a rigorous way the diffracted rays emanating from edges and corners, but it is unable to describe the field at the shadow boundaries [12]. UTD was proposed in order to correct this shortcoming, providing field continuity also on the transition zones [13]. Since UTD is analytically more complex than GTD, and both theories converge beyond the boundary zones, GTD can still be used in those regions. We here show a simple example of the diffracted field

behind a perfect electric conductor (PEC) screen based on GTD [12]

$$E_{\mathrm{d}}(f) = E_{\mathrm{inc}} \left[\frac{1}{2} - \frac{e^{j\pi/4}}{\sqrt{2}} F\left(-\frac{2y}{\sqrt{c_0 x/f}} \right) \right] \quad x > 0. \tag{2.10}$$

Here, E_{inc} is the horizontally propagating incident field on the vertical screen, x and y are the horizontal and vertical Cartesian coordinates with origin at the screen edge, and F(.) is the Fresnel integral, which contains the frequency dependence as its argument, given by

$$F(u) = \int_0^u e^{-ju^2\pi/2} du. \tag{2.11}$$

2.2.4 Rough Surface Scattering

A rough surface is considered to be a surface with small-scale random fluctuations on the local height. In cases when the surface height can be well described by a Gaussian distribution, the scalar reflection coefficient of the rough surface becomes [12]

$$R_{\mathrm{r}}(f) = R_{\mathrm{s}} e^{-2[2\pi(f/c_0)\sigma \sin(\phi_0)]^2} \tag{2.12}$$

where ϕ_0 is the angle of incidence on the surface, σ is the standard deviation of the surface height and R_{s} is the reflection coefficient for the corresponding smooth surface.

2.2.5 Realistic Example of Frequency Dependence

In order to visualize the amount of frequency distortion caused by each one of the above described propagation effects, realistic parameters were chosen for each expression and the results plotted in Fig. 2.2. To facilitate the comparison, all curves were normalized to their maximum magnitude. The figure also shows a representation of the three different bandwidth systems, from which it is clear why the frequency variations over narrowband and wideband systems are commonly neglected; only ultra-wideband systems experience significant frequency variations. The propagation effects and the corresponding parameters[3] used in Fig. 2.2 are as follows.

- $1/L_0(f)$ – Free-space path-gain.
- $S_{\mathrm{Tra}}(f)$ – Transmission through a layer of bricks with 15 cm of width (dielectric constant of bricks taken from [11]).

[3]The parameters that only affect the mean power are not listed since their influence is lost in the normalization.

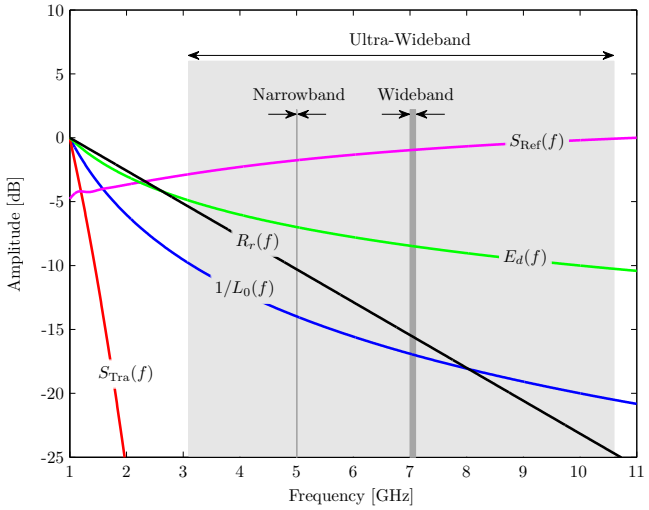

Figure 2.2: Example of frequency variations for different propagation effects: $1/L_0(f)$ free-space path-gain, $S_{\mathrm{Tra}}(f)$ transmission through a layer of bricks, $S_{\mathrm{Ref}}(f)$ reflection of a layer of bricks, $E_{\mathrm{d}}(f)$ diffraction behind a PEC screen and $R_r(f)$ rough surface scattering. The considered bandwidths are: 1 MHz narrowband, 100 MHz wideband and 7.5 GHz ultra-wideband.

- $S_{\mathrm{Ref}}(f)$ – Reflection of a layer of bricks with 15 cm of width (dielectric constant of bricks taken from [11]).
- $E_{\mathrm{d}}(f)$ – Diffraction behind a screen at coordinates $(x, y) = (2, -2)$ m.
- $R_r(f)$ – Rough surface scattering considering an incidence angle of $\phi_0 = \pi/4$ and a standard deviation of the surface height of $\sigma = 1$ cm.

2.3 Bandwidth Effect on Fading Statistics

As shown in Section 2.1, an increase of bandwidth can[4] decrease the number of MPCs per delay tap (i.e., per resolvable MPC) and therefore influence the small-scale fading statistics. Figs. 2.3a and 2.3b, show the impulse responses

[4]The word "can" is used here because the decrease of the number of MPCs per delay tap depends from channel to channel, e.g., if in a given narrowband channel there is only one MPC per delay tap, then, even with a wider bandwidth, there will still be only one MPC per delay tap.

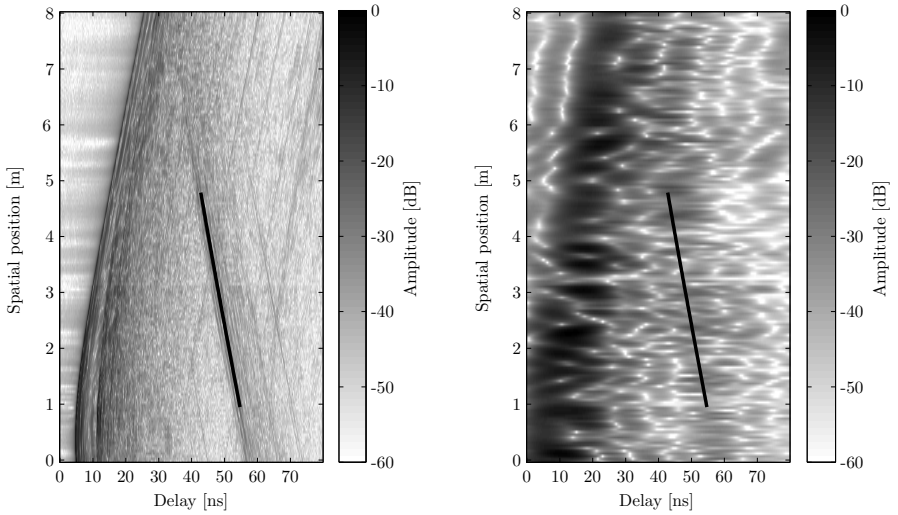

(a) Ultra-wideband: 7500 MHz **(b)** Wideband: 100 MHz

Figure 2.3: Impulse responses of the same measured channel for two different bandwidths. The black line indicates the tracked MPC used in the small-scale statistic analysis in Fig. 2.5.

of the same measured channel considering a bandwidth of 7500 MHz (ultra-wideband) and 100 MHz (wideband), respectively. Each horizontal line in the figures corresponds to the impulse response at a given receiver antenna position for the same transmitter antenna position. The antennas had line-of-sight (LOS) at all measured positions.

A direct consequence of the different bandwidths, is that the impulse responses in Fig. 2.3b show a much smoother profile than the ones in Fig. 2.3a. When looking at the first arriving resolvable MPC, i.e., the LOS component, the ultra-wideband impulse response shows a well defined MPC, whose amplitude decays monotonically for increasing spatial position (this is reasonable since the receiver antennas was being moved away from the transmitter antenna). When looking at the wideband channel, this is no longer true. The LOS component shows large amplitude variations along the different spatial positions, due to the interference of the different MPCs at early delays. The interference is said to be *constructive* when the constituent MPCs have similar phases (as is the case at spatial position 0 m) or *destructive* when the MPC phases are different (as is the case at spatial position 3.25 m). Actually, the

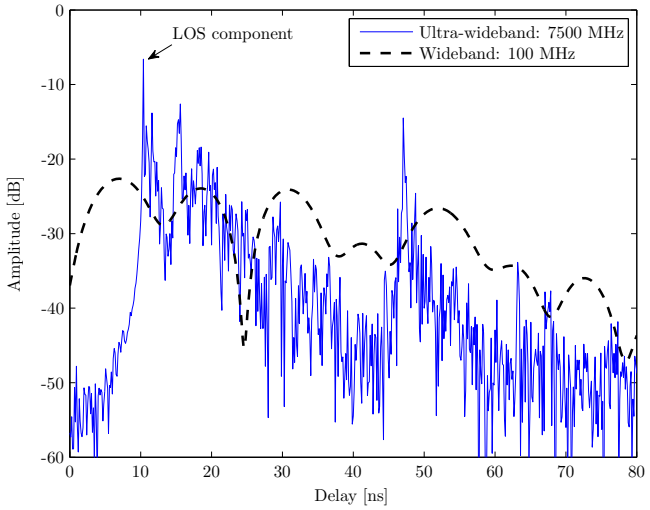

Figure 2.4: Impulse response of the same channel (spatial position 3.2 m from Fig. 2.3) for two different bandwidths.

impulse response at 3.25 m, given in detail in Fig. 2.4, can barely be seen to have a LOS component at all.

We now focus our attention to the statistical description of the amplitude variations. A specific MPC was chosen from the ultra-wideband channel and tracked through the different spatial positions (the chosen MPC is marked by a black line in Figs. 2.3a and 2.3b). In order to track the MPC, we used the scatterer detection algorithm described in our Paper I, and the corresponding envelope amplitudes were compensated from large-scale variations by means of an average sliding window (also explained in Paper I).[5] The resulting empirical cumulative distribution function (CDF) of the envelope amplitudes are depicted in Figs. 2.5a and 2.5b, for the ultra-wideband and wideband case, respectively. In addition, the amplitudes were also fitted to the Rayleigh and Rician distributions, and the corresponding CDFs plotted in the same figures.[6] Comparing the figures, it is clear that for the ultra-wideband case the amplitudes are well described by a Rician distribution indicating the presence of only one strong MPC and possibly several weak ones, while for the wideband case,

[5]Such amplitude compensation is necessary since the following statistical analysis requires the data to be stationary, i.e., the statistical properties of the data, including the mean, must not change.

[6]The parameters of both distributions were found using the maximum-likelihood estimators described in Section 4.2.

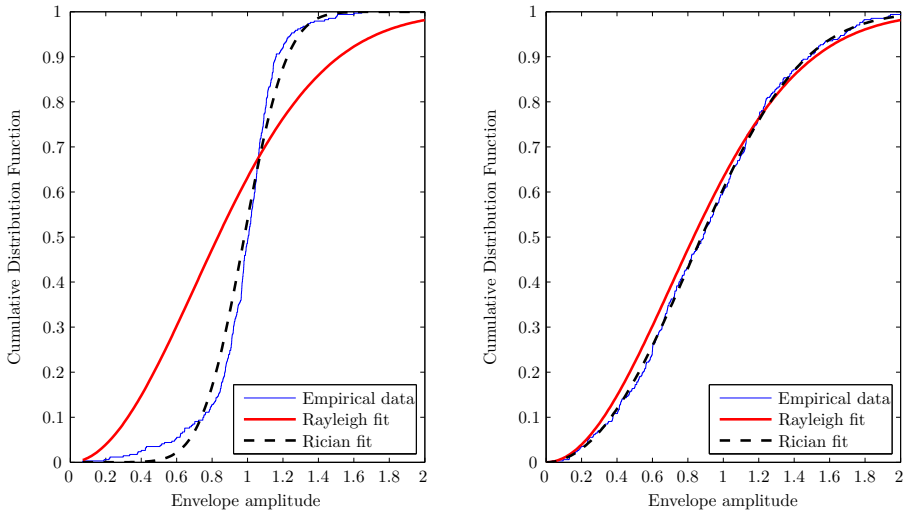

(a) Ultra-wideband: 7500 MHz **(b)** Wideband: 100 MHz

Figure 2.5: Empirical CDFs of the amplitudes extracted from the MPC indicated in Fig. 2.3, using 360 data points. The corresponding Rayleigh and Rician distribution fits are also shown.

the amplitude variations approach the Rayleigh distribution, indicating the interference between several MPCs (which could not be separated/resolved) with similar strengths.

2.4 Signal Processing for UWB: Beamforming

The distinctive propagation characteristics of ultra-wideband also influence the signal processing required at both transmitter and receiver. In this section, we give an example of the signal processing needed to transmit (or reciprocally, receive) a signal in a certain direction, assuming multiple antennas. We consider the uniform linear array (ULA) case, where the antennas are equally spaced along a specific direction.

For narrowband systems, beamforming a signal $s(t)$ in a specific direction ϕ from the array, is achieved by applying *steering phases* to $s(t)$ before the antennas elements. This can be interpreted as a frequency-domain approach since the steering phases affect the phase of the carrier frequency. In accordance, the signal transmitted from the n:th antenna (using complex base-band

representation) is defined as in [14] by

$$x_n(t) = s(t)e^{jn\theta_\phi}, \quad n = 1, \ldots, N_{\text{TX}} \tag{2.13}$$

where N_{TX} is the total number of antennas and the steering phase θ_ϕ is defined geometrically from the beamforming angle ϕ by

$$\theta_\phi = 2\pi \frac{d}{\lambda} \sin \phi. \tag{2.14}$$

Here, d is the distance between the antennas and λ is the wavelength of the carrier frequency.

In ultra-wideband systems, specially in the case of impulse based communications systems with large relative bandwidths, there is no single carrier frequency, and therefore the beamforming approach of (2.13) cannot be used. A possibility is to divide the spectrum in subbands and use (2.13) for the center frequency of each one of those subbands considering a common time reference, but such would result in increased complexity. The time-domain approach of beamforming is more suitable for ultra-wideband. This consists of using *steering delays* instead of steering phases, such that the signal transmitted from the n:th antenna is defined as in [15] by

$$x_n(t) = s\left(t + n\tau_\phi\right), \quad n = 1, \ldots, N_{\text{TX}} \tag{2.15}$$

where the base delay τ_ϕ is defined geometrically from the beamforming angle ϕ as

$$\tau_\phi = \frac{d}{c} \sin(\phi) \tag{2.16}$$

Here, c is the speed of light in vacuum.

2.5 Channel Models for Wireless Communications

The impulse response of a wireless channel is usually a product of several wave propagation effects such as path-loss, reflection, transmission, diffraction and scattering, and many of these effects can only be explained by derivations of Maxwell's equations. It then becomes impractical to find models that describe all these effects exactly. In addition, not all the propagation effects may be relevant for a communication system, e.g., a multipath component from a far scatterer with 1000 times less power than the line-of-sight component cannot be considered to affect the performance of the system. There is much more information on the physical environment where waves propagate, than what is actually necessary to describe the impulse response. Channel modeling does

therefore not necessarily seek an exact description, but rather a *relevant* description of the channel.

Channel models should also be simple enough to enable their implementation, since complicated models are less attractive from a usability point of view. A good model is therefore one that finds a good compromise between accuracy and simplicity.

2.5.1 Stochastic Channel Models

The first complete mathematical framework capable of describing the variations over delay and time of wireless channels was proposed by Bello in 1963 [3]. His work was based on two assumptions, the wide sense stationarity (WSS), referring to the time-invariant statistics of the delay taps, and the uncorrelated scattering (US) referring to the statistical independence between different delay taps. Bello's model remains to date the most widely accepted model for wireless communications and the majority of the channel modeling work is, one way or the other, based on it, e.g., the COST 207 used for GSM (well explained in [16]) and the more recent IEEE 802.15.3a UWB channel model.

The mentioned models all fall in the category of stochastic channel models, since their parameters are described by random variables. These models are however only valid within a stationarity region, or more specifically, they do not describe the transition (non-stationary phase) from one stationarity region to another.

2.5.2 Geometry-Based Stochastic Channel Models

A useful approach to describe non-stationary effects is to introduce geometry into the model, i.e., to use a so called geometry-based stochastic channel model (GSCM). Most commonly, GSCMs as the one we propose in Paper II, are based on a geometrical map where the scatterer positions and scatterer powers are chosen randomly. Then, the MPCs of scatterers are summed up at the receiver by means of a simplified ray-tracing to form the impulse response. GSCMs have gained popularity in novel channel modeling areas as vehicle-to-vehicle communications [17, 18]. An example of a standardized channel model with a geometrical basis is the recent 3GPP Spatial Channel Model (SCM) used for LTE [19].

2.5.3 Standardized Models for Ultra-Wideband

As mentioned before, there are two standardized channel models for UWB, the IEEE 802.15.3a model and the IEEE 802.15.4a model. Though the standards

were designed for high-speed and low-speed communications, respectively, both channel models can be used to simulate any data rate, since a channel is not dependent on the characteristics of the system operating on it [6].

Both models are based on the Saleh-Valenzuela (S-V) model,[7] however, 802.15.3a uses the classical version [20], and 802.15.4a uses a generalized version, i.e., with generalized description of path-arrival times and path-gains. The parameters for the SV models were extracted from measurements. The 802.15.3a model was developed first, in 2003, and it was based in measurements at office and residential indoor scenarios, covering a range of up to 10 m [21]. The 802.15.4a model was developed later and was based on more measurements covering larger distances at more scenarios, i.e., residential indoor, office indoor, industrial, outdoor and farm environments [22].

It is important to note that 802.15.3a does not include per-path distortion, and 802.15.4a assumes the same per-path distortion for all paths.

[7]Not all the modeled environments in 802.15.4a use the S-V model, i.e., industrial non-LOS and office non-LOS use a dense channel model with a "soft onset" of the power delay profile [6].

Chapter 3

Channel Measurements

Channel measurements are generally the basis for channel models. Strictly speaking, channel models do not exclusively require measurements, but it is a fact that all standardized models are derived from measurements. Furthermore, the model design and the planning of measurements are interconnected tasks which should be made in agreement with each other.

When it comes to the interpretation of the measured data, it is also important to note that measurements are not perfect, they contain errors and may depend on the measurement equipment. Care should therefore be taken in order not to incorporate these errors into the model. However, it is often not possible to achieve such a task completely, in which case the effects can at best be reduced.

In the remainder of this chapter we describe the different channel measurement techniques and make some comments regarding equipment and antennas.

3.1 Time-Domain Measurements

Time-domain measurements consist of the transmission of short pulses[1] from a pulse generator, and the recording of the received signal voltage by a digital sampling oscilloscope (DSO). This measurement technique has the advantage of being very fast, enabling the measurement of rapid changing channels. The drawback comes from the difficulty of generating short pulses with enough power to achieve good received signal quality, i.e., high signal to noise ratio (SNR). In such cases, there are two alternative means to increase SNR, either

[1] in the order of a few tenths of nanoseconds for the UWB case

Table 3.1: Time domain vs Frequency domain channel sounding.

	Time domain (DSO)	Frequency domain (VNA)
Tx-Rx synchonization	difficult	easy
Measurement duration	short	long
Calibration	difficult	easy

the measurement is repeated several times and averaged, loosing the initial advantage of being very fast, or power amplifiers and low noise amplifiers are used before the transmitter and receiver antennas, respectively.

A more sophisticated measurement technique is the one used in correlative sounders. Here, the transmitter sends a sequence of pulses with good auto-correlation properties, and the receiver calculates the cross-correlation between the transmitted and received signals. However, it is also worth mentioning that generating wideband sequences with good correlation properties can be a challenge in itself.

Other disadvantages of time-domain measurements include the synchronization of transmit and receive units, since these are generally separated. In addition, the calibration of the frequency distortions introduced by the cables, amplifiers and transmitted pulse, is difficult since this requires the deconvolution operation.

3.2 Frequency-Domain Measurements

Frequency-domain measurements are commonly performed with a vector network analyzer (VNA). This equipment transmits pure sinusoidal signals instead of pulses, and calculates the real and imaginary parts of the received sinusoid by comparing it with the transmitted reference. The measurements become considerably slower than the time-domain ones since each frequency point is measured separately, limiting its applicability for fast changing channels. The time taken to measure each frequency is set by the intermediate frequency (IF) bandwidth.[2] By decreasing the IF bandwidth it is possible to increase the measurement's SNR, since each frequency is measured for a longer time.

This approach presents several advantages too, e.g., a flexible measured bandwidth, simpler synchronization (since the transmitter and receiver are usually implemented in the same unit) and simpler calibration of cables, amplifiers and VNA distortions. The calibration is usually available as an internal option

[2] An IF bandwidth of 100 Hz corresponds roughly to 100 measured frequencies per second.

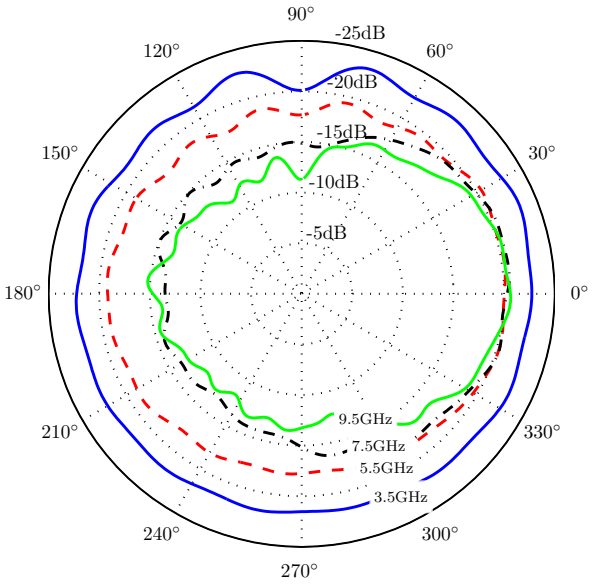

Figure 3.1: Radiation pattern of SkyCross SMT-3TO10M-A in the azimuthal plane with vertical polarization.

of the VNA.

Frequency domain measurements were used in all our contributions, i.e., Papers I, II and III. A list comparing the characteristics of both time-domain and frequency domain measurements is provided in Table 3.1.

3.3 Ultra-Wideband Antennas

Even though frequency domain measurements have the advantage of being easy to calibrate, the VNA calibration procedure is not able to correct for the influence of the antenna pattern. UWB antennas have radiation patterns characterized by a complex coefficient for each direction and for each frequency, which in the time domain translates into the radiation of different pulses in different directions (once again, a characteristic unique to UWB).

The elimination of the antenna effects from measured data is still possible by means of maximum-likelihood parameters estimation algorithms as the UWB-SAGE [23], however, these algorithms require the complete knowledge of the complex antenna pattern. In our work, we only had access to the *amplitude*

information of the radiation pattern of the antennas, as the *phase* information was available, and for this reason, no attempts were made to compensate for the antenna effects. Nevertheless, the antennas used in the measurements, SkyCross model SMT-3TO10M-A, have a approximately flat radiation pattern in the azimuthal plane, as can be seen from Fig. 3.1. The radiation pattern shows no "dips," and from 3.5 to 9.5 GHz there is, at most, a difference of 10 dB in the radiated power.

3.4 Antenna Effects on UWB Pulses

Antennas are well known to have differentiation effects on the voltage signals fed to them, e.g., the radiated fields from a small electric-dipole antenna have a time dependence proportional to the second time derivative of the voltage signal [8]. This effect if often neglected for narrowband signals since the derivative of a sinusoid does not change the signal's shape, it only introduces a $\pi/2$ phase-shift. Furthermore, a second derivative of sinusoids leads to a phase-shift of π, which simply corresponds to an inversion of polarization. UWB signals, on the other hand, are significantly changed when fed to UWB antennas.

In order to understand how much our antennas distorted the transmitted signals, test measurements were done using a DSO (Tektronix DPO 71604) and a pulse generator (Picosecond 4015D). We started by measuring the transmission of the generated pulse through only RF cables, see Fig. 3.2a.[3] Then, an amplifier was added after the cables, which changed the initial signal by adding a positive excursion after the main negative one, see Fig. 3.2b. The similarity between the measured signal with the amplifier, and the derivative of the signal in Fig. 3.2a evaluated numerically, and also shown in Fig. 3.2b, reveal that the amplifier has a derivative effect. Finally, we added two SkyCross antennas to the setup, see Fig. 3.2c. The antennas were positioned at a distanced of half a meter, face-to-face, an in an environment without scatterers within a radius of two meters. Similarly to the amplifier, and contrary to the small electric-dipole antenna [8], the SkyCross antennas appear to derivate the signals fed to them only once, as can be seen by comparison with the dashed line in the same figure.

[3]It is worth mentioning that the pulse in Fig. 3.2a could never be radiated in free-space since it is impossible to radiate DC signals, i.e., the complete time integral of a radiated waveform must be equal to zero [8].

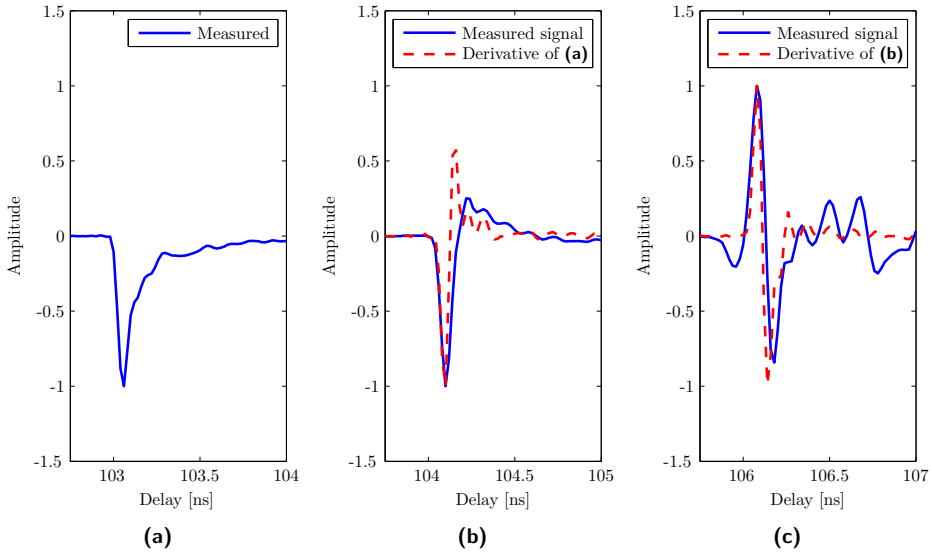

Figure 3.2: Received UWB pulse after propagating through (a) cables, (b) cables and amplifier, and (c) cables, amplifier and antennas. The dashed lines are derivatives for the solid lines on the corresponding plot to the left.

Chapter 4

Parameter Estimation and Model Selection

PARAMETER EXTRACTION can be described as the task which stands between the measurements and the actual definition of a channel model. A model is specified by parameters that need to be estimated from measured data, which makes the extraction dependent on the modeling approach. As an example, for a Saleh-Valenzuela based model some of the parameters that need to be estimated are the number of clusters, the number of MPCs per cluster and their powers. Stochastic channel models often require the estimation of the parameters defining amplitude distributions and the selection of the most suitable statistical distributions.

More complex channel models that include directional information of MPCs require more advanced parameter extraction methods based on multiple antennas or virtual arrays. We have proposed one such method in Paper I, and pointed out the fundamental differences between our method and the two most popular high-resolution methods that are able to extract the directional information of MPCs for UWB channels, the Sensor-CLEAN [24] and the UWB-SAGE [23].

4.1 Statistical Modeling of Small-Scale Fading

In this section, we describe the most popular statistical distributions used to describe amplitude variations in wireless channels. While the pdfs of the following distributions can be found in any good statistics book, the corresponding maximum likelihood (ML) estimators are difficult to find, and therefore we

present them both here (ML estimators described in the next section) with the purpose of creating a reference document for future work.

4.1.1 Rayleigh Distribution

Rayleigh distributed amplitudes appear when a large number of MPCs with independent phases and similar powers add up together. The Rayleigh pdf is defined for $x > 0$, as

$$f_{\text{Rayleigh}}(x) = \frac{x}{\sigma^2} e^{-\frac{x^2}{2\sigma^2}} \tag{4.1}$$

where the only parameter is the variance σ^2.

4.1.2 Rician Distribution

Rician distributed amplitudes appear when on the top of a large number of weak and independent MPCs, there is additionally a stronger dominant MPC. The Rician pdf is defined for $x > 0$, as

$$f_{\text{Rician}}(x) = \frac{x}{\sigma^2} e^{-\frac{x^2+\mu^2}{2\sigma^2}} I\left(0, x\frac{\mu}{\sigma^2}\right) \tag{4.2}$$

where the two parameters are μ and σ^2, and I is the 0:th order modified Bessel function of the first kind. The Rician distribution is also commonly described a function of the ratio of powers of the dominant component and the random (or Gaussian) component, $\mu^2/(2\sigma^2)$, so called k factor [7].

4.1.3 Log-Normal Distribution

The log-normal distribution is commonly applied to model multiplicative fading, as is the case of MPCs resulting from multiple interactions with the channel, e.g., multiple diffraction in buildings. It is also sometimes used to model small-scale fading, however without physical reasoning. The log-normal pdf is defined for $x > 0$, as

$$f_{\text{log-normal}}(x) = \frac{1}{x\sqrt{2\pi\sigma^2}} e^{-\frac{(\ln x - m)^2}{2\sigma^2}} \tag{4.3}$$

where the two parameters are m and σ^2.

4.1.4 Nakagami-m Distribution

The Nakagami-m distribution was initially proposed for the modeling of wireless channels in [25], and has since then become popular to describe small-scale

fading, e.g., it is the distribution used in the IEEE 802.15.4a model. The Nakagami-m pdf is defined for $x > 0$ as,

$$f_{\text{Nakagami}}(x) = \frac{2}{\Gamma(m)} \left(\frac{m}{\Omega}\right)^m x^{2m-1} e^{-mx^2/\Omega} \tag{4.4}$$

$m > 0.5$ is the *shape parameter* and $\Omega > 0$ is the *scale parameter*.

4.1.5 Weibull Distribution

The Weibull distribution does not have any physical basis regarding small-scale fading but it generally performs as good or better than the Nakagami-m, as is the case in our Paper II. The Weibull pdf is defined for $x > 0$, as

$$f_{\text{Weibull}}(x) = \alpha x^{\beta-1} e^{-\alpha x^\beta/\beta} \tag{4.5}$$

$\alpha > 0$ is the *shape parameter* and $\beta > 0$ is the *scale parameter*.

4.2 Maximum Likelihood Parameter Estimation

In this section, we briefly outline the ML estimators used to calculate the parameters of the five mentioned pdfs. The results can be found in Paper II.

4.2.1 Rayleigh Distribution

The closed-form expression for the estimation of σ^2 is,

$$\hat{\sigma^2} = \frac{1}{2N} \sum_{i=1}^{N} x_i^2. \tag{4.6}$$

4.2.2 Rician Distribution

There is no closed form ML estimator for the parameters of the Rician distribution. We therefore opted by maximizing the likelihood function manually by means of a grid search.

$$\left\{\hat{\mu}, \hat{\sigma^2}\right\} = \underset{\{\mu,\sigma^2\}}{\arg\max} \ln \left[\prod_{i=1}^{N} f_{\text{Rician}}(x_i)\right]. \tag{4.7}$$

This process is tedious, but has the advantage of providing results with a well defined error from the theoretical ML estimator, i.e, the grid set distance. Other non-ML estimators for the parameters of the Rician distribution include the method of moments [26].

4.2.3 Log-Normal Distribution

The closed-form expression for the estimation of the log-normal parameters are [12]

$$\hat{m} = \frac{1}{N}\sum_{i=1}^{N} \ln x_i \tag{4.8}$$

and

$$\hat{\sigma^2} = \frac{1}{N}\sum_{i=1}^{N} (\ln x - m)^2 . \tag{4.9}$$

4.2.4 Nakagami-m Distribution

The scale parameter of the Nakagami-m distribution corresponds to the mean power of the data,

$$\Omega = \mathcal{E}\left\{x^2\right\} \tag{4.10}$$

so, for a sample data such as $\mathbf{x} = [x_1, x_2, \ldots, x_N]$, the ML estimator is,

$$\hat{\Omega} = \frac{1}{N}\sum_{i=1}^{N} x_i^2 \tag{4.11}$$

One estimator, which is based on an approximation of the Taylor expansion of the ML solution, is [27],

$$\hat{m} = \frac{6\sqrt{36 + 48\Delta}}{24\Delta} \tag{4.12}$$

where the variable Δ is defined as

$$\Delta = \ln\left(\frac{1}{N}\sum_{i=1}^{N} x_i^2\right) - \frac{1}{N}\sum_{i=1}^{N} \ln x_i^2. \tag{4.13}$$

4.2.5 Weibull Distribution

There are no closed form expressions for the ML estimation of the Weibull parameters, the existing estimators are only *approximate* ML solutions. The following derivations are based on [28]. The log-likelihood function for sample

data $\mathbf{x} = [x_1, x_2, \ldots, x_N]$ is,

$$\begin{aligned}\ln L &= \ln\left[\prod_{i=1}^{N} f_{\text{Weibull}}(x_i)\right] \\ &= \ln \alpha^N + \sum_{i=1}^{N} \ln x_i^{\beta-1} + \sum_{i=1}^{N} \ln e^{-\alpha x_i^\beta/\beta} \\ &= \ln \alpha^N + \sum_{i=1}^{N} \ln x_i^{\beta-1} - \alpha \sum_{i=1}^{N} \frac{x_i^\beta}{\beta}\end{aligned}$$

Now to find the ML estimator of the distribution parameters we need to maximize the log-likelihood function in respect to both the parameters:

$$\begin{cases} \frac{\partial}{\partial \alpha} \ln L = 0 \\ \frac{\partial}{\partial \beta} \ln L = 0 \end{cases} \tag{4.14}$$

So, for the first parameter,

$$\begin{aligned}\frac{\partial}{\partial \alpha} \ln L = \frac{N}{\alpha} + 0 - \sum_{i=1}^{N} \frac{x_i^\beta}{\beta} &= 0 \\ \frac{1}{\alpha} &= \frac{1}{N} \sum_{i=1}^{N} \frac{x_i^\beta}{\beta} \\ \hat{\alpha} &= \left(\frac{1}{N} \sum_{i=1}^{N} \frac{x_i^\beta}{\beta}\right)^{-1}\end{aligned}$$

which is a closed form expression for the estimation of α, though assuming knowledge on the second parameter β. For the second parameter we have

$$\frac{\partial}{\partial \beta} \ln L = 0 + \sum_{i=1}^{N} \ln x_i - \alpha \left(\sum_{i=1}^{N} \frac{1}{\beta^2} x_i^\beta \left(\beta \ln x_i - 1\right)\right) = 0 \tag{4.15}$$

and now replacing α for the corresponding estimator $\hat{\alpha}$,

$$\sum_{i=1}^{N} \ln x_i - \left(\frac{1}{N} \sum_{i=1}^{N} \frac{x_i^\beta}{\beta}\right)^{-1} \left(\sum_{i=1}^{N} \frac{1}{\beta^2} x_i^\beta \left(\beta \ln x_i - 1\right)\right) = 0 \tag{4.16}$$

and from here one can numerically find $\hat{\beta}$. Ref. [1] states that the solution of $\hat{\beta}$ is unique and therefore it is easy to make the numerical methods converge to

the solution. The method used in our work to find $\hat{\beta}$ was the Secant method, which converged fairly fast, generally in less that 20 iterations.

4.3 Statistical Model Selection

The above sections have presented different *distributions*, and corresponding ML estimators, for the modeling of small-scale amplitude variations. The next step in the modeling process is to select the distribution, together with its parameters, that best describes the measured data. Several methods exist in the literature for this purpose. In the following, we briefly describe the traditional goodness-of-fit (GOF) tests, and the more recently adopted Akaike information criterion (AIC) for model selection.

4.3.1 Goodness-Of-Fit Tests

GOF tests are a specific type of hypothesis tests. They are used to decide if a given data set belongs to a specific distribution. The Kolmogorov-Smirnov (K-S) test is one of such tests, based on the distance between the *empirical* cumulative distribution function (CDF) and the CDFs of the candidate model. The framework is based on two possible hypothesis, the *null hypothesis* $\mathcal{H}_0$ that corresponds to the event that the sample data has been drawn from the candidate distribution., and the *alternate hypothesis* $\mathcal{H}_1$ that corresponds to the complementary event. A distance metric is then calculated from the two CDFs and compared with a threshold (function of the significance level), that separates the region of the two hypothesis, i.e., the acceptance or rejection region.

The output of GOF tests is simply the acceptance, or not, of the candidate distribution, i.e., passing of the null hypothesis. It does not provide a measure of how good a giving distribution fits the data, and for this reason authors using the K-S test for selecting distributions commonly use their *acceptance rate* as a decision measure.

4.3.2 Akaike Information Criterion

Initiated by Schuster's work [29, 30], the AIC has been gathering general acceptance in the selection of statistical models for the description of wireless channels. The reasons pointed out against GOF tests are the following:

- The candidate distributions *and* their parameters should be known *a priori* in GOF tests. Using distributions with parameters estimated from the test data, can lead to biased results.

- GOF tests do not provide a measure of how good a fit actually is, and therefore should not be used to compare the fit of different distributions.
- The result of GOF tests depends on the significance level, a subjective parameter that varies from study to study.

The AIC on the other hand, gives a measure of how good each distribution fits the data and is suitable for candidate distributions with estimated parameters [31]. The AIC is based on the Kullback-Leibler (KL) distance and was initially derived by Akaike [32] as

$$\mathrm{AIC}_j = -2\sum_{i=1}^{N} \ln f_{\hat{\theta}}^{j}(x_i) + 2U, \tag{4.17}$$

where $f_{\hat{\theta}}^{j}(x_i)$ is the expression of the j:th pdf with estimated parameters $\hat{\theta}$ evaluated at x_i, and U is the number of parameters.

4.3.3 Akaike Weights

The normalized version of the AIC, for a group of candidate pdfs is the so-called *Akaike weights* [33]

$$w_j = \frac{e^{-\frac{1}{2}D_j}}{\sum_{i=1}^{J} e^{-\frac{1}{2}Di}}, \tag{4.18}$$

which satisfy $\sum_{j=1}^{J} w_j = 1$, where J is the number of candidate pdfs and

$$D_j = \mathrm{AIC}_j - \min_j \left(\mathrm{AIC}_j\right). \tag{4.19}$$

The Akaike weights have the advantage of providing information about how well a given distribution fits the data in relation to the other candidates. A more detailed explanation of the above is given in [30].

Chapter 5

Summary and Contributions

THIS CHAPTER is dedicated to the summary of the scientific contributions included in this thesis. The first and second papers focus on the description of the propagation channel for UWB communication systems in outdoor scenarios. The third paper focus on the characterization of soil samples by microwave measurements and the relation of the measured data with the emissions of gas from the soil.

Paper I: Modeling the Ultra-Wideband Outdoor Channel – Measurements and Parameter Extraction Method

In this paper we describe a novel high-resolution scatterer detection algorithm for UWB channels. Scatterers are described as points is space which contribute to the channel impulse response as multipath components (MPC). The method uses data measured from a long linear virtual array, and identifies the received power from each scatterer along the array, in addition to the two-dimensional spatial position of the scatterer. The requirement for a "long" array ensures that the impinging wave fronts are spherical, or in other words, cannot be considered plane. The method is also based on the assumption that only single scattering processes occur in the channel, which makes its applicability limited to scenarios where this assumption is valid.

The paper also presents results from an extensive measurement campaign in outdoor "infostation" scenarios. The knowledge of UWB channels in outdoor scenarios is limited since very few investigations have been done in this area. Our work aimed to fill-in this gap. From the extracted data with the proposed method, we also describe how groups of scatterers, i.e., clusters, show direction-selective radiation properties. Finally, a sample measurement from a shadowed

region is compared with diffraction theory.

I am the main contributor to this paper and I was involved in all parts of the scientific work: channel measurements, data post-processing, derivation of the scatterer detection method and writing of the paper.

Paper II: Modeling the Ultra-Wideband Outdoor Channel – Model Specification and Validation

The focus of this paper was to provide a *complete* model to describe the propagation channel in the measured scenarios. Following the scheme of the scatterer detection method proposed in Paper I, the model is based on the distribution of scatterers in a geometrical space. In addition, the characteristics of the scatterers, and corresponding MPCs, are defined from statistical distributions, making it a GSCM. We believe that the novel concepts on which the model is based, such as the power of scatterers defined by radiation patterns, can be beneficial for the development of future channel models.

I am the main contributor to this paper and I was involved in all parts of the scientific work: channel measurements, data post-processing, derivation of the channel model and writing of the paper.

Paper III: Dielectric Characterization of Soil Samples by Microwave Measurements

The focus of this work was to design and test a microwave measurement setup capable of providing data for the calculation of the dielectric constant of a sample material (in our case, the sample material was peat soil). The novel setup was put to test during a ten day soil monitoring experiment. The collected microwave and methane flux data showed good correlation under specific microwave signal conditions (to our knowledge, it was the first time that such an observation was made). As a next step, we calculated the volumetric fractions of the soil constituents from the measured dielectric constants and related that with the emissions of methane from the soil.

I am the main contributor to this paper, having been the responsible for the planning and execution of the microwave measurements, and all the signal processing applied to the measured data that produced the results given in the paper. However, all the activities directly related with the soil, including the preparation for the measurements, the measurements of the methane flux, and the modeling of the soil by different dielectric materials, was of the responsibility of Norbert Pirk from the Department of Physical Geography and Ecosystem Analysis, Lund University.

References

[1] R. A. Scholtz, "Multiple access with time-hopping impulse modulation," in *Proc. IEEE Military Communications Conference*, vol. 2, pp. 447–450, Oct. 1993.

[2] M. Z. Win, F. Ramirez-Mireles, R. A. Scholtz, and M. A. Barnes, "Ultra-wide bandwidth (UWB) signal propagation for outdoor wireless communications," in *Proc. IEEE Vehicular Technology Conference (VTC'97–Spring)*, pp. 251–255, 1997.

[3] P. Bello, "Characterization of randomly time-variant linear channels," *IEEE Transactions on Communications Systems*, vol. 11, pp. 360–393, Dec. 1963.

[4] J. Ahmadi-Shokouh and R. C. Qiu, "Ultra-wideband (UWB) communications channel measurements - A tutorial review," *International Journal on Ultra Wideband Communications and Systems*, vol. 1, pp. 11–31, 2009.

[5] "Harmonized european standard (telecommunications series)," Tech. Rep. EN 302 217-3 V1.3.1, ETSI, July 2009.

[6] A. F. Molisch, "Ultra-wide-band propagation channels," *Proceedings of the IEEE*, vol. 97, pp. 355–371, Feb. 2009.

[7] A. F. Molisch, *Wireless Communications*. IEEE Press – Wiley, 2005.

[8] H. Schantz, *The Art and Science of Ultrawideband Antennas*. Norwood, MA, USA: Artech Hource Inc., 2005.

[9] A. M. Nicolson and G. F. Ross, "Measurement of the intrinsic properties of materials by time-domain techniques," *IEEE Transactions on Instrumentation and Measurement*, vol. 19, pp. 377–382, Nov. 1970.

[10] T. Gibson and D. Jenn, "Prediction and measurement of wall insertion loss," in *IEEE Antennas and Propagation Society International Symposium*, vol. 2, pp. 1486–1489, July 1996.

[11] A. Muqaibel, A. Safaai-Jazi, A. Bayram, and S. Riad, "Ultra wideband material characterization for indoor propagation," in *IEEE Antennas and Propagation Society International Symposium*, vol. 4, pp. 623–626, June 2003.

[12] R. Vaughan and J. B. Andersen, *Channels, Propagation and Antennas for Mobile Communications*. Stevenage, United Kingdom: IEE, 2003.

[13] R. Kouyoumjian and P. Pathak, "A uniform geometrical theory of diffraction for an edge in a perfectly conducting surface," *Proceedings of the IEEE*, vol. 62, pp. 1448–1461, Nov. 1974.

[14] A.-D. Wirth, *Radar Techniques Using Array Antennas*. Institution of Electrical Engineers, 2001.

[15] S. Ries and T. Kaiser, "Ultra wideband impulse beamforming: It is a different world," *Signal Processing*, vol. 86, no. 9, pp. 2198 – 2207, 2006.

[16] M. Pätzold, *Mobile Fading Channels*. New York, NY, USA: John Wiley & Sons, Inc., 2002.

[17] J. Karedal, F. Tufvesson, N. Czink, A. Paier, C. Dumard, T. Zemen, C. F. Mecklenbräuker, and A. F. Molisch, "A geometry-based stochastic MIMO model for vehicle-to-vehicle communications," *IEEE Transactions on Wireless Communications*, vol. 8, pp. 3646–3657, July 2009.

[18] M. Pätzold, B. rn Olav Hogstad, and N. Youssef, "Modeling, analysis, and simulation of MIMO mobile-to-mobile fading channels," *IEEE Transactions on Wireless Communications*, vol. 7, pp. 510–520, Feb. 2008.

[19] "Spatial channel model for multiple input multiple output (MIMO) simulations," Tech. Rep. 25.996 version 8.0.0, 3GPP, Dec. 2008.

[20] A. Saleh and R. Valenzuela, "A statistical model for indoor multipath propagation," *IEEE Journal on Selected Areas in Communications*, vol. 5, pp. 128–137, Feb. 1987.

[21] J. R. Foerster, "Channel modeling sub-committee report final," tech. rep., IEEE 802.15.3a, Feb. 2003.

[22] A. F. Molisch, D. Cassioli, C.-C. Chong, S. Emami, A. Fort, B. Kannan, J. Karedal, J. Kunisch, H. G. Schantz, K. Siwiak, and M. Z. Win, "A comprehensive standardized model for ultrawideband propagation channels," *IEEE Transactions on Antennas and Propagation*, vol. 54, pp. 3151–3166, Nov. 2006.

[23] K. Haneda and J.-I. Takada, "An application of SAGE algorithm for UWB propagation channel estimation," in *Proc. IEEE Conference on Ultra Wideband Systems and Technologies Digest of Technical Papers*, pp. 483–487, 2003.

[24] R.-M. Cramer, R. Scholtz, and M. Win, "Evaluation of an ultra-wide-band propagation channel," *IEEE Transactions on Antennas and Propagation*, vol. 50, no. 5, pp. 561–570, 2002.

[25] D. Cassioli, M. Z. Win, and A. F. Molisch, "The ultra-wide bandwidth indoor channel: from statistical model to simulations," *IEEE Journal on Selected Areas in Communications*, vol. 20, no. 6, pp. 1247–1257, 2002.

[26] L. J. Greenstein, D. G. Michelson, and V. Erceg, "Moment-method estimation of the ricean k-factor," *IEEE Communications Letters*, vol. 3, pp. 175–176, June 1999.

[27] J. Cheng and N. Beaulieu, "Maximum-likelihood based estimation of the Nakagami m parameter," *IEEE Communications Letters*, vol. 5, no. 3, pp. 101–103, 2001.

[28] N. Balakrishnan and M. Kateri, "On the maximum likelihood estimation of parameters of Weibull distribution based on complete and censored data," *Statistics & Probability Letters*, vol. 78, no. 17, pp. 2971–2975, 2008.

[29] U. Schuster, H. Bolcskei, and G. Durisi, "Ultra-wideband channel modeling on the basis of information-theoretic criteria," *IEEE Transactions on Information Theory*, pp. 97–101, Sept. 2005.

[30] U. G. Schuster, *Wireless Communication Over Wideband Channels*. PhD thesis, Series in Communication Theory, ISSN 1865-6765, Germany, 2009.

[31] H. Akaike, "Likelihood of a model and information criteria," *Journal of Econometrics*, vol. 16, no. 1, pp. 3–14, 1981.

[32] H. Akaike, "Information theory and an extension of the maximum likelihood principle," in *Proc. Second International Symposium on Information Theory*, 1973.

[33] H. Akaike, "On the likelihood of a time series model," *The Statistician*, vol. 27, no. 3-4, pp. 217–235, 1978.

Part II

Included Papers

Paper I

Modeling the UWB Outdoor Channel – Measurements and Parameter Extraction Method

Abstract

This paper presents results from an outdoor measurement campaign for ultra-wideband channels at gas stations. The results are particularly relevant for "infostations" where large amounts of data are downloaded to a user within a short period of time.

We describe the measurement setup and present a novel high-resolution algorithm that allows the identification of the scatterers that give rise to multipath components. As input, the algorithm uses measurements of the transfer function between a single-antenna transmitter and a *long* uniform linear virtual array as receiver. The size of the array ensures that the incoming waves are spherical, which improves the estimation accuracy of scatterer locations. Insight is given on how these components can be tracked in the impulse response of a spatially varying terminal.

We then group the detected scatterers into *clusters*, and investigate the angular power variations of waves arriving at the receiver from the clusters. This defines the cluster's "radiation pattern."

Using sample measurements we show how obstacles obstruct the line-of-sight component – a phenomenon commonly referred to as "shadowing." We compare the measurement data in the shadowing regions (locations of the receiver experiencing shadowing) with the theoretical results predicted by diffraction theory and find a good match between the two.

T. Santos, J. Karedal, P. Almers, F. Tufvesson and A. F. Molisch
"Modeling the UWB Outdoor Channel – Measurements and Parameter Extraction Method," submitted to *IEEE Transactions on Wireless Communications* (second round of reviews), 2009.

1 Introduction

Over the past years, ultra-wideband (UWB) wireless systems have drawn considerable interest in the research community. The ultra-wide bandwidth provides high ranging accuracy, protection against multipath fading, low power spectral density and wall penetration capability [1, 2]. The applications for this innovative technology are numerous, ranging from radar systems for target identification and imaging, accurate localization and tracking as a complement to GPS [3], communications in harsh environments [4], [5] to high-data-rate connectivity [6], [7].

An intriguing application for outdoor high-data-rate connectivity are infostations [8], i.e., short-range transmitters that can operate at extremely high data rates, and thus allow a receiver to download a large amount of data within a very short period of time. A typical infostation can be placed, e.g., at a gas station, allowing wireless downloading of high-definition movies to a car within the time it takes to fill up a gas tank of a vehicle, i.e., within a few minutes. Alternative applications include road and traffic information for driving safety, and wireless payment. These, and related methods for enabling in-car entertainment, have drawn great interest from the car industry in recent years [9].

The first vital step in the design of any wireless system lies in the measurement and modeling of the relevant propagation channels. These determine the theoretical performance limits, as well as the practical performance of actual systems operating in the considered environment. To the best of our knowledge, there have been very few UWB outdoor measurement campaigns presented in the literature. References [10, 11] measured the propagation channel in rural scenarios, [12] measured in "forest," "hilly" and "sub-urban" scenarios, [13, 11] measured the propagation from an office-type environment to an outdoor device; these studies also extract purely stochastic channel models. Ray tracing (not measurements) were used to investigate channel characteristics of farm environments [14]. The results from [13, 14] also form the basis for models CM5, CM 6, and CM 9 of the IEEE 802.15.4a UWB channel model [15]. The campaign most similar to ours is the one of [16], which analyzed the channel between transceivers on a parking lot. It was found in that campaign that a geometrical model that takes the direct and ground-reflected component into account and additionally considers diffuse multipath gave a good agreement with the measured impulse responses. However, there is no measurement campaign dedicated to the infostation scenario, i.e., an outdoor environment close to a gas-station, drive-by restaurant, or similar scenario. The current paper aims to fill that gap, presenting the results of an extensive measurement campaign at two gas stations near Lund, Sweden.

Besides the presentation of sample measurement results from this campaign, the main contributions of this paper are:

- we introduce a new high-resolution algorithm for locating scatterers (interacting objects) based on the use of a large virtual antenna array combined with measurements in the frequency domain;
- we identify clusters of scatterers, and show that they exhibit directional properties; in other words, the power[1] of the multipath components (MPCs) associated with a cluster depends significantly on the direction of observation;
- at some locations in our scenario, the line-of-sight (LOS) between transmitter (TX) and receiver (RX) is shadowed off by an obstacle. We introduce the concept of a "shadowing region," and show that the qualitative behavior of the received signal can be explained by the simple picture of "diffraction around a plate."

Based on the measurement results presented here, the companion paper [17] derives a statistical model for infostation channels.

The remainder of this paper is organized as follows. In Section 2 the measurement campaign and scenarios are described. Then, Section 3 explains the post-processing applied to the measured data, in particular the high-resolution extraction of scatterers for each element of the virtual antenna array along with tracking, and the clustering of the detected scatterers. Subsequently, Section 4, gives insight into some characteristics of the UWB channel, in particular the nonstationary effects of cluster radiation patterns and shadowing of the LOS. Finally, Section 5 wraps up the paper.

2 Measurement Campaign Description

2.1 Measurement Equipment and Setup

Our measurements were done with a HP8720C vector network analyzer (VNA), which measures the S_{21} parameter of the "device under test", namely the propagation channel. The VNA is configured to measure at $N_f = 1601$ regularly spaced frequency points in the range from 3.1 to 10.6 GHz. The intermediate frequency (IF) bandwidth was set to 1000 Hz. A UWB low noise amplifier

[1] The term *power*, is used throughout this paper referring to the dimensionless quantity of the received to transmitted power ratio defined as $P_o/P_i = |V_o/V_i|^2$. The ratio of received to transmitted complex voltages, V_o/V_i, is the quantity measured by the vector network analyzer.

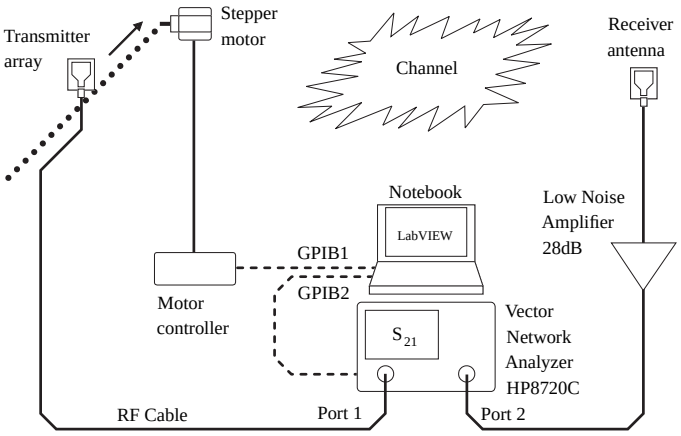

Figure 1: UWB measurement equipment and measurement campaign setup. At every position, the notebook triggers the VNA measurement, stores the S_{21} parameter and moves the transmitter antenna.

(LNA) with a gain of 28 dB and noise figure of 3.5 dB, connected between the RX antenna and the receive port of the VNA, was used to boost the received signal-to-noise ratio (SNR), which was always above 25 dB. A "thru" calibration was performed to eliminate the effect of signal distortions by the cables and amplifier.

Measurements were performed using the virtual array principle, where channel samples at different "array elements" are obtained by mechanically moving a (single) antenna element to different positions. In our setup, the antenna emulating the mobile station (MS) antenna, was moved to various positions along an eight-meter-long plastic rail using a stepper motor. The measurement equipment was controlled by a fully configurable LabVIEW script running on a notebook computer. Both the VNA and the motor controller had general purpose interface bus (GPIB) connections to the notebook. The other antenna emulated a typical base-station (BS) or access-point (AP) in an infostation scenario, and was placed at a fixed location on top of an aluminum pole. A diagram of the measurement setup is given in Fig. 1. During measurement, the channel was static, (i.e., the only movement of any kind was the movement of the MS to different "array element" locations), which is a necessary condition for a virtual-array interpretation [18].

In our campaign we measured the transfer function of the "radio propagation channel" between the antenna connectors at transmitter and receiver; the

radio channel is thus defined to include both the TX and RX antennas and the actual propagation channel. Since the complete radiation pattern of the antennas was not available over the bandwidth of interest, no attempts were made to compensate the impact of the frequency-dependent antenna pattern on the measured data.

Both TX and RX antennas were stamped metal antennas from SkyCross, model SMT-3TO10M-A. They were chosen for their small size, linear phase across frequency. Preliminary measurements furthermore showed that the antenna pattern was almost omnidirectional in the azimuthal plane (with variations on the order of ± 3 dB of the time domain pulse envelope and ± 5 dB for individual frequencies), which is the dominating propagation plane in our measurement scenario. In a real infostation scenario, the mobile user antenna is expected to be on top of or inside a vehicle, leading to additional scattering, thus distorting the antenna patterns. We consciously did not include any vehicle in our campaign, for three reasons:

- by measuring with a car, the final channel model becomes specific to that type of car, and even to the particular antenna placement, used in the campaign;
- the high-resolution algorithm, and the extracted scatterer locations, require the assumption of single-scattering only; this assumption might be violated if there is significant scattering by the car on which the antenna is placed;
- the model derived from our measurements *without* the car can be combined with arbitrary car/antenna combinations through the concept of "composite channels" [19]. In this way, the final model is suitable for situations when the influence of the vehicle is well known (e.g., with a measurement setup similar to the one used in [20]) and can be introduced into the model, becoming suitable for any kind of vehicle.

2.2 Measurement Scenarios

The measured sites were two gas stations in Sweden, Hydro in Staffanstorp and OKQ8 in Södra Sandby. A photo of the latter is given in Fig. 2. The structure of those stations is fairly similar, with a small "main building" containing a convenience store, a number of gas pumps, and a roof supported by structural columns. Comparison of the results from the two stations shows that the channel characteristics are indeed similar. This supports the conjecture that a model derived from those measurement has an applicability that goes beyond the specific measured stations.

Figure 2: Photo of one of the measurement sites. OKQ8 gas station in Södra Sandby, Sweden.

At each location, we considered two BS positions and four straight lines (virtual arrays) of MS positions. Fig. 3 shows a representation of the measured positions. The BS was placed at a height of 2.6 m and the MS at 1.6 m. The first BS location was above the entrance to the gas station's convenience store, whereas the second location was on one of the structural pillars located on the side of one of the gas pumps. The MS positions were chosen to be where a vehicle is expected to stop or pass, namely on the sides of the gas pumps. Each MS virtual array was composed of $N_{\mathrm{MS}} = 170$ sampled positions, with spacing of 48 mm (approximately half of the largest measured wavelength, $\approx \lambda_{\max}/2$), corresponding to a total covered distance of 8.11 m. The total number of measured impulse responses is $2 \times 2 \times 4 \times 170 = 2720$. Fig. 3 also identifies the most significant scattering objects in the environment. Those objects were mostly made of metal, with the exception of the "main building" walls (which were composed of concrete and glass).

3 Post-Processing of Measurement Data

In this section we describe the post-processing applied to the measurement data. Based on the measured channel transfer functions, we try to identify the location of scatterers in the geometrical space. These extracted locations are then subsumed into clusters. The inter-cluster and intra-cluster properties

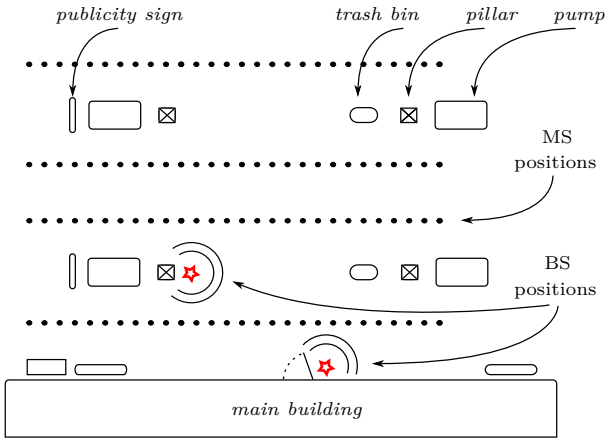

Figure 3: Representation of the typical layout of the measured scenarios. The four dotted lines of MS positions and the two BS positions are indicated.

provide useful insights into the physical propagation mechanisms (which are the emphasis of this paper) and also form the basis of the geometry-based stochastic channel model described in [17].

3.1 Scatterer Detection Method - Principles and Fundamental Assumptions

Our high-resolution scatterer detection method is similar in spirit to the CLEAN algorithm that was introduced for UWB channel sounding in [21], though it differs in some important details. Additional explanations and examples are given in [22].

It is important to note that the method relies on the previously described measurement principle, i.e. using a setup with one antenna on one of the link sides, and a virtual array of antennas on the other link side. In contrast to most existing high-resolution algorithms, which rely on the plane wave assumption, we assume (and require) the array to cover an area large enough so that *the wave fronts arriving to the array are spherical (i.e., plane wave assumption is not valid)*. Then, merging the information from all the array positions improves the detection performance. This is the key innovation of our algorithm.

Longer virtual arrays are also essential to evaluate how the MPCs evolve with changing MS positions, both in the small- and large-scale sense. Fig. 4

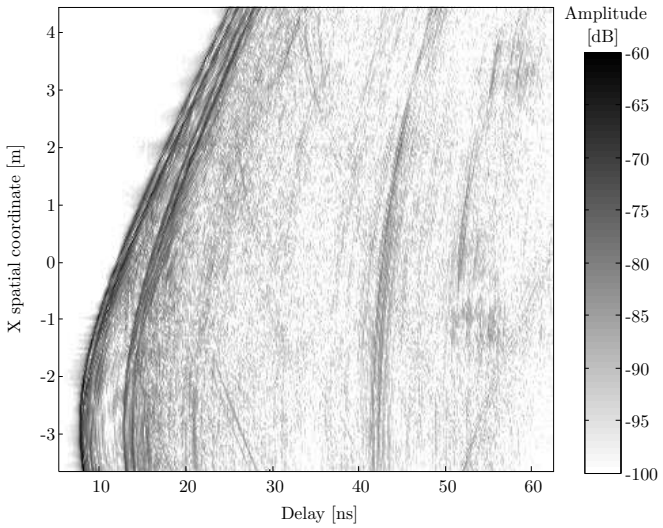

Figure 4: Measured impulse responses along the horizontal direction covering 8.11 m.

shows an example of all the 170 measured impulse responses from one rail. In all impulse responses, the earliest component is the strongest one, which agrees with the interpretation as the LOS. Several "lines", or specular components, can be identified from the figure indicating the presence of physical scatterers. It is also notable that some specular components cannot be observed at all MS locations, whereas others can be observed over the whole measured range of locations. The method described below, identifies these specular MPCs in the delay domain and reveals the scatterer locations in space where they originated from.

The basic principle of our algorithm for finding the specular components in the delay domain is the following: for each impulse response, we detect the strongest peak of the impulse response (using a high-resolution search) and subtract the contribution coming from the corresponding MPC from the impulse response, and then repeat the process until all significant MPCs have been detected. This can be understood as a *search and subtract* approach, which principle also underlies other popular UWB channel parameter estimation methods [21, 23]. While this approach can lead to the appearance of *ghost* components (when the subtracted pulse shapes differ from the actually received ones), it can approximate the performance of maximum-likelihood detection, while being much less computationally burdensome.

It must be emphasized that our algorithm for the extraction of the scatterer location relies on several key assumptions:

- we assume that only single-scattering processes are relevant. This is a reasonable assumption given the largely open structure of the gas station. Note that the concept of "equivalent scatterer location" of [24] is not directly applicable in our model, because it is only defined for relatively small sizes of the virtual array.

- propagation occurs only in the horizontal plane. Due to our measurement setup (linear virtual array), identification of the elevation angle of the radiation, and thus height-coordinate of the scatterers, is not possible. Given the geometry of the setup, it is reasonable to assume that scattering could occur from the ground, as well as from the roof above the gas pumps. Since the echoes from the ground and roof do not propagate in the horizontal plane, the position the of scatterers extracted with the horizontal-only assumption will be off. Nevertheless, the arriving delays of these components are similar to the delays of MPCs that are reflected at the wall behind the BS antenna, and are therefore detected as part of the same cluster (see below).

- we assume that the temporal distortions by the scattering process can be neglected. It is well known [18] that in its most general case, the UWB impulse response can be modeled as

$$x(\tau) = \sum_{k=1}^{N} \alpha_k \chi_k(\tau) * \delta(\tau - \tau_k), \tag{1}$$

  where $\chi_k(\tau)$ denotes the distortion of the k^{th} arriving component due to the frequency selectivity of the interactions with the environment, α_k its amplitude and τ_k the corresponding delay. N is the number of scatterers, and $*$ denotes the convolution operation. Nevertheless, since the distortion functions are in general not known, this model can not be applied to scatterer detection. By using the simplified model

$$x(\tau) = \sum_{k=1}^{L} \alpha_k \delta(\tau - \tau_k), \tag{2}$$

  where $L > N$, a distorted pulse looks like a sequence of closely-spaced pulses with amplitudes determined by the power carried by the MPC as well as the pulse distortion. Thus, the simplified model might ultimately identify more scatterers than physically exist, thus generating so-called

"ghost components" but their locations will be closely spaced around the locations of the true scatterers.

Despite the restrictions and caveats mentioned above, our scatterer location algorithm works well - this is confirmed by the fact that the extracted locations correspond well to the location of physical objects (gas pumps, columns, etc.) in our environments.

3.2 Scatterer Detection Method – Mathematical Formulation

A simplified flowchart of the method steps is given in Fig. 5. The method proceeds in an inner and an outer loop.
Step I: The inner loop runs for each array position, detecting iteratively with high-resolution the peaks in the impulse response with the highest amplitude. The loop stops when all peaks with an amplitude above a user-defined threshold are found.
Step II: Identification of the scatterer locations corresponding to the peaks detected in *Step I*. This is done by a spatial grid search where every grid point is a candidate scatterer (CS). Each CS is then associated with the peaks (of *all* impulse responses), from which we also deduce the visibility region and overall weight of the CS.
Step III: The CS with the strongest weight is chosen, and its contribution is subtracted from the original measured data. This defines the outer loop, which restarts from *Step I* with the updated data. The process continues until no more CSs are to be analyzed. The mathematical formulation of the above follows.

The measurement data is available in the frequency domain. The (complex) transfer function at the N_f frequency points are written into a vector $\mathbf{h}_i \in \mathbb{C}^{N_F \times 1}$,

$$\mathbf{h}_i = \left[\begin{array}{ccc} h_0 & \cdots & h_{N_F-1} \end{array} \right]^T. \tag{3}$$

where $(\cdot)^T$ is the transpose operator and i is indexing the different array positions. Since our channel model (2) is defined in the time domain, we can obtain a continuous channel impulse response $x(\tau)$ as

$$x(\tau) = \mathbf{p}^T(\tau)\mathbf{h}_i, \tag{4}$$

where $\mathbf{p}(\tau) \in \mathbb{C}^{N_F \times 1}$ is the vector of the IDFT (inverse discrete Fourier transform) coefficients, i.e.,

$$\mathbf{p}(\tau) = \left[\begin{array}{ccc} e^{j2\pi f_0 \tau} & \cdots & e^{j2\pi (f_0 + (N_F-1)\Delta f)\tau} \end{array} \right]^T,$$

where f_0 is the lowest measured frequency, and Δf is the frequency step.

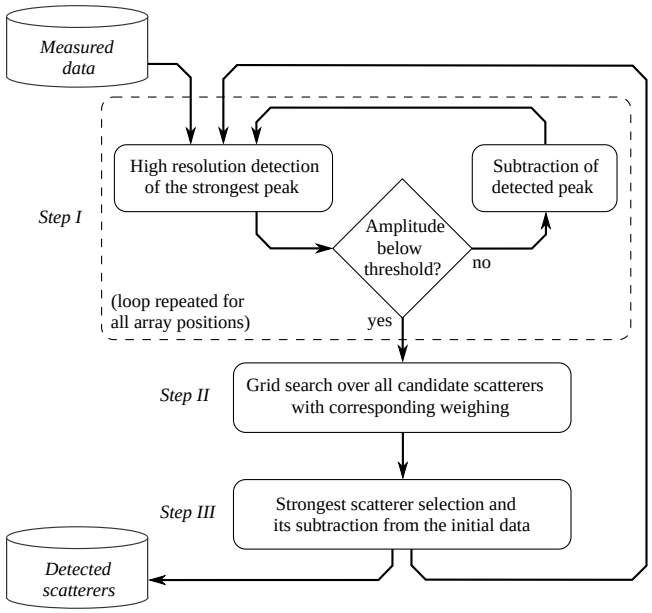

Figure 5: Simplified flowchart of the scatterer detection method.

The peak search step can be formulated as the maximization of the impulse response envelope over the delay variable τ. Since τ is a continuous variable which can take any real value, our resolution can be arbitrarily high. The estimated delay of the i:th array position and l:th strongest peak then becomes

$$\hat{\tau}_{i,l} = \arg\max_{\tau} \left| \mathbf{p}^T(\tau)\mathbf{h}_{i,l} \right|, \tag{5}$$

and the corresponding complex amplitude is obtained as

$$\hat{\alpha}_{i,l} = \frac{\mathbf{p}^T(\hat{\tau}_{i,l})\mathbf{h}_{i,l}}{\mathbf{p}^T\mathbf{p}}. \tag{6}$$

The vector $\mathbf{h}_{i,l}$ is defined as the impulse response remaining after the contribution of the $l-1$ th peak has been subtracted, i.e.,

$$\mathbf{h}_{i,l} = \begin{cases} \mathbf{h}_i, & l = 1 \\ \mathbf{h}_{i,l-1} - \hat{\alpha}_{i,l-1}\mathbf{p}^*(\hat{\tau}_{i,l-1}), & l > 1 \end{cases} \tag{7}$$

where $(\cdot)^*$ denotes complex conjugation. Note that the subtraction is performed not in the *transform* domain (i.e., delay domain), but over the same domain

that the data were measured, i.e., the frequency domain. The process continues until the estimated peak amplitude $|\hat{\alpha}_{i,l}|$ falls below a predefined threshold μ.[2] For our data, we chose to set this threshold corresponding to a signal power of -99 dB which was 20 dB above the estimated noise floor at -119 dB. At a distance of 11.17 m between the antennas, this threshold was still 25 dB below the LOS power, as illustrated in Fig. 7. The peak detection process is repeated for all the array positions.

The next step consists of finding the point scatterers in the two-dimensional *geometrical* space that match with the detected peaks in the impulse response. To find those scatterers we scan for their presence over all the array positions simultaneously. This is accomplished by a grid search where every geographical point is a candidate scatterer (CS). The step of the grid search was 10 mm, which is four times smaller than the spacing of the virtual array positions. In order to find the strongest CS, we determine their respective *weights* as described subsequently.

For each CS, we calculate the theoretical propagation delay for all the MS positions, assuming a single bounce on the CS and wave propagation at the speed of light. Then, a peak of the impulse response is associated with a CS if its propagation delay agrees with the CS's theoretical delay within the delay resolution of our system (the inverse of the bandwidth). From this rule, a given CS can have at most N_{MS} peaks associated to it, one for each array position.

Since our measurements covered large distances, certain scatterers might not be "visible" over the whole array, i.e., do not have peaks of the impulse response associated with them for all positions of the MS along the rail. We therefore define the *visibility region* of a scatterer. To this end, we use an average sliding window (ASW) over the associated peak amplitudes, which for the k^{th} CS is

$$\mathbf{w}_k\left[i\right] = \frac{1}{N_W} \sum_{n=-N_W/2}^{N_W/2-1} \alpha_{n+i,k}.$$

Here, N_W is the window size and α are the peak amplitudes. The window slides over the consecutive array positions as $i = 1, \ldots, N_i$. We used a window size corresponding to an area of one meter, the size of the expected region of stationarity.[3] The locations where the ASW crosses the threshold μ define the *birth* and *death* of the CS, and the visibility region is defined as the region between birth and death location. Finally, the *weight* of a CS is defined as the integrated power of the impulse response peaks associated with a CS that lie

[2] An illustrative example of the peak search step, and corresponding detected peaks, can be found in [22] Fig. 2.

[3] The justification for the choice of one meter stems from the fact that all significant scatterers are visible for at least one meter along the array (cf. Fig. 4).

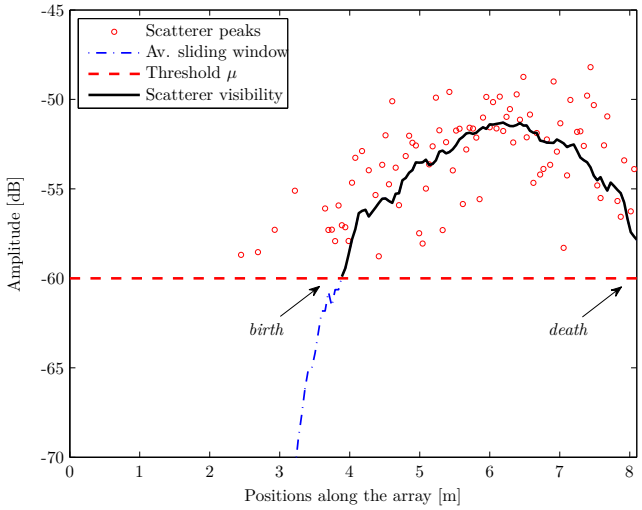

Figure 6: Selected peak amplitudes and corresponding visibility region for an example scatterer. The array positions without a selected peak, are considered to have zero amplitude on the ASW calculation.

within its visibility region. An illustrative example of the visibility region of a scatterer, and corresponding birth and death positions, can be seen in Fig. 6.

After weighting, it is possible to select the strongest CS and save its information in a data base. Using again the successive cancellation principle, the measured frequency responses are updated by subtracting the contributions to the impulse responses by this scatterer before the detection of the next. The update is defined as

$$\mathbf{h}_i = \mathbf{h}_i - \hat{\alpha}_{i,l_{\text{peak}}} \mathbf{p}^* \left(\hat{\tau}_{i,l_{\text{peak}}} \right) \tag{8}$$

for all the array positions whose impulse responses have a peak associated with the scatterer, where $\alpha_{i,l_{\text{peak}}}$ and $\hat{\tau}_{i,l_{\text{peak}}}$ are the estimated delay and complex amplitude corresponding to the MPC of the selected scatterer at the array position i. At this point, the process is repeated starting from the high resolution peak search.

The output of the method above also provides us with the information on how the contribution from a given scatterer evolves along the array (for different MS positions). This means that we can track the MPCs associated with the scatterers. An example of tracking is shown in Figs. 7(a) and 7(b). In Fig. 7(a), eight detected scatterers are identified with a marker and labeled with a letter, $\{a, \ldots, h\}$. To ease the visual interpretation, MPCs with similar delays

are also given similar markers. MPCs a and b, are the LOS and back wall reflection, respectively, and the remaining MPCs originate from different metal objects. Fig. 7(b) shows the MPC delays corresponding of the same scatterers after moving the antenna 1.34 m away from the initial location.

By comparing both figures, it can be seen how some scatterers maintain their relative delays while the delays between some other components changes. The four MPCs with circle markers, for example, initially have similar delays, and it might be conjectured that their corresponding scatterers are in similar spatial locations. However, with the movement of the antenna, they evolve separately in two sub-groups, $\{e, g\}$ and $\{f, h\}$, revealing that those two groups of scatterers do not originate from the same physical location. By matching the detected scatterers with the real environment, it was found that $\{e, g\}$ belonged to a publicity sign and $\{f, h\}$ to a gas pump which were actually separated by 13 m.

3.3 Clustering the Detected Scatterers Using a Modified K-means Approach

It is well established in the literature that scatterer locations tend to be *clustered*. (see, e.g., [25, 26, 27]). Here we define a *cluster as a group of scatterers located a similar points in space.* Clustering can give additional physical insights into the propagation mechanisms, and is also useful in the establishment of simple yet accurate channel models. Both visual inspection [26] and automated clustering [27] have been proposed in the literature; we use the latter approach in this paper.

The K-means clustering algorithm [28] groups the scatterers by minimizing the Euclidean distance from the scatterers to the cluster centroids, over all clusters. The distance metric used here was modified to minimize the power-weighted geometrical distances.[4] In other words, we scale the geometric distance to the centroid by the scatterer power, such that the distance metric from a scatterer at position (x_s, y_s) with power P_s to a centroid at (x_c, y_c) is given by

$$d_{\text{metric}} = P_s \sqrt{(x_s - x_c)^2 + (y_s - y_c)^2}. \tag{9}$$

With this approach, the position of the centroids will be more dependent of the position of a stronger scatterer than of a weaker one. The definition is similar to the "center of gravity", and follows from the intuitive idea that for a

[4] Since our data is defined in three dimensions (*x-coord*, *y-coord*, *power*), a straightforward application is to perform the clustering equally over all the dimensions. This is not reasonable, since it results in the grouping of scatterers also by their level of power, which doesn't agree with the observed measurements.

specific cluster positions, it is more likely to find stronger components around its center, and also solves the problem of weaker, far-away scatterers pulling the centroid excessively away from the true center. This definition was first proposed in [27] and referred to as the KPowerMeans algorithm.

The K-means algorithm is iterative, and thus requires an initial estimate of the cluster position. Since from our measurement campaigns, we had a good knowledge of the environment surrounding the antennas, we made use of it to select the initial parameters. The positions in space matching physical objects and scatterers were set as initial cluster positions. This was found to be preferable to blind methods, since it reduces clustering errors.[5]

An example of the output of the clustering algorithm is illustrated in Fig. 8, where different clusters were given different markers and colors.

4 Cluster Directional Properties and Shadowing

4.1 Cluster Directional Properties

The power of the MPC associated with a specific scatterer, as well as the sum of the powers of the MPCs associated with a cluster, varied over the different MS positions. To better interpret these variations, we investigate in this subsection whether the power variations of a given MPC are correlated with the power variations of the other MPCs associated with the same cluster of scatterers. Furthermore, we show that these variations can be compactly described in the angular domain.

As examples, we choose three sets of clustered scatterers depicted in Fig. 8. Since the propagation paths between a given scatterer and different MS positions have different path loss due to the different runlengths the signal has to cover, we compensate these losses using a d^{-n} distance power law. The pathloss coefficient $n = 1.38$ was obtained from a least-squares fit using all available data, see [17] subsection II-D. The resulting normalized receive power as a function of the angle under which the MS "sees" the scatterer is henceforth called the "radiation pattern" of the scatterer. The covered angular range in the azimuth plane is limited, but is similar for the scatterers belonging to the same cluster. Given that our interest is on the directional properties of the scatterers, and not on their relative level of power, each radiation pattern is normalized such that the maximum has unit amplitude.

Subsequently, the radiation pattern of the scatterers within a cluster were averaged to form the cluster radiation pattern. The resulting patterns are also

[5] A clustering error occurs when a calculated centroid ends up where no physical object exists – a situation often related to the algorithm converging to a local minimum.

shown in Fig. 8, centered on the corresponding clusters. From the figure, one can observe that each cluster radiates in a preferred direction with a beam-like shape. Fig. 9 shows the same radiation patterns, but plotted directly in the angular domain. It can be seen that the radiation patterns are approximately symmetrical with respect to the angle of maximum radiation.

The results presented here are from a single virtual array, but these directional characteristics of the group of scatterers were found throughout all our measurements. The patterns vary in width and shape from cluster to cluster, but a preferred direction of radiation is always identifiable. It is important to stress here that these amplitude variations are not originated by shadowing from obstructing objects but by the characteristics of the physical objects themselves.

4.2 Shadowing Behind Objects

In some of our measurements, there were MS positions for which no LOS existed between TX and RX. This occurred when the MS antenna was in the shadow region of a physical object, such as a gas pump or a column. In this section, we investigate the behavior of the received signal while the MS was being moved through such shadow regions.

When the MS is entering a shadow region of a given object, the signal strength starts to decay from its LOS value. The inverse process takes place when the MS is leaving the shadow region. Furthermore, on several occasions, a well defined amplitude peak is observed when the MS is exactly behind the shadowing object, in the center of the shadow region. This peak can be explained qualitatively by diffraction theory. Since there are two main diffraction components, one from each side of the shadowing object, these two components can add constructively behind the object, to create a *peak*.

For the description of the diffraction field in UWB communications, several useful results are available in the literature: e.g., the recent work by Zhou and Qiu [29], provides closed-form expressions for the impulse responses of several canonical channels. Other fundamental work in this topic pertaining to the time domain is [30, 31, 32]. Here, we use the well known frequency domain[6] expressions of the uniform geometrical theory of diffraction (UTD/GTD) [33], i.e.,

$$E_d(s) = E_i D(\hat{s}, \hat{s}') A_d(s) e^{-jks}, \tag{10}$$

in which s is the distance between the diffraction edge and the observation point, E_i is the incident field on the edge, $D(\hat{s}, \hat{s}')$ is the dyadic diffraction

[6]The frequency domain expressions were used instead of the time domain ones, since the measurements were also performed in the frequency domain.

coefficient, $A_d(s)$ describes how the amplitude of the field varies along the diffracted ray and k is the wave number.[7]

Fig. 10 compares the first received component from the MS behind a steel pillar, extracted from the measurements, with the predicted electrical field behind a perfectly electric conductor (PEC) plate in the same location. The PEC plate was chosen for the comparison because it is the geometry that among all canonical geometries is the closest to the steel pillar, it leads to straight wedge diffraction. For the simulation, the diffracted field was assumed to be constituted by two components, one for each side of the plate; both calculated from (10). Since the cross section of the pillar was 0.3×0.3 m, the simulated object (also 0.3 m wide) was at least three times larger than any of the considered wavelengths, which supports the validity of (10).

The measured signal was normalized to the strength of the hypothetical LOS signal (i.e., in the absence of shadowing objects). Since there was no perfect knowledge of the transmitted pulse shape, a frequency flat pulse was used in the simulation. The figure shows a qualitative match, but no perfect quantitative agreement. This is to be expected, because the shape and electromagnetic properties of the actual pillar did not agree with the "two-wedge" model used in the theoretical computations.

5 Conclusions

In this work, we have described the results from one of the few existing UWB outdoor measurement campaigns. The target scenario was a gas station, an environment envisioned in the context of UWB-based infostations. We have described a scatterer detection method which is suitable for UWB outdoor measurements deploying a virtual array covering long distances.

The tracking capabilities of the method showed how the delays of MPCs change within the impulse response as the MS moves. The analysis of the cluster directional properties showed that groups of scatterers have a preferred direction of radiation and often the shape of their radiation pattern approaches the one of a directional beam. This knowledge is of valuable help for the development of more accurate, non-purely statistical, channel models. The study of the shadow effects on the UWB signal envelope revealed an increase of the signal amplitude was often found when one of the antennas was exactly behind a shadowing object; diffraction theory was shown to give a good explanation to this effect.

[7] A complete definition of $E_d(s)$ and all of its components is given in detail in [33].

Acknowledgments

The authors would like to thank Dr. R. Qiu for the helpful discussion regarding the diffraction issues. We also thank the reviewers of this manuscript for their constructive remarks.

References

[1] M.-G. Di Benedetto, T. Kaiser, A. F. Molisch, I. Oppermann, C. Politano, and D. Porcino (eds.), *UWB Communications Systems, A Comprehensive Overview*. EURASIP publishing, 2005.

[2] X. Shen, M. Guizani, R. C. Qiu, and T. Le-Ngoc, *Ultra Wideband Wireless Communications and Networks*. John Wiley, 2006.

[3] Z. Sahinoglu and S. Gezici, "Ranging in the IEEE 802.15.4a standard," *Proc. IEEE Annual Wireless and Microwave Technology Conference*, pp. 1–5, 2006.

[4] R. A. Scholtz, D. M. Pozar, and W. Namgoong, "Ultra-wideband radio," *Journal on Applied Signal Processing*, no. 3, pp. 252–272, 2005.

[5] M. Win and R. Scholtz, "On the energy capture of ultrawide bandwidth signals in dense multipath environments," *IEEE Communications Letters*, vol. 2, pp. 245–247, Sept. 1998.

[6] A. Batra, J. Balakrishnan, and A. Dabak, "Multi-band OFDM: A new approach for UWB," in *Proc. International Symposium on Circuits and Systems*, pp. 365–368, 2004.

[7] "High rate ultra wideband PHY and MAC standard ECMA-368, 3rd edition," Dec. 2008.

[8] R. Frenkiel, B. Badrinath, J. Borres, and R. Yates, "The infostations challenge: Balancing cost and ubiquity in delivering wireless data," *IEEE Personal Communications*, vol. 7, no. 2, pp. 66–71, 2000.

[9] DaimlerChrysler, "DaimlerChrysler to demonstrate first of its kind invehicle video streaming over UWB at CES WiMedia techzone," Jan. 2007.

[10] M. Z. Win, F. Ramirez-Mireles, R. A. Scholtz, and M. A. Barnes, "Ultrawide bandwidth (UWB) signal propagation for outdoor wireless communications," in *Proc. IEEE Vehicular Technology Conference (VTC'97–Spring)*, pp. 251–255, 1997.

[11] "UWB channel measurements and modeling for DARPA NETEX." Virginia Tech, 2004.

[12] M. D. Renzo, F. Graziosi, R. Minutolo, M. Montanari, and F. Santucci, "The ultra-wide bandwidth outdoor channel: From measurement campaign to statistical modelling," *Mobile Networks and Applications*, vol. 11, no. 4, pp. 451–467, 2006.

[13] C. Kim, X. Sun, L. Chiam, B. Kannan, F. Chin, and H. Garg, "Characterization of ultra-wideband channels for outdoor office environment," in *Proc. IEEE Wireless Communications and Networking Conference*, vol. 2, pp. 950–955, 2005.

[14] S. Emami, C. Corral, and G. Rasor, "Ultra-wideband outdoor channel modeling using ray tracing techniques," in *Proc. IEEE Consumer Communications and Networking Conference*, pp. 466–470, Jan. 2005.

[15] A. F. Molisch, D. Cassioli, C.-C. Chong, S. Emami, A. Fort, B. Kannan, J. Karedal, J. Kunisch, H. G. Schantz, K. Siwiak, and M. Z. Win, "A comprehensive standardized model for ultrawideband propagation channels," *IEEE Transactions on Antennas and Propagation*, vol. 54, pp. 3151–3166, Nov. 2006.

[16] A. Domazetovic, L. J. Greenstein, N. B. Mandayam, and I. Seskar, "A new modeling approach for wireless channels with predictable path geometries," in *Proc. IEEE Vehicular Technology Conference (VTC'02–Fall)*, vol. 1, pp. 454–458, Sept. 2002.

[17] T. Santos, F. Tufvesson, and A. F. Molisch, "Modeling the ultra-wideband outdoor channel – Model specification and validation." submitted to IEEE Transactions on Wireless Communications, 2009.

[18] A. F. Molisch, "Ultrawideband propagation channels-theory, measurement, and modeling," *IEEE Transactions on Vehicular Technology*, vol. 54, pp. 1528–1545, Sept. 2005.

[19] F. Harrysson, J. Medbo, A. F. Molisch, A. Johansson, and F. Tufvesson, "The composite channel method: Efficient experimental evaluation of a realistic MIMO terminal in the presence of a human body," in *Proc. IEEE Vehicular Technology Conference (VTC'08–Spring)*, pp. 473–477, May 2008.

[20] F. Berens, H. Dunger, S. Czarnecki, T. Bock, R. Reuter, S. Zeisberg, J. Weber, and J. Guasch, "UWB car attenuation measurements," in *Proc. IST Mobile and Wireless Communications Summit*, pp. 1–5, 2007.

[21] R.-M. Cramer, R. Scholtz, and M. Win, "Evaluation of an ultra-wide-band propagation channel," *IEEE Transactions on Antennas and Propagation*, vol. 50, no. 5, pp. 561–570, 2002.

[22] T. Santos, J. Karedal, P. Almers, F. Tufvesson, and A. F. Molisch, "Scatterer detection by successive cancellation for UWB – Method and experimental verification," in *Proc. IEEE Vehicular Technology Conference (VTC'08–Spring)*, pp. 445–449, May 2008.

[23] K. Haneda and J.-I. Takada, "An application of SAGE algorithm for UWB propagation channel estimation," in *Proc. IEEE Conference on Ultra Wideband Systems and Technologies Digest of Technical Papers*, pp. 483–487, 2003.

[24] A. F. Molisch, A. Kuchar, J. Laurila, K. Hugl, and R. Schmalenberger, "Geometry-based directional model for mobile radio channels-principles and implementation," in *Proc. European Transactions on Telecommunications*, vol. 14, pp. 351–359, 2003.

[25] A. F. Molisch, H. Asplund, R. Heddergott, M. Steinbauer, and T. Zwick, "The COST259 directional channel model part I: Overview and methodology," *IEEE Transactions on Vehicular Communications*, vol. 5, pp. 3421–3433, Dec. 2006.

[26] M. Toeltsch, J. Laurila, K. Kalliola, A. Molisch, P. Vainikainen, and E. Bonek, "Statistical characterization of urban spatial radio channels," *IEEE Journal on Selected Areas in Communications*, vol. 20, no. 3, pp. 539–549, 2002.

[27] N. Czink, P. Cera, J. Salo, E. Bonek, J.-P. Nuutinen, and J. Ylitalo, "A framework for automatic clustering of parametric MIMO channel data including path powers," in *Proc. IEEE Vehicular Technology Conference (VTC'06–Fall)*, pp. 1–5, Sept. 2006.

[28] J. A. Hartigan and M. A. Wong, "Algorithm AS 136: A K-means clustering algorithm," *Applied Statistics*, vol. 28, no. 1, pp. 100–108, 1979.

[29] C. Zhou and R. C. Qiu, "Pulse distortion and optimum transmit waveform for pulse-based UWB communications," *International Journal on Ultra Wideband Communications and Systems*, vol. 1, pp. 32–48, 2009.

[30] T. W. Veruttipong, "Time domain version of the uniform GTD," *IEEE Transactions on Antennas and Propagation*, vol. 38, pp. 1757–1764, Nov. 1990.

[31] P. R. Rousseau and P. H. Pathak, "Time-domain uniform geometrical theory of diffraction for a curved wedge," *IEEE Transactions on Antennas and Propagation*, vol. 43, pp. 1375–1382, Dec. 1995.

[32] P. R. Rousseau, P. H. Pathak, and H.-T. Chou, "A time domain formulation of the uniform geometrical theory of diffraction for scattering from a smooth convex surface," *IEEE Transactions on Antennas and Propagation*, vol. 55, pp. 1522–1534, June 2007.

[33] R. Kouyoumjian and P. Pathak, "A uniform geometrical theory of diffraction for an edge in a perfectly conducting surface," *Proceedings of the IEEE*, vol. 62, pp. 1448–1461, Nov. 1974.

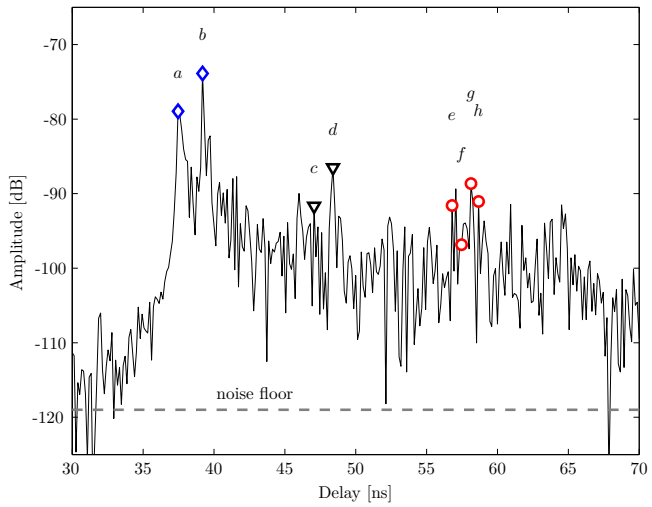

(a)

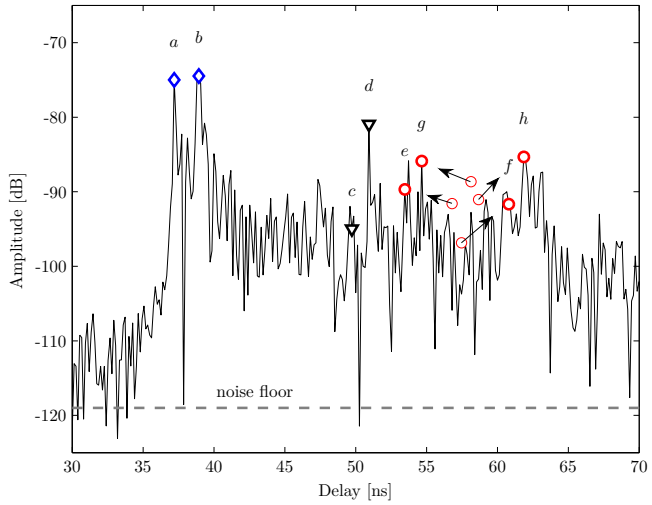

(b)

Figure 7: Scatterer tracking example from the UWB impulse response where the labeled components were found using the method described in Section 3.2: (a) at position $(x = -1.57, y = 11.06)$ and (b) at position $(x = -0.23, y = 11.06)$.

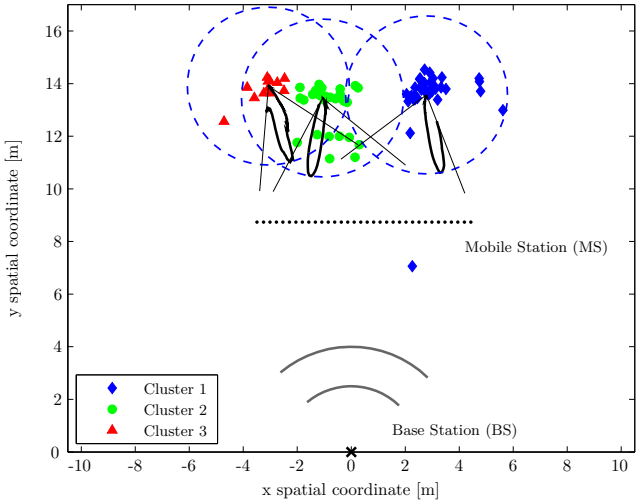

Figure 8: Estimated radiation pattern of three clusters of scatterers. The cluster at the base station is not shown.

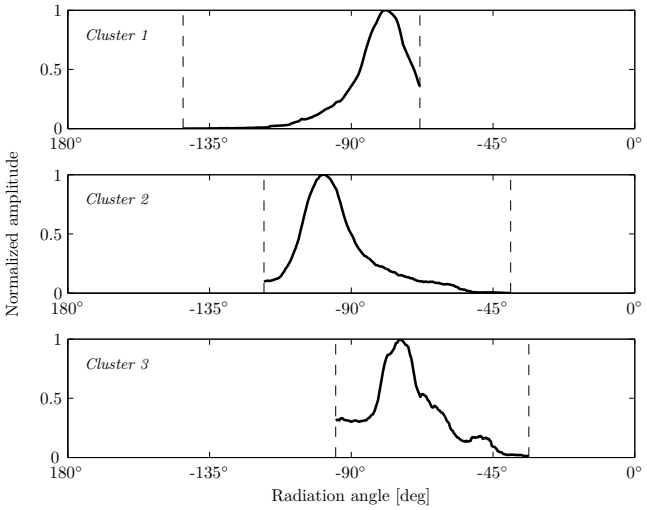

Figure 9: Estimated radiation pattern of three channel clusters in the angular domain.

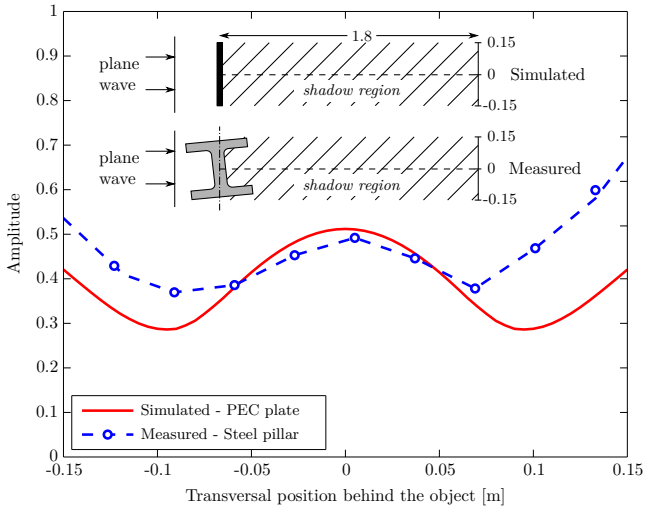

Figure 10: Simulated and measured signal amplitudes behind shadow objects. The upper sketches illustrate the simulated and measured geometries. The incident wave is considered plane since in the measured scenario the BS antenna was 14 m away from the pillar.

Paper II

Modeling the UWB Outdoor Channel – Model Specification and Validation

Abstract

In this paper we establish a geometry-based stochastic ultra-wideband channel model for gas stations. We statistically describe the 2D spatial location and power of clustered scatterers, the shape of their visibility and shadowing regions. We also separately model the diffuse part of the impulse response (i.e., the part that cannot be explained by the scatterers' multipath components), and show that its amplitude fading statistics can be best described by a Weibull distribution with a delay dependent β-parameter. A step-by-step implementation recipe demonstrates how the model can be built. Finally, we validate our model by comparing simulated and measured channel parameters such as the rms delay spread.

T. Santos, F. Tufvesson and A. F. Molisch
"Modeling the UWB Outdoor Channel – Model Specification and Validation,"
submitted to *IEEE Transactions on Wireless Communications*
(second round of reviews), 2009.

1 Introduction

Ultra-wideband (UWB) communications is a technology capable of delivering high data rates over short distances. One possible application is the delivery of multimedia content to vehicles briefly stopping at locations such as gas stations (the focus of this work) or drive-thru restaurants. Such transmission scenarios have been dubbed *infostations* in the literature [1].

A fundamental prerequisite for analyzing the possible performance of such systems is an understanding of UWB propagation channels in outdoor gas station environments. In [2] we have described an extensive measurement campaign in such environments, concentrating on the measurement setup and data processing that yielded the 2D spatial position of relevant scatterers.

Based on those results, the current paper derives a detailed channel model. The model is novel both in the sense that many elements of its generic structure have not previously been proposed in the literature, and that no parameterized (quantitative) model has been previously proposed for the gas station scenario. The main purpose of the developed model is to enable system simulations and analysis of information-theoretic limits of transmission in the considered environment.

A large number of generic channel models has been proposed in the literature [3, 4, 5]. In particular, for UWB channels, tapped delay line channel models with regular tap spacing [6], [7], Saleh-Valenzuela-type channel models [8], [9], as well as geometry-based models [10] have been used. However, none of the existing generic modeling approaches is completely suitable to explain all the features of our measurement results. We therefore introduce a new model that bears some similarities to [10, 11, 12] in that it is also geometry-based, and considers discrete path components as well as diffuse components. However, we introduce several novel concepts for UWB channel modeling: (i) cluster "beampatterns" describing the directional dependence of the radiation emanating from a cluster, (ii) shadowing regions that represent the large-scale attenuation of the LOS for certain TX/RX locations, and (iii) Laplacian distributed scatterer coordinates within clusters.

The remainder of the paper is organized as follows. Firstly, in Section 2 we summarize our previous work, subsequently in Section 3 we describe the chosen modeling approaches and their motivations based on the measured data. Then, in Section 4 we provide the values for all the model parameters and give a step-by-step formula to generate the channel impulse responses. In Section 5 the model validation is presented and in 6 we wrap up the paper with the conclusions.[8]

[8] *Notation a)* The term *power*, is used throughout this paper referring to the dimensionless quantity of the received to transmitted power ratio defined as $P_o/P_i = |V_o/V_i|^2$. The ratio

2 Measurement Campaign and Post Processing

For the convenience of the reader, this section summarizes the measurement methodology and data postprocessing of our gas station measurement campaign; more details are given in [2].

The measurements were performed at two gas stations (scenario 1 and 2) near Lund, Sweden. At each of them, the positioning of the antennas was as follows: the antenna representing the BS was placed at the entrance of the gas station shop or near the top of one of the gas pumps, while the second antenna, representing the MS, was moved along a rail positioned at the sides of the gas pumps (the location where a vehicle is expected to stop or pass through). A single rail of measurements compromised 170 MS positions separated 0.048 m from each other, creating an *eight* meter virtual array. During the measurement of each array, BS and scatterers did not move; furthermore the MS did not move during the measurement at one particular MS position, so that the channel was completely static. Furthermore, in each of the two gas stations, we had two BS positions combined with four MS rail positions, resulting on a total of $2 \times 2 \times 4 \times 170 = 2720$ frequency responses measured in the two scenarios. The transfer functions of the channels were measured by means of a VNA, configured to measure the S_{21} parameter of $N_f = 1601$ regularly spaced frequency points, covering from 3.1 to 10.6 GHz. The antennas were SkyCross SMT-3TO10M-A, chosen for their approximately omnidirectional radiation pattern in the horizontal plane. No attempts were made to eliminate the influence of the antennas from the measured data; they are therefore *ipse facto* included in the proposed model.

The data post processing phase consisted of two main steps

- *Scatterer detection* – In this step we used a novel channel estimation method, which takes as input all the 170 frequency responses of a single eight meter virtual array, and identifies the scatterers by means of successive cancellation.[9] The method makes use of (i) the fact that an MPC is visible from several consecutive (on the rail) MS positions (also referred to as *visibility region*) and (ii) the assumption that only *single-scattering* processes occur, in order to find the spatial location of the scatterer. Each

of received to transmitted complex voltages, V_o/V_i, is the quantity measured by the vector network analyzer (VNA). *b)* The terms TX (transmitter) or BS (base station), and RX (receiver) or MS (mobile station) are used interchangeably throughout the text. *c)* In order to maintain self-consistency of the definitions for the different statistical models, we refer to the pdfs as defined in the book by Papoulis [13] unless specifically indicated otherwise.

[9] A *scatterer* is here defined to be a point in a 2-dimensional space that reflects power from the TX to the RX antenna. A *multipath component* (MPC) is the name given to the signal that arrives at the RX from the scatterer.

one of the detected scatterers is then characterized by its 2D coordinates, visibility region and received power of its associated MPC at the different MS positions. The figures in Section 4 provide a more visual interpretation of these concepts, e.g., one given point (scatterer) in Fig. 8 is mapped to a time-varying component of the impulse responses in Fig. 9.

- *Clustering of scatterers* – This method assigns each scatterer to a cluster, where a *cluster* is defined to be a group of scatterers located a similar points in space. The clustering is based on a the modified K-means approach of [14].

Further analysis showed that scatterers belonging to the same cluster reflected radiation in a similar way, which can be well described by *beampatterns* pointing into specific directions.

3 Channel Model Description

This section is devoted to the description of the channel model concepts. We start with the general overview and qualitative comments, and then proceed, with a more comprehensive and quantitative description of each of the modeling approaches in separate subsections.

Our model is fundamentally a geometry-based stochastic channel model (GSCM), as introduced in [15]. This means that each realization of the channel is obtained by firstly choosing the location and power of the scatterers stochastically (creating a static geometrical map), and then the impulse response of the different MS positions is obtained by means of a simplified ray tracing where the different MPCs are superimposed at the receiver.

A single channel realization is characterized by a geometrical map, composed of static scatterers, from which several impulse responses (from the different MS positions) can be calculated.

A fundamental assumption of our model is that we only consider single-scattering processes. While being a simplification, single-scattering was found to describe the greater part of the channel impulse response. This is evidenced by the fact that the locations of the clusters of scatterers, which are determined *under the assumption of single-scattering*, could on the whole be mapped to physical objects in the measured scenarios, e.g., gas pumps and pillars. The dominance of single-scattering was thus found to be a distinct property of these scenarios. While multiple-scattering processes still exist, they are associated with radiation carrying only low power. We include those contributions in the diffuse component.

A general equation for the transfer function of the modeled channel is thus

$$H_n(f) = \left(\overbrace{S_{\mathrm{LOS},n}(f)}^{I} + \overbrace{\sum_k S_{n,k}(f)}^{II} + \overbrace{\mathcal{F}\{D_n(\tau)\}}^{III} \right) \overbrace{\frac{f^{-m}}{F}}^{IV}. \quad (1)$$

The index n identifies the different MS positions, such that $n = 1, \ldots, N_{\mathrm{MS}}$. The main constituents of channel model are:

I – the *quasi-LOS component*, with transfer function $S_{\mathrm{LOS},n}(f)$, which is calculated deterministically from the distance dependent path-loss and is also affected by the shadow effects,

II – the *discrete multipath components (MPC)*, with transfer functions $S_{n,k}(f)$, which are derived from the spatial position of the scatterers, the radiation pattern of the corresponding clusters, and the path-loss,

III – the *diffuse component*, which is defined by a deterministic large-scale attenuation superimposed on a purely statistical small-scale fading ($\mathcal{F}\{\cdot\}$ stands for the Fourier transform operation) and

IV – the *frequency dependency*, which models the frequency dependence of the *average* magnitude of the transfer function that occurs in UWB channels [3]. F is a normalization factor used to ensure that f^{-m} does not affect the frequency-integrated power of the channel's transfer function..

The detected scatterers were found to be arranged in clusters and this fact needs to be reflected by the model. We therefore distinguish between the inter-cluster properties (e.g., the statistics of the cluster center locations), and the intra-cluster properties, i.e., the location of scatterers *within* a cluster.

In the course of the model development, we often had to establish which pdf best describes a particular model parameter. For this model selection, we followed the recent work of Schuster [16] and employ the Akaike Information Criteria (AIC), or more specifically, its normalized version, the Akaike weights. This was found to be preferable to the more traditional goodness-of-fit (GOF) tests, which have subjective significance levels. The basic idea behind AIC is "... the maximization of the expected log likelihood of a model determined by the method of maximum likelihood" [17].

Note that in this section, we present only the functional shape of the pdfs of the scatterers. The actual numerical values parameterizing those pdfs will be presented in Section 4.

3.1 Type and Number of Clusters and Scatterers

Since the BS was always placed on a structure of large dimensions (e.g. a wall or pillar), we found that one cluster surrounding the BS always existed. This cluster was characterized by having a larger number of scatterers than the remaining clusters: on average the number of scatterers per BS cluster was 129 and for non-BS clusters it was 26. For this reason, we model these two types of clusters separately.

The number of clusters, N_{cl}, was found to be well modeled by a Poisson distribution in accordance with the literature [9]. The number of scatterers per cluster, N_{sc}, could best be described by a discrete version of the Gaussian distribution truncated to positive outcomes.[10]

3.2 Cluster Positions

We model the distribution of the cluster coordinates (i.e. the coordinates of the cluster center) as a two-dimensional uniform distribution. This is clearly an oversimplified picture, since the layout of a gas station (lines of gas pumps, etc.) gives rise to a more regular structure. Nevertheless, for want of a better model, we employ this uniform distribution in the following, while noting that the cluster location can be adapted based on future measurements, or even based on location-specific geometrical information, in the spirit of [10].

In the model, the clusters are only allowed to exist within a finite area surrounding the BS and MS antennas. The delimitation of this area is found from the delay of the furthest cluster detected from the measurements, which was $\tau_{c,max} = 128$ ns. Thus, the cluster location pdf is uniform within an ellipse whose foci are the BS and center MS position, being defined as,

$$f_{uniform}(x', y') = \begin{cases} \frac{1}{\pi \alpha_e \beta_e} & , \frac{x'^2}{\alpha_e^2} + \frac{y'^2}{\beta_e^2} \leq 1 \\ 0 & , \text{otherwise} \end{cases}. \tag{2}$$

The auxiliary coordinate system (x', y') is used here to facilitate the formulation of the distribution. The x'-axis is oriented along the line that connects the BS to the center MS position, and the origin $(x', y') = (0, 0)$ lies on the mid point of that line. The ellipse's semimajor axis is $\alpha_e = \tau_{c,max} c/2$ and the semiminor axis is $\beta_e = \sqrt{\alpha_e^2 + d_{\text{foci}}}$, where d_{foci} is the distance between the two ellipse's foci and c is the speed of light in vacuum. Fig. 8 shows the *allowed cluster area*, where the foci are the BS and the center MS position.

[10] Due to the lack of a physical reasoning or existing literature that would indicate a certain statistical description for these parameters, we compared the histogram of the data with several distribution and chose the one that best matched the data.

3.3 Scatterer Positions Within a Cluster

From inspection of plots of scatterer locations, we note that the density of scatterers decreases with distance to the cluster's centroid. We could furthermore see by inspection that the density is rotationally symmetric, which suggests the use of a bivariate pdf for the two spatial coordinates (x_s, y_s) around the centroid. The pdfs along the two coordinate axes are assumed to be uncorrelated with the same variance, such that the scatterers will be equally spread around the cluster centroid.

The next step is to identify a good distribution to describe the variations of the x_s and y_s coordinates. To this end, we tested the bivariate Gaussian and Laplace distributions. The main difference between the two candidates is that the Laplacian is highly peaked at the origin and falls off less quickly than the Gaussian at large distances from the centroid. The model selection was based on the Akaike weights, which were computed for both distributions and showed the bivariate Laplace distribution to be the better fit to the measurement results. This distribution is defined as [18],

$$f_{Laplace}\left(x_{s'}, y_{s'}\right) = \frac{1}{\pi\kappa} K_0\left(\sqrt{\frac{2}{\kappa}\left(x_{s'}^2 + y_{s'}^2\right)}\right), \tag{3}$$

where κ is the parameter of the distribution and $K_0(\cdot)$ is the zero-th order modified Bessel function of the second kind. Note that this is the distribution of the coordinates within a cluster, the true coordinates (with the BS as the origin) are $(x_s, y_s) = (x_{s'} + x_c, y_{s'} + y_c)$, where (x_c, y_c) are the cluster centroid coordinates.

3.4 Scatterer's Power

On average, the power received via the different scatterers decreases with the *run-length* of the signal, namely following a power law

$$P_{\mathrm{PL}}\left(d_{t:s:r}\right) = P_0\left(d_{t:s:r}/d_0\right)^{-n_{\mathrm{PL}}}. \tag{4}$$

Here, n_{PL} is the path-loss exponent, $d_{t:s:r}$ is the distance from the transmitter, through a given scatterer to the receiver, and P_0 is the mean power at the reference distance d_0. The fit of d_0 and P_0 to the measurement results was done in the least-squares sense, based on all the MPCs excluding the direct LOS component.[11] Since for very small distances, the above equation would

[11] The path-loss of the LOS component is modeled separately in Section 3.7 since it does not include an interaction with scatterers.

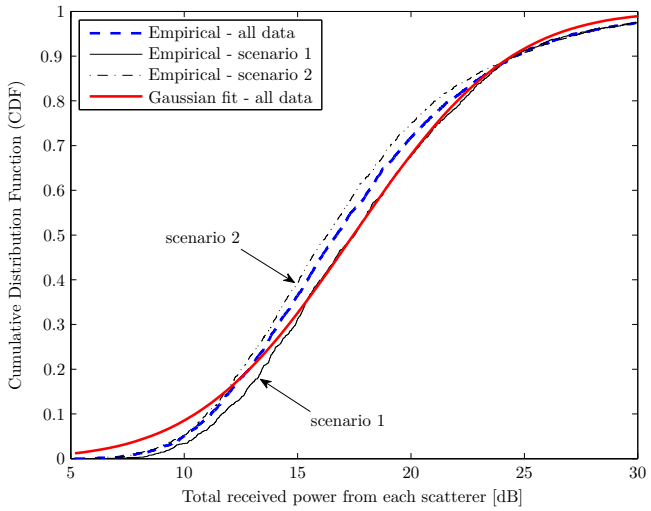

Figure 1: Log-normal total received power variations of the scatterers after path-loss compensation. The two thin lines correspond to the data from scenario 1 and 2 separately.

stop being valid (as $d_{t:s:r} \to 0, P_{\mathrm{PL}} \to \infty$), only $d_{t:s:r} \geq d_0$ are considered, where the reference distance is $d_0 = 1$ m.

The power law described above describes only the *mean* power of the MPCs; however, individual components show a variation around this mean. These power deviations, p_s, were found to be well modeled by a log-normal distribution, which when plotted in dB scale is transformed into a Gaussian distribution. Their empirical CDF and corresponding Gaussian fit are shown in Fig. 1.

It is noteworthy that this power law (plus lognormal deviations) is different from the conventional power law for the pathloss [19]. The conventional model ascribes a d^{-n} law to the *total* received power (not to the MPC powers, as in our case), and furthermore defines d as the distance between transmitter and receiver, not the runlength of the signal.

3.5 Visibility Regions of Clusters

From the measurements, we observed that specific scatterers could not be observed at all the measurement positions of the MS. Most often, a given scatterer was visible only if the MS was in a certain region (called visibility region). The

transitions from being visible to not being visible (as the MS position changed continuously) were sometimes abrupt and on other occasions gradual.

The concept of visibility regions was introduced (for conventional wideband channels) by the COST259 Directional Channel Model [20, 21, 22]. It defines regions in space associated with a certain scatterer cluster such that a corresponding cluster becomes visible if the MS happens to be within the region. It also provides a transition function to describe the activation of the cluster when the MS enters the visibility area. An alternative approach was formulated in [23], using not the spatial but rather the angular domain: each cluster is ascribed an angle-dependent radiation pattern. In the currently proposed model we choose the latter approach. This is in line with our initial study of the measured clusters, when we looked at their angular radiation pattern.

As reported at the end of Section 2, these patterns were found to have *beam*-like shapes. We tested two candidate shapes to describe the radiation patterns that also have *beam*-like properties, namely a (truncated) Gaussian and raised- cosine functions. The main difference between them is that the latter has a limited width beyond which all angles have zero response, while the former has non-zero values for all angles. Fig. 2 shows an example of a measured radiation patterns and the corresponding fits. To choose the best shape parameters we minimized the mean square error (MSE),

$$\nu_{opt} = \arg\min_{\nu} \frac{1}{N} \sum_{n=1}^{N} \left(R_{\phi_n} - R'_{\phi_n}(\nu) \right)^2,$$

where R_{ϕ_n} is the measured radiation pattern[12] after path loss compensation, $R'_{\phi_n}(\nu)$ is the shape to be tested, N is the number of measurement points and ϕ_n is the angle between the horizontal line passing through the cluster and the line connecting the cluster to the n-th MS position. The variable over which the minimization is performed is ν. For the Gaussian case, 2ν is the pulse width at an amplitude of $1/e$, and for the raised cosine case, ν is the pulse width at an amplitude of $1/2$. Both shapes plus measured radiation pattern are normalized to a maximum amplitude of 1 and centered at the angle providing amplitude. By fitting these two shapes to all the 52 measured clusters, we found that the average MSE for the Gaussian was 3.35×10^{-2} and the average MSE for the raised cosine was 3.62×10^{-2}. Hence, the Gaussian shape is superior in the MSE sense, although the difference between the two is small. The Gaussian

[12]The measured radiation pattern of a cluster is found from the averaging of all the individual scatterers' patterns that constitute that cluster, [2].

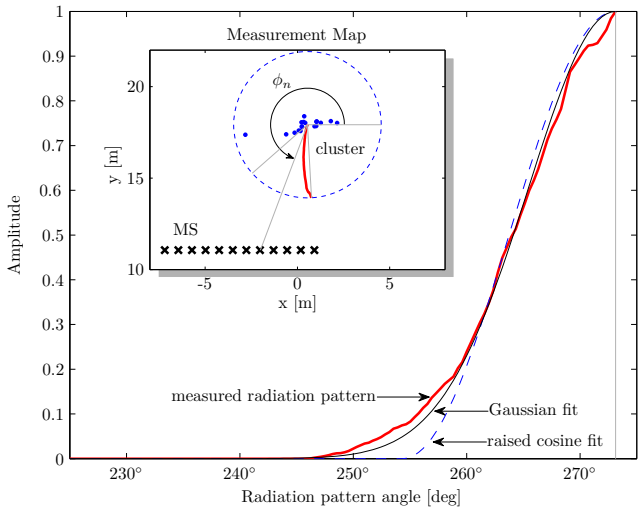

Figure 2: Example of a measured cluster's radiation pattern with the corresponding Gaussian and raised cosine fits. The small figure shows the geometrical map containing the position of the cluster and all the MS positions, plus the measured radiation pattern plotted in polar coordinates.

shape is defined here as

$$V(\phi) = \exp\left(-\frac{(\phi-\phi_0)^2}{\nu^2}\right), \tag{5}$$

where $V(\phi)$ is only defined for $\phi_{min} \le \phi \le \phi_{max}$, and the limits are given by the cluster and MS position as illustrated in Fig. 3. The shape is controlled by the parameters, ϕ_0 ($\phi_{min} \le \phi_0 \le \phi_{max}$) and ν ($\nu > 0$). The former specifies the main direction of the radiation beam, modeled as uniformly distributed within the available angular range, and the latter gives information about how focused the beam is, and is assumed to follow a log-normal distribution.[10] The parameters for these pdfs were estimated from the 52 measured clusters.

Our definition also intrinsically states that all created clusters are visible in *some* region. This is reasonable, since the non-visible clusters are impossible to detect during measurements, and there is no information about them. Finally, assigning a radiation pattern to a cluster means that we expect all scatterers from that cluster to share the same radiation pattern.

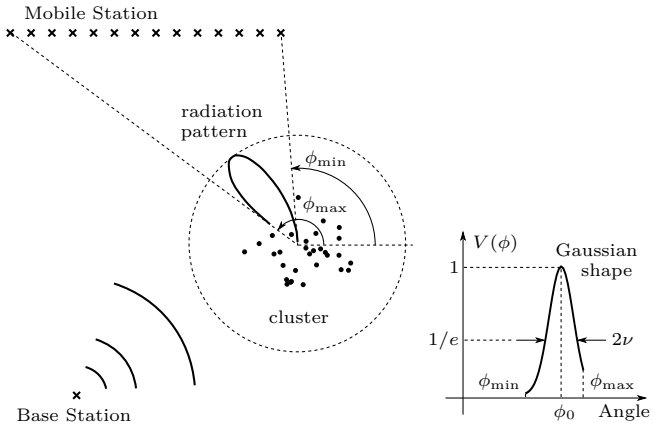

Figure 3: Definition of visibility region from the cluster's radiation pattern. On the left, a map view representation with the radiation pattern in polar coordinates, and on the right, the same in cartesian coordiantes.

3.6 Shadow Regions

In the measured scenarios, there were locations at which the LOS between the transmitter and receiver antennas was obstructed. A simple analysis to the data revealed that, in some cases, the shadowing by a single object was responsible for a loss of 13 dB of the overall impulse response power. Simply distinguishing between "LOS" and "NLOS" cases, as often done in the literature, does not provide the important information about the dynamic channel evolution as an MS moves from a shadowed to an unshadowed region. There is therefore a need for *shadow regions* in the model.

The above mentioned obstruction was generally due to gas pumps, pillars or other objects of comparable size. Since our measurement routes (virtual arrays) were long enough, we were able to identify the beginning and end of several shadowing processes. This enabled us to study and model how the received signal fades behind objects.

As explained in [2, IV-B], diffraction theory provides a good explanation for specific shadowing effects. However, introducing diffraction equations into our model would make it far too complex. Furthermore, from our measurements, we were only able to identify 18 shadow regions, which is insufficient to build a statistically relevant yet detailed model for the corresponding signal variations. Due to these reasons, we selected a very simple quadratic shape to an angular shadowing region (beampattern) to describe the signal variations, which captures the main effect of shadowing, namely the reduction of the signal

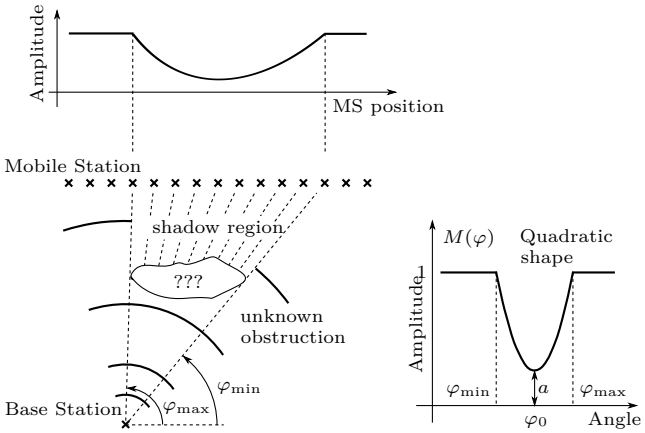

Figure 4: Definition of the shadow region as a quadratic shape in the angular domain. The plots show the normalized received signals strength without the influence of path loss. The upper plot, in the *MS position* domain and the lower one, in the *angular* domain.

amplitude behind objects. More precisely, we define the shadow region, cf. Fig. 4, by the mask,

$$M(\varphi) = \begin{cases} (1-a)\left(2\frac{\varphi-\varphi_0}{\Delta\varphi}\right)^2 + a & ,\varphi_{\min} \le \varphi \le \varphi_{\max} \\ 1 & ,\text{otherwise} \end{cases} . \tag{6}$$

The shadow region angular width is defined as $\Delta\varphi = 2(\varphi_{min} - \varphi_0)$, where φ_0 is the mid-angle between φ_{max} and φ_{min}. The parameter a is used to control the maximum signal loss which happens when the MS is exactly behind the object. The term *mask* is used here because (6) will be applied, as a multiplicative mask, to the LOS component (15) and to the scatterer components belonging to the BS cluster in (14). The shadow effect is also illustrated in Fig. 9.

The parameter φ_0 is modeled as a random variable that is uniformly distributed over the available angular range and a and $\Delta\varphi$ are constants estimated from the measurements of the 18 available shadow regions.

Finally, the number of shadow regions found from our 8.11 m virtual array, $N_{sh,8}$, is modeled by a Poisson distribution.[10] The density of shadow regions can be found by normalizing the number of shadow regions by the array length, $N_{sh,8}/8.11$.

3.7 Line-Of-Sight Power

The power of the LOS component as a function of distance also needs to be quantified. By LOS component we mean the UWB pulse that propagates from one antenna to the other without any obstruction. The standard model suggests that the LOS power follows a power-law

$$P_{\mathrm{LOS}}\left(d_{t:r}\right) = P_0\left(d_{t:r}/d_0\right)^{-n_{\mathrm{LOS}}}, \tag{7}$$

where P_0 is the LOS power at the reference distance d_0, chosen to be $d_0 = 1$ m, and $d_{t:r}$ is the distance between the transmitter and a given receiver position.

It is well known that the free space path-loss for spherical waves in the far-field is proportional to the inverse of the distance squared. However, estimates from the measured data gave $n_{\mathrm{LOS}} = 1.67$. This result indicates that the LOS component might be influenced by other components that cannot be resolved from the LOS component because their delays are too similar.

3.8 Diffuse Multipath Component

The discrete components associated with particular scatterer locations cannot explain all the power experimentally observed in the impulse responses. The remainder can be described as diffuse multipath component (DMC) and it often results from processes like multiple-scattering, rough surface scattering and diffraction around objects. Since these components have low power, are numerous and originate from all directions surrounding the antennas, an attempt to model them on a geometrical basis would result in an overly-complex channel model; we therefore choose a purely stochastic description.

The data from which we extract the DMC characteristics is the remainder of the impulse response *after* the application of the scatterer detection method, briefly described in Section 2. In every step of the method, discrete scatterer contributions were detected and subtracted, so that the remaining *cleaned* channel is assumed to be free of specular components, with only the DMC being left. The detection method may also have generated cleaning artifacts, which become subsumed into the modeled DMC.

It is a common assumption that the DMC power, on average, decays exponentially as a function of delay, starting immediately after the LOS component (zero excess delay) [24]. Hence, a sufficient description of the average behavior of the DMC power is obtained by estimating its decay exponent (or correspondingly, its rms delay spread) and its level of power at zero excess delay. In order to capture all the dependencies of the DMC, we model these two parameters as a function of the distance between the antennas, $d_{t:r}$.

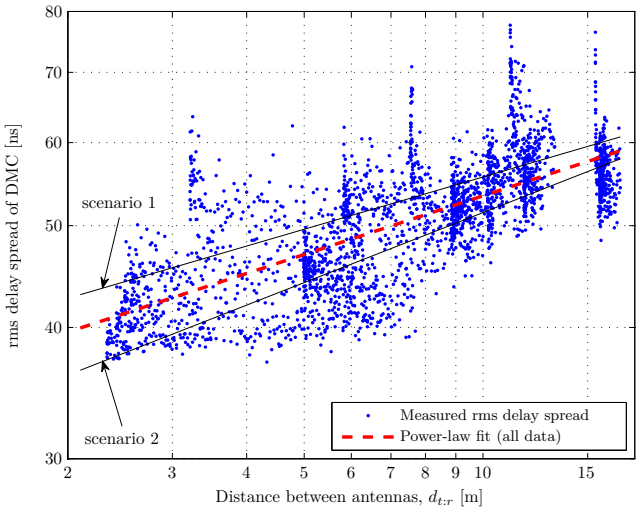

Figure 5: Exponent of the diffuse multipath component versus distance. The thin lines show the fit to the data from scenario 1 and 2 separately.

While the rms delay spread dependence on the distance has been previously studied for full impulse responses [25], we apply the same principles to the DMC only, c.f. Fig. 5. The large-scale DMC power is then fully described by,

$$D_{\mathrm{LS}}(\tau) = \begin{cases} D_{\tau_{\mathrm{LOS}}}(d_{t:r}) \exp\left(-\frac{\tau-\tau_{\mathrm{LOS}}}{\tau_{\mathrm{RMS}}(d_{t:r})}\right) & ,\tau > \tau_{\mathrm{LOS}} \\ 0 & ,\tau \leq \tau_{\mathrm{LOS}} \end{cases} \tag{8}$$

where the power at zero excess delay, in linear scale, is defined as,

$$D_{\tau_{\mathrm{LOS}}}(d_{t:r}) = D_0 \left(d_{t:r}/d_0\right)^{-n_{\mathrm{D}}} \tag{9}$$

and the rms delay spread of the DMC is,

$$\tau_{\mathrm{RMS}}(d_{t:r}) = \tau_0 \left(d_{t:r}/d_0\right)^{n_{\mathrm{RMS}}} . \tag{10}$$

The parameters D_0, n_{D}, τ_0 and n_{RMS}, were estimated from all the 2720 *cleaned* channel responses.

We next analyze the amplitude statistics of the DMC's small-scale fading, as a function of the excess delay. The 170 different MS locations constitute the statistical ensemble from which we can obtain the pdf, while the delay is considered a deterministic parameter on which the pdf can depend. We note that for each delay value we normalize the signal such that it has unit mean

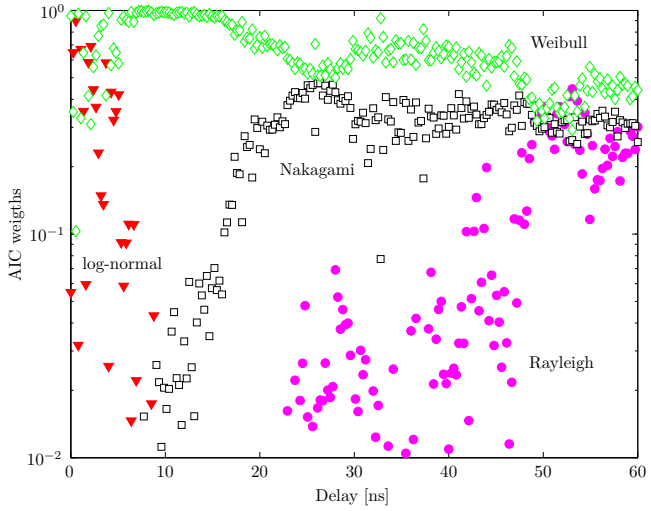

Figure 6: Akaike weigths of the four candidate distributions to describe the DMC small-scale variations as a function of delay.

power. Then, five candidate distributions were considered for the amplitude pdf, whose parameters were calculated based on ML estimates: log-normal and Rayleigh by their closed form expressions, Rician by a grid search maximizing the log-likelihood function with a step size of 10^{-4}, Nakagami by an approximate ML estimator [26] and Weibull by a numerical method finding the zero of the partial derivatives of the log-likelihood function with an error below 10^{-5} [27]. Again we use the Akaike weights for the model selection. Fig. 6 shows the weights (on a logarithmic scale) versus delay.[13]

From the figure, it can be observed that for small excess delays, both Weibull and log-normal are the preferred distributions. Then, with increasing delay, the log-normal distribution starts to perform worse, while Nakagami and Weibull are the best. Also with increasing delay, the data progressively becomes more "Rayleigh-like". Since the Weibull distribution is (among the) best fit over the whole delay range, we choose it to model the small-scale fading of the DMC amplitude, $D_{\mathrm{ss}}(\tau) \sim f_{Weibull}\,(\alpha, \beta(\tau))$.[14]

The Weibull distribution is defined by the *scale parameter* α and the *shape parameter* β, where the latter one is comparable to the m-parameter of the

[13] Since the Rician weights were very similar to the Rayleigh ones, these are not shown in the figure for clarity.

[14] The τ dependence is explained in the following paragraphs.

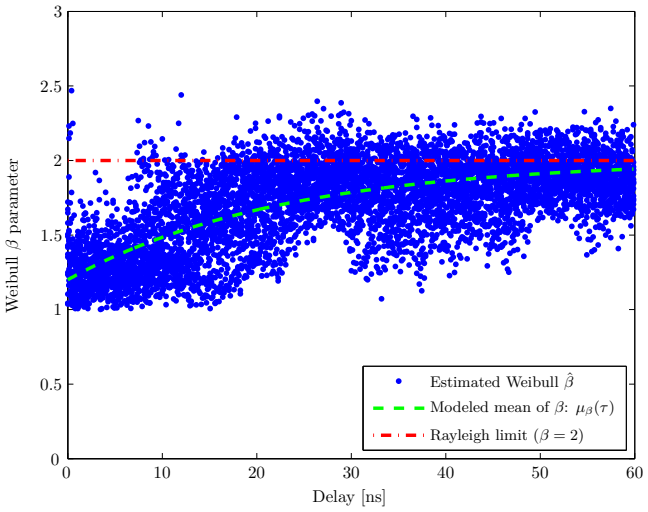

Figure 7: Estimated Weibull $\hat{\beta}$ parameter as a function of delay and corresponding modeling.

Nakagami distribution. Fig. 7 shows the estimated values of β. The values of β below 2 represent a fading worse than Rayleigh. From Fig. 11, one can observe that indeed the data approaches Rayleigh with increasing delay $\beta \to 2$ as $\tau \to \infty$. To capture the essence of this behavior, we empirically model the β parameter as a delay dependent variable defined by,

$$\beta(\tau) = 2 + \frac{u-2}{(\tau+1)^v}. \tag{11}$$

Here, u defines the mean value of β at $\tau = 0$ and v controls the curvature of the line as it tends to $\beta = 2$. The value of both the parameters was estimated by minimizing the mean square error from the data in Fig. 7. At first glance, one might attribute the Rayleigh-like amplitude statistics at large delays to measurement noise; however, the power of the DMC at 60 ns was, on average, calculated to be 15 dB above the noise power, and therefore, the noise influence in $\hat{\beta}$ is minimal. The bias of the estimator for the Weibull parameters in the presence of noise, considering the 170 samples, was calculated to be below 0.025 for all delays and thus neglected. Finally, the Weibull α parameter can be deterministically calculated since it is a function of both β and the mean power. Since the mean power was normalized to one, it here simplifies to,

$$\alpha = \beta \left[\Gamma\left(1 + 2/\beta\right)\right]^{\beta/2}, \tag{12}$$

where Γ is the Gamma function. Regarding the phase of the DMC taps θ_{DMC}, all our tests revealed it to be uniformly and independently distributed from 0 to 2π.

3.9 Frequency Dependent Decay

Finally, we have also studied the frequency dependence of the pathloss, which is one of the distinguishing characteristics of the UWB channels compared to narrow-band ones. This characteristic requires us to use a frequency dependent term, f^{-m}, into our model, see Eq. (1). This is a simplified approach since, in real scenarios, each received pulse can have its own decay exponent [28], nevertheless since these individual exponents are difficult to estimate we opt for a general decay exponent as in [10]. In order to estimate the value of m, we calculated the exponent of each individual frequency response and averaged over that ensemble which resulted in $m = 0.95$. This is in line with the results found in [10] and [9].

4 Building the Impulse Response

In this section we provide step-by-step instructions on how to implement the proposed channel model. All the necessary parameters and corresponding estimated values are given in Table 1, for random parameters, and in Table 2, for deterministic parameters.

Since the virtual array used in the channel measurements was 8.11 m long, the model is only valid for MS positions covering distances up to this length. Similarly, the distance between BS and MS must be within 2 to 19 m. Figures 8 and 9, illustrate an example of a geometrical map and the corresponding channel impulse responses, respectively. The figures were generated using the same parameters as used in the measurements, e.g., same number of MS positions and separation distance between them. In the mathematical formulations given below, n indexes a given MS position (a "cross" in Fig. 8) and k indexes a specific scatterer (a "point" in Fig. 8). The model can then be built has follows

1. Choose the distance of the center MS with respect to the origin (BS) $d_{\text{BS:MS}}$, from a uniform distribution. Place the MS positions in a straight line (covering up to 8.11 m).

2. Choose the number of clusters N_{cl} from a Poisson distribution and add one (the BS cluster) to the result. For each, choose a corresponding number of scatterers N_{sc}, from a discrete Gaussian distribution.

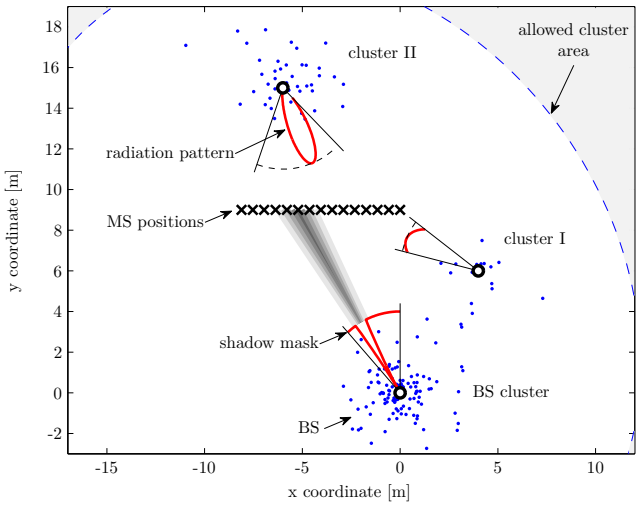

Figure 8: Geometrical map from one specific channel model realization. The radiation patterns are positioned on the centroids of the corresponding clusters. For clarity, only 15 of the 170 MS positions are shown.

3. Place the cluster center locations, (x_c, y_c), according to a uniform distribution within an ellipsoid, (2).

4. Position the scatterers within a cluster ensuring that their coordinates, (x_{s_k}, y_{s_k}), follow a 2D Laplacian distribution, (3).

5. For the case of scatterers belonging to *non-BS clusters*, define their contribution over the n-th MS position by,

$$\underset{non\text{-}BS}{S_{n,k}(f)} = \sqrt{P_{\mathrm{PL}}(d_{t:s_k:r_n})p_{s_k}} \cdot \frac{V_k(\phi_n)}{V_{\mathrm{norm},k}} \cdot e^{-j(2\pi f \tau_{n,k}+\rho_k)}, \qquad (13)$$

where $P_{\mathrm{LS}}(d_{t:s_k:r_n})$, (4), is the path-loss power calculated form the total propagation distance, p_{s_k} is the log-normally distributed total scatterer power, $V_k(\phi_n)$, (5), is the Gaussian shaped radiation pattern of the cluster owning the scatterer, $V_{\mathrm{norm},k}$ is a normalization variable that must be calculated to ensure that $V_k(\phi_n)$ does not scale the scatterer's total power, $\tau_{n,k}$ is the propagation delay through the scatterer assuming propagation at the speed of light c, and ρ_k is scatterer's phase, uniformly distributed from 0 to 2π.

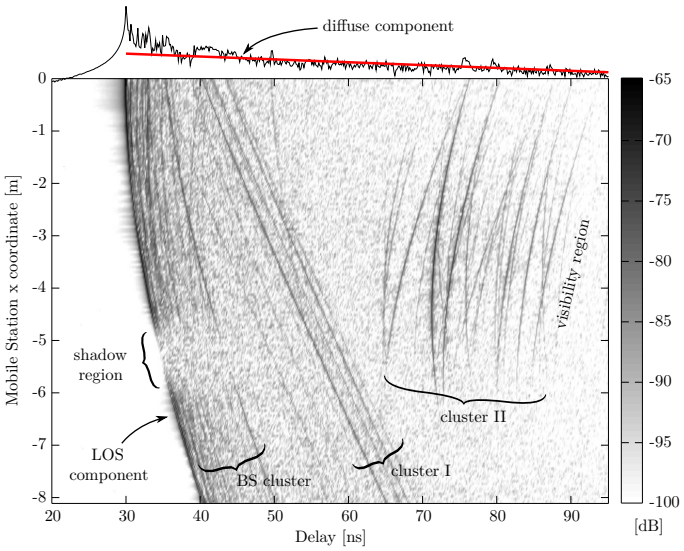

Figure 9: Simulated channel based on the geometrical map given in Fig. 8. The main model components are identified. The figure compromises 170 impulse responses, each separated by 0.048 m.

6. For the case of scatterers belonging to the *BS cluster*, define their contribution over the n-th MS position by,

$$\underset{BS}{S_{n,k}}(f) = \sqrt{P_{\text{PL}}(d_{t:s_k:r_n})p_{s_k}} \cdot M(\varphi_n) \cdot e^{-j(2\pi f \tau_{n,k}+\rho_k)}. \tag{14}$$

   In this case, the radiation pattern is replaced by the shadow mask $M(\varphi_n)$ (6). This can be seen from Fig. 8 by comparing the radiation of each cluster clusters (the red lines).

7. Define the LOS component (which does not include any interaction with scatterers) by

$$S_{\text{LOS},n}(f) = \sqrt{P_{\text{LOS}}(d_{t:r_n})} \cdot M(\varphi_n) \cdot e^{-j2\pi f \tau_{\text{LOS},n}}, \tag{15}$$

   where $P_{\text{LOS}}(d_{t:r_n})$, (7), is the LOS power at antenna distance $d_{t:r_n}$ and $\tau_{\text{LOS},n}$ is the LOS propagation delay.

8. Determine the contribution DMC by,

$$D_n(\tau) = \sqrt{D_{\text{LS},n}(\tau)} \cdot D_{\text{SS}}(\tau) \cdot e^{j\theta_{\text{DMC}}} \tag{16}$$

where $D_{\mathrm{LS},n}(\tau)$, (8), is the large-scale deterministic diffuse power, $D_{\mathrm{SS}}(\tau)$ is the Weibull distributed small-scale variations of the DMC envelope, and θ_{DMC} is the uniformly and independently distributed tap phase. The definition of $D_{\mathrm{SS}}(\tau)$ and θ_{DMC} is based on a uniform discretization of the delay domain, $\tau = 0, \delta t, 2\delta t, \ldots$, where δt is the inverse of the system bandwidth. Its frequency domain representation can be calculated by the Fourier transform operation,

$$D'_n(f) = \mathcal{F}\left\{D_n(\tau)\right\}. \tag{17}$$

9. Finally, add together all the above components, and apply the frequency dependency term, to get the complete channel frequency response,

$$H_n(f) = \left(S_{\mathrm{LOS},n}(f) + \sum_k S_{n,k}(f) + D'_n(f)\right)\frac{f^{-m}}{F}. \tag{18}$$

Applying a Fourier transform to (18) results in the (time domain) impulse response of the channel, which is depicted in Fig. 9. The effect of shadow and visibility regions is clearly visible from the figure.

5 Model Validation

The validation is an important step in any model development. Here, we validate the proposed model based in two distinct approaches. Firstly, we show that parameters derived from the model (but not directly used to parameterize it) agree well with the equivalent parameters directly computed from the measurements. An example of this is the rms delay spread, τ_{rms}, which is plotted in Fig. 10. Measured and simulated lines agree both in the mean and variance. As a comparison with existing models, we find that our mean τ_{rms} of 25 ns, is in accordance with the 29 ns τ_{rms} calculated from the standardized channel model IEEE 802.15.4a CM5 for outdoor LOS [9].

Secondly, we investigate whether the model might be suitable to describe a general gas station scenario. In order to do so, we compare the estimated parameters from the two different measured gas stations. Fig. 1 and 5 present estimated parameters when using the data from each scenario. Lastly, in Fig. 10 we also added the delay spreads of our model applied separately to scenario 1 and 2. They do not differ significantly, which supports the idea that this model has a general applicability for these kind of scenarios, though clearly a larger number of gas stations would have to be measured to provide statistically significant confirmation of this conjecture.

Table 1: List of all random parameters.

Random Variable	Symbol	Unit	Distribution	Reference	Cluster Type	Parameter Values
Distance between BS and center MS	$d_{\text{BS:MS}}$	m	uniform	[13, 4-46]	–	$a = 2$ $b = 19$
No. of clusters	N_{cl}	#	Poisson	[13, 4-57]	non-BS	$\lambda = 3.25$
No. of scatterers within a cluster	N_{sc}	#	*discrete* Gaussian	[13, 4-25]	BS	$\mu = 129$ $\sigma^2 = 2193$; $N_{sc} \geq 0$
					non-BS	$\mu = 26$ $\sigma^2 = 394$; $N_{sc} \geq 0$
Cluster coordinates	(x_c, y_c)	m	2-D uniform	(2)	non-BS	$\tau_{c,max} = 1.28 \cdot 10^{-7}$
Scatterer coordinates within a cluster	(x_s, y_s)	m	2-D Laplace	(3)	BS	$\kappa = 1.45$
					non-BS	$\kappa = 2.49$
Scatterer local power variations	p_s	dB	Gaussian	[13, 4-25]	all	$\mu = 17.46$ $\sigma^2 = 29.63$
Visibility radiation pattern direction	ϕ_0	rad	uniform	[13, 4-46]	non-BS	$a = \phi_{\min}$ $b = \phi_{\max}$ (Fig. 3)
Visibility radiation pattern width	ν	rad	log-normal	[13, 5-30]	non-BS	$\mu = -0.24$ $\sigma^2 = 0.55$
No. of shadow regions (8 m array)	$N_{sh,8}$	#	Poisson	[13, 4-57]	BS	$\lambda = 1.27$
Shadow region direction	φ_0	rad	uniform	[13, 4-46]	BS	$a = \varphi_{\min}$ $b = \varphi_{\max}$ (Fig. 4)
DMC small-scale envelope variations	D_{SS}		Weibull	[13, 4-43]	–	$\alpha =$ Eq. (12) $\beta =$ Eq. (11)
DMC tap phase	θ_{DMC}	rad	uniform	[13, 4-46]	–	$a = 0$ $b = 2\pi$
Scatterer phase	ρ	rad	uniform	[13, 4-46]	–	$a = 0$ $b = 2\pi$

Table 2: List of all deterministic parameters.

Deterministic Variable	Symbol	Unit	Reference	Cluster Type	Values/Parameters
No. of MS positions	N_{MS}	#		–	170
Distance between MS positions	Δd_{MS}	m		–	0.048
No. of frequency points	N_f	#		–	1601
Minimum frequency	$f_{\min}$	Hz		–	$3.1 \cdot 10^9$
Maximum frequency	$f_{\max}$	Hz		–	$10.6 \cdot 10^9$
Frequency step/resolution	δf	Hz		–	$4.69 \cdot 10^6$
Delay step/resolution	δt	s		–	$133.3 \cdot 10^{-9}$
Propagation speed	c	m/s		–	$3 \cdot 10^8$
Shadow region loss coefficient	a		(6)	BS	0.064
Shadow region width	$\Delta\varphi$	rad	(6)	BS	0.11
Scatterers' power path-loss	$P_{\mathrm{PL}}(d_{t:s:r})$		(4)	all	$P_0 = -74.6$ $n_{\mathrm{PL}} = 1.38$ $d_0 = 1$; $d_{t:s:r} \geq d_0$
Power of LOS component	$P_{\mathrm{LOS}}(d_{t:r})$		(7)	–	$P_0 = -57.34$ $n_{\mathrm{LOS}} = 1.65$ $d_0 = 1$; $d_{t:r} \geq d_0$
Power of DMC at LOS	$D_{\tau_{\mathrm{LOS}}}(d_{t:r})$		(9)	–	$D_0 = 2.36 \cdot 10^{-9}$ $n_{\mathrm{D}} = 1.28$ $d_0 = 1$; $d_{t:r} \geq d_0$
rms delay spread of DMC	$\tau_{\mathrm{RMS}}(d_{t:r})$		(10)	–	$\tau_0 = 3.31 \cdot 10^{-8}$ $n_{\mathrm{RMS}} = 0.21$ $d_0 = 1$; $d_{t:r} \geq d_0$
Frequency decay exponent	m		(18)	–	0.95

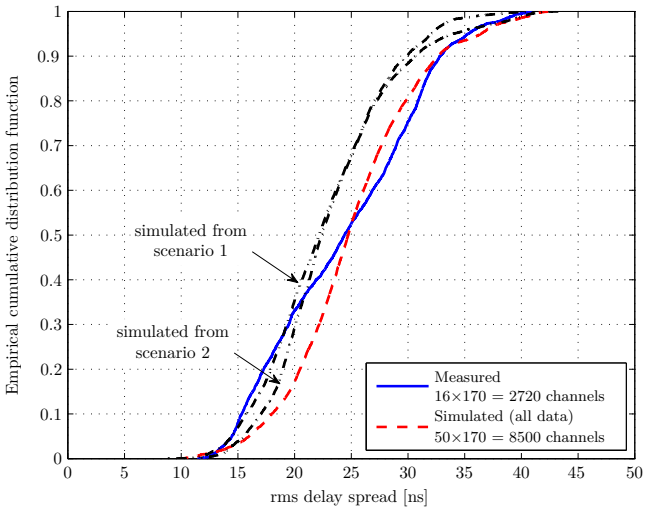

Figure 10: CDFs of the rms delays spreads of both the measured and simulated impulse responses. The two "arrow indicated" lines correspond to the rms delay spreads calculated from the proposed channel model based separately in the data from scenario 1 and 2.

6 Conclusions

In this paper, we have specified one of the few existing UWB channel models for outdoor scenarios. The aim here was to characterize the static channel, however, real situations will often include moving vehicles and people, which can result in additional time/space varying clusters of scatterers and/or shadow regions. While not including these channel effects, our model is well prepared to integrate them since it has a geometric-stochastic basis (e.g. a car could be described by a moving cluster in our geometrical space with varying radiation properties). Such improvements would also require further measurements and possibly more complex detection algorithms.

Besides the importance of this work for infostation systems, a number of modeling concepts were also introduced: (i) cluster radiation patterns defining the cluster's visibility region, and (ii) shadowing regions that represent the large-scale attenuation of the LOS for certain TX/RX locations, and (iii) the Laplacian distributed scatterer coordinates within clusters. These concepts were found to be of great help for the modeling of the outdoor UWB channel and it is of interest to verify if the same holds true for indoor UWB or even for

narrow-band channels.

Acknowledgments

The authors would like to thank the reviewers of this manuscript for their constructive remarks, which greatly helped to improve the presentation of the material.

References

[1] R. Frenkiel, B. Badrinath, J. Borres, and R. Yates, "The infostations challenge: Balancing cost and ubiquity in delivering wireless data," *IEEE Personal Communications*, vol. 7, no. 2, pp. 66–71, 2000.

[2] T. Santos, J. Karedal, P. Almers, F. Tufvesson, and A. F. Molisch, "Modeling the ultra-wideband outdoor channel – Measurements and parameter extraction method." submitted to IEEE Transactions on Wireless Communications, 2009.

[3] A. F. Molisch, "Ultrawideband propagation channels-theory, measurement, and modeling," *IEEE Transactions on Vehicular Technology*, vol. 54, pp. 1528–1545, Sept. 2005.

[4] A. F. Molisch, "Ultrawideband propagation channels and their impact on system design," in *Proc. International Symposium on Microwave, Antenna, Propagation and EMC Technologies for Wireless Communications*, pp. K4–1–K4–5, 2007.

[5] A. F. Molisch, "Ultra-wide-band propagation channels," *Proceedings of the IEEE*, vol. 97, pp. 355–371, Feb. 2009.

[6] D. Cassioli, M. Z. Win, and A. F. Molisch, "The ultra-wide bandwidth indoor channel: from statistical model to simulations," *IEEE Journal on Selected Areas in Communications*, vol. 20, no. 6, pp. 1247–1257, 2002.

[7] S. Ghassemzadeh, L. Greenstein, T. Sveinsson, A. Kavcic, and V. Tarokh, "UWB delay profile models for residential and commercial indoor environments," *IEEE Transactions on Vehicular Technology*, vol. 54, pp. 1235–1244, July 2005.

[8] A. F. Molisch, J. R. Foerster, and M. Pendergrass, "Channel models for ultrawideband personal area networks," *IEEE Transactions on Wireless Communications*, vol. 10, pp. 14–21, Dec. 2003.

[9] A. F. Molisch, D. Cassioli, C.-C. Chong, S. Emami, A. Fort, B. Kannan, J. Karedal, J. Kunisch, H. G. Schantz, K. Siwiak, and M. Z. Win, "A comprehensive standardized model for ultrawideband propagation channels," *IEEE Transactions on Antennas and Propagation*, vol. 54, pp. 3151–3166, Nov. 2006.

[10] J. Kunisch and J. Pamp, "An ultra-wideband space-variant multipath indoor radio channel model," in *Proc. IEEE Conference on Ultra Wideband Systems and Technologies Digest of Technical Papers*, pp. 290–294, 2003.

[11] A. Domazetovic, L. J. Greenstein, N. B. Mandayam, and I. Seskar, "A new modeling approach for wireless channels with predictable path geometries," in *Proc. IEEE Vehicular Technology Conference (VTC'02–Fall)*, vol. 1, pp. 454–458, Sept. 2002.

[12] Y. Chen and V. Dubey, "An azimuth-frequency domain geometric model for ultrawide bandwidth signal propagation," in *Springer Wireless Personal Communications*, vol. 31, pp. 1–18, Oct. 2004.

[13] A. Papoulis and S. U. Pillai, *Probability, Random Variables and Stochastic Processes*. Mc Graw Hill, 4 ed., 2002.

[14] N. Czink, P. Cera, J. Salo, E. Bonek, J.-P. Nuutinen, and J. Ylitalo, "A framework for automatic clustering of parametric MIMO channel data including path powers," in *Proc. IEEE Vehicular Technology Conference (VTC'06–Fall)*, pp. 1–5, Sept. 2006.

[15] J. Fuhl, A. Molisch, and E. Bonek, "Unified channel model for mobile radio systems with smart antennas," in *IEE Proceedings Radar, Sonar and Navigation*, vol. 145, pp. 32–41, 1998.

[16] U. Schuster, H. Bolcskei, and G. Durisi, "Ultra-wideband channel modeling on the basis of information-theoretic criteria," *IEEE Transactions on Information Theory*, pp. 97–101, Sept. 2005.

[17] H. Akaike, "Likelihood of a model and information criteria," *Journal of Econometrics*, vol. 16, no. 1, pp. 3–14, 1981.

[18] T. Eltoft, T. Kim, and T.-W. Lee, "On the multivariate Laplace distribution," *IEEE Signal Processing Letters*, vol. 13, pp. 300–303, May 2006.

[19] A. F. Molisch, *Wireless Communications*. IEEE Press – Wiley, 2005.

[20] M. Steinbauer, A. F. Molisch, and E. Bonek, "The double-directional radio channel," *IEEE Antennas and Propagation Magazine*, vol. 43, no. 4, pp. 51–63, 2001.

[21] A. F. Molisch, H. Asplund, R. Heddergott, M. Steinbauer, and T. Zwick, "The COST259 directional channel model part I: Overview and methodology," *IEEE Transactions on Vehicular Communications*, vol. 5, pp. 3421–3433, Dec. 2006.

[22] H. Asplund, A. A. Glazunov, A. F. Molisch, K. I. Pedersen, and M. Steinbauer, "The COST259 directional channel model - part II: Macrocells," *IEEE Transactions on Wireless Communications*, vol. 5, no. 12, pp. 3434–3450, 2006.

[23] Y. Chen and V. K. Dubey, "Visibility of far clusters in directional mobile radio channels," *IEEE Communications Letters*, vol. 7, no. 9, pp. 422–424, 2003.

[24] A. Richter, *Estimation of Radio Channel Parameters: Models and Algorithms*. PhD thesis, Technische Universität Ilmenau, Ilmenau, 2005.

[25] L. J. Greenstein, V. Erceg, Y. S. Yeh, and M. V. Clark, "A new path-gain/delay-spread propagation model for digital cellular channels," *IEEE Transactions on Vehicular Technology*, vol. 46, no. 2, pp. 477–485, 1997.

[26] J. Cheng and N. Beaulieu, "Maximum-likelihood based estimation of the Nakagami m parameter," *IEEE Communications Letters*, vol. 5, no. 3, pp. 101–103, 2001.

[27] N. Balakrishnan and M. Kateri, "On the maximum likelihood estimation of parameters of Weibull distribution based on complete and censored data," *Statistics & Probability Letters*, vol. 78, no. 17, pp. 2971–2975, 2008.

[28] R. Qiu and I.-T. Lu, "Wideband wireless multipath channel modeling with path frequency dependence," in *Proc. IEEE International Conference on Communications*, vol. 1, pp. 277–281, 1996.

Paper III

Dielectric Characterization of Soil Samples by Microwave Measurements

Abstract

Northern high-latitude wetlands are well known to seasonally emit methane gas into the atmosphere, and therefore contribute to greenhouse effects. While these gas emissions are well documented, their causes are not well understood. The method described in this work can be used to analyze the changes happening in the soil during gas emissions, and therefore help the understanding of the sub-surface gas dynamics.

We have monitored a sample of peat soil through an artificial freezing and thawing cycle, using both a gas detector to measure the methane flux at the soil surface and a vector network analyzer to measure the transmission of microwaves through the soil. It was observed that the results from the two measurement approaches had a very good match under specific microwave signal conditions. In addition, from the microwave measured data, the dielectric properties of the soil and the volumetric fractions of its constituents were also calculated based on a dielectric mixing model.

T. Santos, Anders J. Johanson, and F. Tufvesson
"Dielectric Characterization of Soil Samples by Microwave Measurements,"
Series of Technical Reports, Department of Electrical and Information Technology,
Lund University, no. 10, ISSN 1402-8840, September, 2009.

1 Introduction

Methane (CH_4) is a natural atmospheric gas with the property of absorbing infra-red radiation. This property makes it a greenhouse gas, and in this category, methane is more than 20 times stronger than carbon dioxide (CO_2) [1]. In addition, following water vapor and carbon dioxide, methane is the most abundant greenhouse gas in the troposphere [2]. The methane present in the atmosphere is due to both human activity and natural causes, and the northern high-latitude wetlands contribute to 72% of all the natural methane emissions [2]. Concern is also given to the eventual thawing of the permafrost in these locations, and the consequent release of the carbon their deposited, since this could lead to a positive feedback effect on the global temperature.

The Zackenberg Ecological Research Operations (ZERO) research station at Zackenberg, Greenland, is located in such wetlands, and part of its activities include the monitoring of gas emissions from the soil. In 2007, besides the expected methane emissions during the spring, a large methane burst was also detected during the autumn, on the onset of freezing [3]. The integral of emissions during the freeze-in period was approximately equal to the amount of methane emitted during the entire summer season. This finding triggered new interest on the understanding of how the freezing/thawing processes influence gas emissions from the soil.

In this work, we aim to cast some light on the unknown gas dynamics happening within the soil before and during the gas emissions. In order to do so, we monitored a sample of peat soil while it was artificially frozen and thawed in a controlled laboratory environment. Our work is novel in that the monitoring was done both at the surface and at the sub-surface level, using two completely independent measurement techniques: methane flux measurements and microwave measurements, respectively. From the collected data, we calculated the bulk dielectric constant of the soil. The soil was then modeled as being composed of a *gas*, a *water* and a *solid* part, and the corresponding volumetric fractions were computed based on a dielectric mixing model.

The reminder of the paper is organized as follows. First, in Section 2 we present the background theory in which we base our calculations of the dielectric constant and volumetric fractions. In Section 3 we describe the measurement setup and give insight on how undesired diffraction and reflection effects can be minimized. In Section 4 we describe the post-processing applied to the data, and in Section 5 we present and discuss the measurement results. Lastly, in Section 6 we list the findings and propose future work.

2 Background Theory

2.1 Propagation Through a Dielectric Slab

In this work we analyzed the measurements of microwave signals transmitted through, and reflected from, a sample of soil. These effects can be well described mathematically by the expressions of transmission and reflection coefficients of an infinite dielectric slab [4, 5, 6]. For the case of a slab with length L, and considering free-space around the slab, the transmission coefficient is defined by

$$\mathrm{S}_{21}(f) = |\mathrm{S}_{21}(f)|\, e^{j\phi_{21}} = \frac{\left(1-R^2\right) e^{-\gamma L}}{1-R^2 e^{-2\gamma L}} \tag{1}$$

and the corresponding reflection coefficient is

$$\mathrm{S}_{11}(f) = |\mathrm{S}_{11}(f)|\, e^{j\phi_{11}} = \frac{\left(1-e^{-2\gamma L}\right) R}{1-R^2 e^{-2\gamma L}}. \tag{2}$$

where R is the field reflection coefficient (defined ahead). The propagation constant of the dielectric-filled slab γ, is defined in terms of the attenuation coefficient α and the phase factor β as

$$\gamma = \alpha + j\beta = \frac{2\pi}{\lambda_0}\sqrt{-\varepsilon_r} \tag{3}$$

where $\frac{2\pi}{\lambda_0} = k_0$ is the wavenumber in free space, λ_0 is the free space wavelength and ε_r is the relative complex dielectric permittivity of the sample which is composed by a real and imaginary part

$$\varepsilon_r = \varepsilon' - j\varepsilon''. \tag{4}$$

The real part ε' is related with the *propagation speed* as $v = c/\sqrt{\varepsilon'}$, where c is the speed of light in vacuum, whereas ε'' is related with the *attenuation* through the dielectric material. The relative complex dielectric permittivity[15] ε_r is related with the effective dielectric permittivity ε by

$$\varepsilon = \varepsilon_r \varepsilon_0, \tag{5}$$

[15] Throughout the rest of the paper we drop the words "relative complex" and refer to ε_r simply as "dielectric permittivity" or "dielectric constant."

where ε_0 is the dielectric constant in free space. From the above, ε' and ε'' can also be formulated as

$$\varepsilon' = \left(\frac{1}{k_0}\right)^2 \left[-\left(\alpha^2 - \beta^2\right)\right] \tag{6}$$

$$\varepsilon'' = \left(\frac{1}{k_0}\right)^2 (2\alpha\beta)\,. \tag{7}$$

The field reflection coefficient R is given in terms of Z_0, the intrinsic impedance of free space, and Z is the characteristic impedance of the dielectric-filled slab

$$R = \frac{Z - Z_0}{Z + Z_0}. \tag{8}$$

These impedances are given by

$$Z = \frac{j\omega\mu_0}{\gamma} = \frac{2\pi\eta_0}{\lambda_0} \cdot \frac{\beta\,(1 + j\alpha/\beta)}{\alpha^2 + \beta^2} \tag{9}$$

$$Z_0 = \mu_0 c = \sqrt{\frac{\mu_0}{\varepsilon_0}} \tag{10}$$

$$\mu_0 = 4\pi \times 10^{-7} \tag{11}$$

$$\varepsilon_0 = \frac{1}{\mu_0 c^2} \tag{12}$$

$$c = 2.9979 \times 10^8, \tag{13}$$

where $\omega = 2\pi f$ is the angular velocity at frequency f and μ_0 is the permeability of free space.

2.2 Dielectric Mixing Model

Soil samples such as peat are generally composed of different materials, e.g., earth, gases and water. Hence, the corresponding measured dielectric constant will be dependent on the electric properties of the different constituents. One way to describe the bulk (or total) dielectric constant is by using a so called *dielectric mixing model*. A well accepted mixing model is the one proposed by Lichtenecker [7]

$$\varepsilon_{\text{bulk}}^{\alpha} = \sum_i \Theta_i \varepsilon_i^{\alpha} \tag{14}$$

$$\sum_i \Theta_i = 1 \tag{15}$$

where ε_i is the dielectric constant of the i:th constituent and Θ_i is the corresponding volumetric fraction. The exponent α can range from -1 to 1, and defines the arrangement of the constituents to each other. The theoretical value of α for an homogeneous mixture is 0.5, which is the one used in this work. LichteneckerŠs mixture formulae (15) was originally derived in an empirical way, but was latter also derived theoretically [8].

2.3 Debye Theory of Dielectric Relaxation

Single materials are well described by the Debye theory of dielectric relaxation [9]. It assigns three parameters to each material, which describe how electric dipoles behave when excited by different frequencies

$$\varepsilon_r(w) = \varepsilon_\infty + \frac{\varepsilon_{\mathrm{dc}} - \varepsilon_\infty}{1 + jw\tau} - j\frac{\sigma}{w}. \tag{16}$$

$\varepsilon_{\mathrm{dc}}$ represents the static dielectric permittivity, ε_∞ is the permittivity at infinitely high frequencies and τ is the relaxation time of the material. The latter term, containing the electrical conductivity σ, can here be neglected since it diminishes at high frequencies. In this work, we use the Debye theory to describe the frequency dependent dielectric constant of water as is commonly done in the literature, e.g., [10]. The representation of both real and imaginary parts of the dielectric constant based on Debye theory are given in Fig. 1.

3 Measurement Setup and Equipment

The measurement campaign consisted in the monitoring of a sample of peat soil during freezing and thawing processes. A soil sample was collected from Fäjemyr, Skåne, Sweden (56°15′N, 13°33′E) and stored in a plastic container with dimensions 36×27×22 cm. The sampling site was chosen for its similarities with Greenland regarding soil properties. In addition, the height of the soil sample agrees with the height of the layer of soil above the permafrost in Zackenberg, Greenland. As a preparation for the experiment, the peat soil was incubated for a period of four weeks with a constant water level and in an anaerobic environment to ensure that considerable amount of methane was produced and stored in the soil. The container was then carefully transported to a temperature controlled room at the Department of Physical Geography and Ecosystem Analysis, Lund University. In order to induce the freezing process, a cooling device was placed on the top of the container to simulate the top-down natural freezing conditions. The measurement diagram is given in Fig. 2a and the corresponding photo in Fig. 2b. A methane detector was also placed above the soil to measure gas emissions.

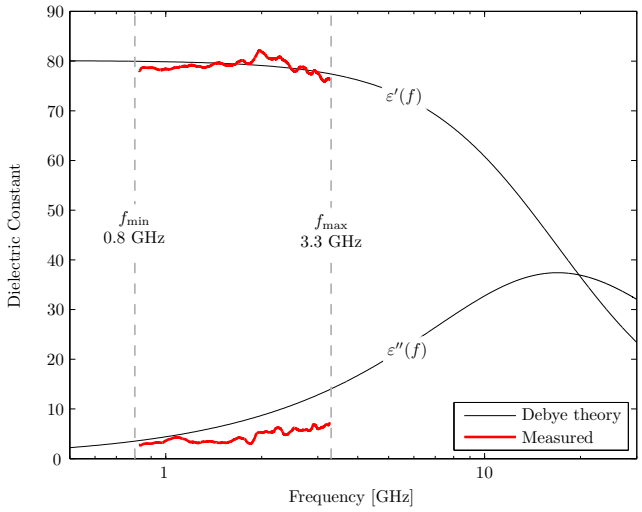

Figure 1: Theoretical and measured dielectric constant of water at 20° C.

Regarding the microwave part of the setup, the transmitter and receiver antennas were placed on the sides of the container, 5 cm away from the container's surface, and the surrounding volume was filled, as much as possible, with radiation absorber material,[16] see Fig. 2a. The measurements were done with a HP8720C vector network analyzer (VNA), which was set to measure the S_{21} and S_{11} parameters successively.

The VNA was configured to measure 1601 regularly spaced frequency points from 0.8 to 3.3 GHz. This frequency range was chosen as a compromise between the characteristics of the antennas, the amplifier and the soil. The intermediate frequency (IF) bandwidth was set to 1000 Hz. A UWB low noise amplifier (LNA), Mini-Circuits model ZVE-8G, with 28 dB of gain and noise figure of 3.5 dB, was connected between the receiver antenna and Port2 of the VNA. The VNA was controlled by a LabVIEW program running on a notebook computer. The antennas used were UWB SkyCross antennas, model SMT-2TO6MB-A.

Both the methane detector and the VNA were set to take one measurement per minute, during a total period of ten days. For the first two days the soil was maintained at room temperature, then the freezing phase was initiated by turning on the cooling device, and at the end of the seventh day, the thawing phase was started by taking the cooling device out of the measurement setup.

[16] Section 3.1 gives a detailed justification for the positioning of the antennas and the absorber material.

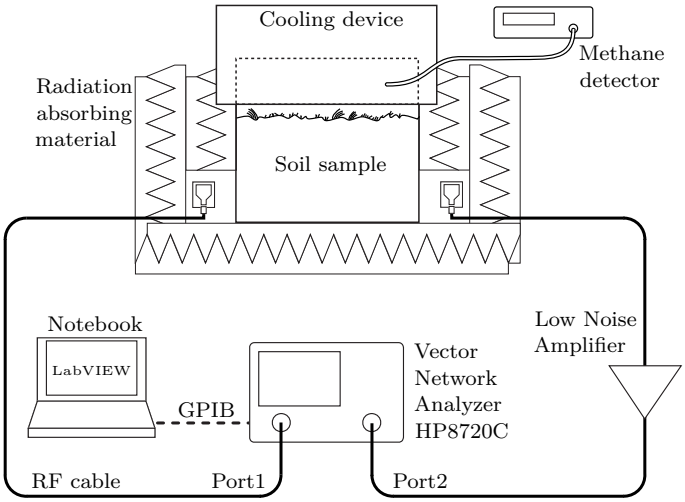

(a) Measurement diagram.

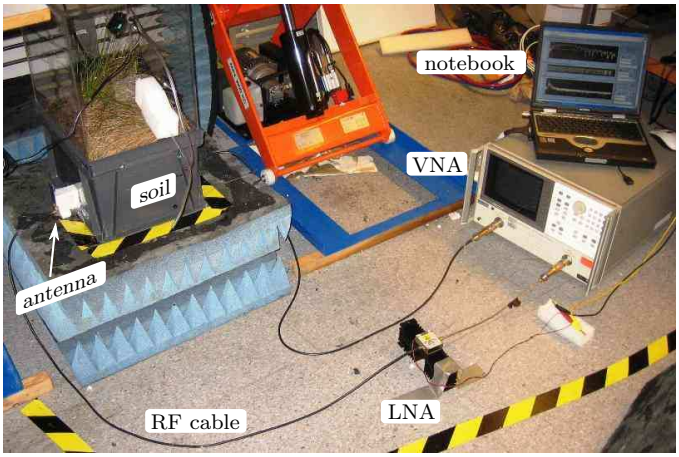

(b) Photo of the measurement setup.

Figure 2: Measurement diagram and corresponding photo at the temperature controlled room, Department of Physical Geography and Ecosystem Analysis, Lund University. Photo taken during the preparation for the measurements.

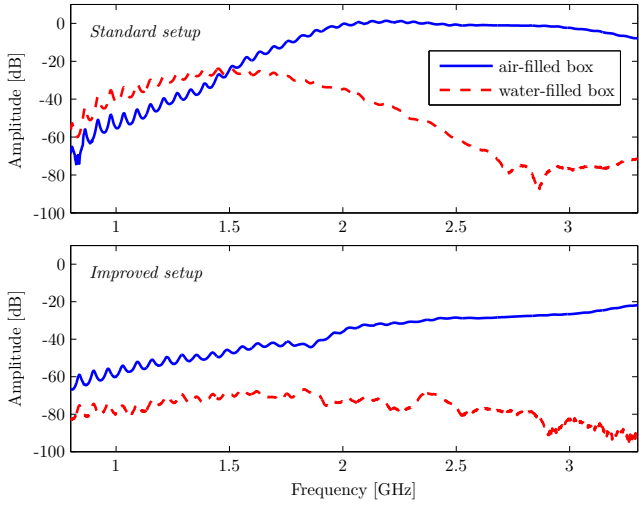

Figure 3: Uncalibrated S_{21} parameter values for standard (upper plot) and improved (lower plot) measurement setup .

3.1 Reducing Undesired Diffraction and Reflection Effects

In order to find the dielectric constant of the material, we assume that the measured S_{21} parameters are well modeled by the transmission equation (1). However, considering the size of our sample, this approximation is only true if the microwave signals arriving at the receiver antenna are only propagating in a straight line from the transmitter antenna, i.e., no additional components exist. In practice, this is impossible to achieve as diffraction components around the sample and reflection components from within the sample will always exist, these are illustrated in Fig. 4. In an effort to minimize these undesired effects we used the following measurement setup:

- Radiation absorbing material was placed on the sides of the plastic box to minimize the diffracted fields.
- The antennas were placed 5 cm away from the box, such that the waves propagating through the sample are more flat, i.e., less spherical, which reduces the strength of the reflection components on the sides of the container. In addition, the antenna mismatch was also reduced since the used antennas are designed for transmission in air.

A representation of the position of the absorbers and the antennas is given in Fig. 2a. In order to quantify the improvements, test measurements were per-

formed considering an empty box and water-filled box, see Fig. 3. From the upper plot, it is visible how strong the diffraction components are. For the lower frequencies, the transmission through water is larger than the transmission in free-space, which is physically impossible if not considering diffraction around the box. By applying the above referred modifications to the measurement setup, the diffracted and reflected fields were generally reduced. This reduction was more significant at the lower frequencies, e.g., at 1 GHz the power was reduced by 40 dB. The results shown in the lower plot of Fig. 3 are more acceptable: the transmission through water is always below transmission in free-space and the difference between the two lines increases with frequency, which agrees with the water property of increasing loss with increasing frequency.

4 Data Analysis and Post-Processing

4.1 Calibration

When transmission measurements are done through a sample, the recorded S_{21} parameter includes not only the influence of the sample under test but also the antenna distortions. To correct for this, the measured S_{21} must be calibrated.[17] A simple way to perform this calibration is to do it directly in the frequency domain by a division, as is done by [11],

$$\hat{S}_{21,\text{soil}}(f) = \frac{S_{21,\text{mea.}}(f)}{S_{21,\text{cal.}}(f)}. \tag{17}$$

It is important to note that calibrations performed directly by a division, are only valid under certain conditions. One condition is that the system must be linear and that the introduction of a certain material in the box must not generate additional propagation components, e.g., diffraction and reflection components, as represented in Fig. 4. This in often not the case as materials with $\varepsilon' > 1$ generate diffraction fields around the sample and create new reflected components from within the sample. To find the correction coefficients, $S_{21,\text{cal.}}(f)$, we started by measuring the transmission through an empty box, which contained all the referred non-linearities, $S_{21,\text{free-space}}(f)$. Ideally, $S_{21,\text{cal.}}(f)$ should be the transmission coefficient for when there is no sample at all, such that the antennas would have to be almost touching each other. This is not possible since the two antennas would stop behaving has good radiators due to the coupling between each other. So, our approach is to first measure the empty box (free space), and then "back-rotate" the phase of each one of the frequency points by an amount corresponding to the length of the

[17] Calibration is also referred to as "correction."

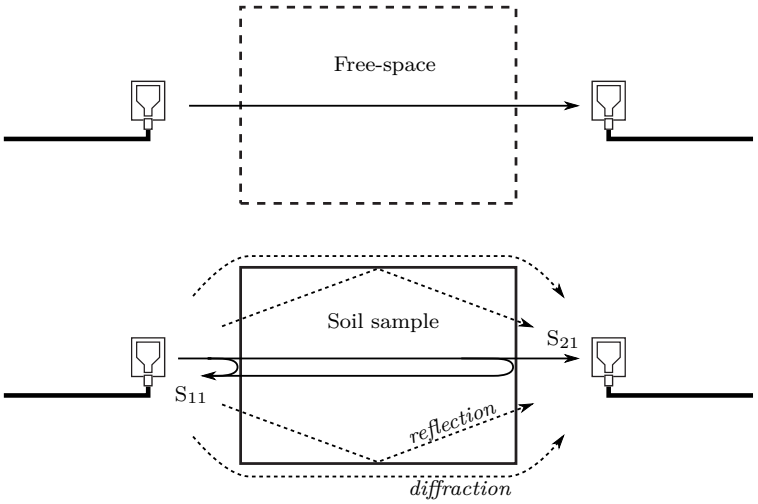

Figure 4: Calibration through free-space measurement. The indicated components, e.g., reflection and diffraction, represent the undesired propagation components.

box L, assuming propagation at the speed of light. In this way, we eliminate the influence of the unwanted free space within the box

$$\mathrm{S}_{21,\mathrm{cal.}}(f) = \mathrm{S}_{21,\text{free-space}}(f) \cdot e^{j2\pi Lf/c} \tag{18}$$

$$= \mathrm{S}_{21,\text{free-space}}(f) \cdot e^{jw\tau_0}. \tag{19}$$

where τ_0 is the propagation delay corresponding to a wave traveling at the speed of light through a length of L. This approach also solves an additional problem. The assumption in equation (1) is that the wave impinging on the slab is plane, or lossless, which is not our case since the waves radiated by the antennas are spherical, and therefore lossy. However, the same spherical loss is also measured in $\mathrm{S}_{21,\text{free-space}}(f)$, and will therefore be compensated in (17).

It is important to refer that the above described calibration does not replace the internal calibration of the VNA, which corrects for the equipment's internal errors and non-linearities [12]. However, the internal calibration of the VNA is not sufficient since it is not able to correct for the antenna distortions.

4.2 Calculation of the Dielectric Parts ε' and ε''

The calculation of the dielectric constant is not trivial because there is no direct relation between ε' or ε'', and the measured S_{21} parameter. One approach

is to use numerical methods. Several iterative numerical methods have been proposed in the literature, in [4] an iterative algorithm based on (6) and (7) is proposed. The drawback of such algorithms is generally the uncertainty off the convergence to the correct solution, which is usually dependent on the initial values. The non-unique solution, i.e., the fact that several values of ε' and ε'' verify (1) and (2), stems from the repetitive nature of a sinusoidal wave.

Our approach is based on an exhaustive error minimization search over the values of ε' and ε''. We start by defining the frequency dependent error function as

$$E(f) = \left| \hat{\mathrm{S}}_{21,\mathrm{soil}}(f) - \frac{\left(1-R^2\right) e^{-\gamma L}}{1 - R^2 e^{-2\gamma L}} \right|^2 . \tag{20}$$

The corresponding minimization problem is formulated as

$$\{\varepsilon'(f), \varepsilon''(f)\} = \underset{\{\varepsilon', \varepsilon''\}}{\arg\min}\, E(f). \tag{21}$$

As mentioned earlier, the solution to (21) is not unique. However, the values of $\varepsilon'(f)$ and $\varepsilon''(f)$ are not expected to change significantly within small frequency bands. We can therefore use the frequency domain to narrow down the number of possible solutions by

$$\{\varepsilon'(f_c), \varepsilon''(f_c)\} = \underset{\{\varepsilon', \varepsilon''\}}{\arg\min} \int_{f_c - B/2}^{f_c + B/2} E(f) df \tag{22}$$

where B is the band around the center frequency f_c. Since the measured data is restricted to discrete frequency points, we can reformulate (22) with a frequency discrete basis

$$\{\varepsilon'(f_i), \varepsilon''(f_i)\} = \underset{\{\varepsilon', \varepsilon''\}}{\arg\min} \sum_{i=-N_f/2}^{N_f/2} E(f_{i+n}), \tag{23}$$

where f_i refers to the i:th measured frequency and N_f is the number of consecutive frequencies. In the analysis of the data, N_f was set to 20, which corresponded to a bandwidth of roughly 30 MHz. This bandwidth is acceptable since all soil constituents are expected to have constant dielectric properties within 30 MHz. Even water, the constituent varying the most with frequency, satisfies this condition. Fig. 5 shows the logarithmic error surface based on (22) for both 0.8 and 3.3 GHz when the soil sample was at a temperature below 0°C. It is visible from the figure how challenging it is to choose the correct solution[18] for the higher frequencies since the number of solutions increases with

[18]Each possible solution is identified by a "valley" on the error surface, since a "valley" corresponds to the area where the error is minimal.

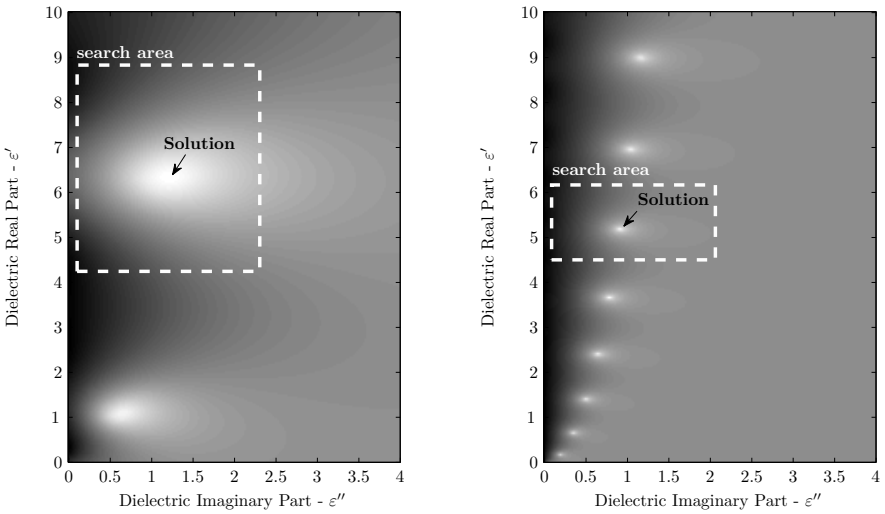

(a) Frequency: 0.8 GHz **(b)** Frequency: 3.3 GHz

Figure 5: Logarithm of error surface for a soil sample at a temperature below 0°C. The dashed rectangles indicate the grid search area.

increasing frequency. This property is caused by the fact that the amount of phase rotation increases with increasing frequency, when considering the same propagation length.

Our approach to calculate ε' and ε'' for the whole frequency band is the following. First, we find the impulse response of the measured data by means of the IFFT operation. Then, we find the delay, τ_{peak}, corresponding to the strongest peak of the impulse response, and calculate an estimate of ε' by

$$\hat{\varepsilon}' = \left(\frac{c\tau_{\text{peak}}}{L}\right)^2 \tag{24}$$

where c is the speed of light in vacuum. Subsequently, using the error surface corresponding to the lowest frequency, f_1, we find the solution that is closer to $\hat{\varepsilon}'$ by a grid search using (23). For the example shown in Fig. 5a, f_1 is 0.8 GHz and the calculated solution is $\varepsilon'(f_1) = 6.3$ and $\varepsilon''(f_1) = 1.2$. The size of the grid search is depicted in the figure by the dashed rectangle. We then use this solution as a starting point to the calculation of the dielectric constant of the next frequency point, more specifically, the solution of a given frequency

becomes the center of the grid search of the next frequency

$$\underset{\text{grid center}}{(\varepsilon'(f_n), \varepsilon''(f_n))} = (\varepsilon'(f_{n-1}), \varepsilon''(f_{n-1}))\,, \quad n > 1. \tag{25}$$

In this way, the solution is tracked until the last frequency point, see Fig. 5b. Since the distance between the adjacent solutions decreases with increasing frequency, the size of the grid search is reduced accordingly, so that only one solution exists within a given grid. In this work, the resolution of the grid search was chosen to ensure an error below 10^{-3} for both ε'' and ε'.

To verify the accuracy of the above described method, measurements were performed with pure water and the calculated dielectric constants were compared with the expected ones based on Debye theory, the results are given in Fig. 1. The deviation between calculated and theoretical curves, appears to increase with increasing frequency for the case of ε'', which indicates that, with the present measurement setup, the calculated results might be underestimating ε'' for the higher frequencies. Nevertheless, the calculations of ε' show a good match with theory.

4.3 Dielectric Properties of the Constituent Materials

For the considerations regarding the dielectric properties of the constituent materials, we follow the reasoning presented in [13]. In brief, we model the soil samples by three constituents: *gas*, *water* and *solid*, such that the corresponding volumetric fractions verify

$$\underset{\text{gas}}{\Theta_1} + \underset{\text{water}}{\Theta_2} + \underset{\text{solid}}{\Theta_3} = 1, \quad \Theta_1, \Theta_2, \Theta_3 \geq 0. \tag{26}$$

4.4 Calculation of the Volumetric Fractions

The aim of this work is ultimately to find the value of these three parameters for every time instant.[19] In order to find the three volumetric fractions, we make use of the calculated dielectric constants together with the mixing model described in section 2.2, such that

$$\sqrt{\varepsilon_{\text{calc.}}} = \Theta_1\sqrt{\varepsilon_1} + \Theta_2\sqrt{\varepsilon_2} + \Theta_3\sqrt{\varepsilon_3} \tag{27}$$

where $\varepsilon_{\text{calc.}} = \varepsilon' - j\varepsilon''$ denotes the dielectric constant calculated from the method described in Section 4.2. The values chosen for ε_1, ε_2 and ε_3 are given in Table 1, and the corresponding justification is provided in [13]. Considering Eq. (26), together with the fact that Eq. (27) is complex and therefore needs to

[19] The time dependence is not shown in the formulations for clarity.

Table 1: Considered dielectric permittivities of the three soil constituents.

	ε_1 gas	ε_2 water	ε_3 solid
ε'	1	Debye (16)	3.150
ε''	0	Debye (16)	0.005

be valid independently for the real and imaginary parts, we arrive at a system of three equations

$$\mathrm{Re}\left\{\sqrt{\varepsilon_{\mathrm{calc.}}}\right\} = \mathrm{Re}\left\{\Theta_1\sqrt{\varepsilon_1} + \Theta_2\sqrt{\varepsilon_2} + \Theta_3\sqrt{\varepsilon_3}\right\} \tag{28}$$

$$\mathrm{Im}\left\{\sqrt{\varepsilon_{\mathrm{calc.}}}\right\} = \mathrm{Im}\left\{\Theta_1\sqrt{\varepsilon_1} + \Theta_2\sqrt{\varepsilon_2} + \Theta_3\sqrt{\varepsilon_3}\right\} \tag{29}$$

$$1 = \Theta_1 + \Theta_2 + \Theta_3 \tag{30}$$

from which the three unknowns Θ_1, Θ_2 and Θ_3 can be calculated.

However, the calculation of the volumetric fractions is not straightforward since the above system of equations is non-linear. Following the same approach used for the calculation of ε' and ε'' in Section 4.2, we avoid iterative methods and estimate the three unknowns by means of a fine grid search. By replacing (30) on (28) and (29), the problem can be simplified to a two-dimensional grid search.

5 Results

5.1 Frequency and Time Domain Profiles

The complete data measured by the VNA, after calibration, is illustrated in Fig. 6, in the frequency-domain, and in Fig. 7, in the time-domain.

It is difficult to find an explanation for each and every amplitude variation seen in the figures, however, several general observations can be made. From Fig. 6, at the beginning of the experiment (day zero), when the water was in the liquid state, the amplitude of the transmission decays with increasing frequency. This property is well in line with the predictions from the Debye model for water. Then, during the freezing phase, while the liquid water was progressively being transformed into solid ice, the higher frequencies progressively became less attenuated (at 3.3 GHz, from day two to day eight, there is an increase in received power of 40 dB). On the other hand, the attenuation of the lower frequencies (e.g., 0.8 GHz) barely changes during the six days of freezing, which also agrees with the Debye model. On the onset of the thawing phase, there is an increase in the volumetric content of liquid water, and the transmission coefficient naturally decreases.

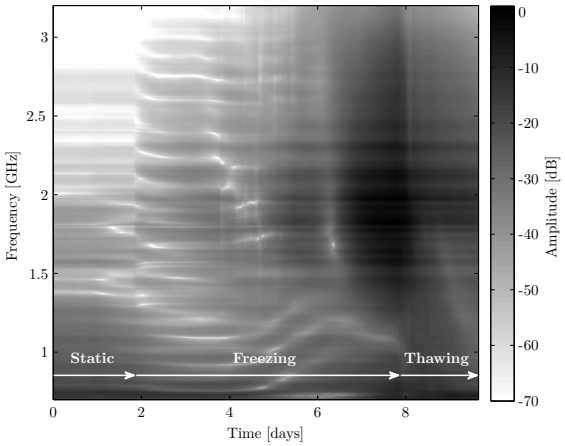

Figure 6: Measured S_{21} parameter after calibration, for the full ten days of measurements.

The data presented in Fig. 7, results from applying the IFFT operation to the calibrated S_{21} parameter, and in the figure, there are two aspects worth mentioning: 1) As indicated by the two arrows, the first strong component of the impulse response appears at 8 ns before freezing and at 2 ns after freezing. This indicates that at the start of the measurements, the transmitted pulse[20] propagates mainly through liquid water, and that at day eight the propagation is made mainly through ice. It is also notable that around day four, there are two arriving components with comparable amplitude at delays 3 ns and 8 ns, which point to the fact that, at this instant, there were two separable layers in the soil: a top-frozen layer and a bottom-unfrozen one. 2) Between day six and day eight, a train of amplitude decreasing pulses is visible along the delay domain. This supports the idea that the received power is not only due to one component that propagates through the soil once, but also due to later propagation components which are reflected multiple times from within the soil. This is a characteristic of dielectric slabs with low ε'', as is the case of ice.

[20]By "pulse," we refer to the virtual time-domain "sinc" pulse composed of all the transmitted frequencies.

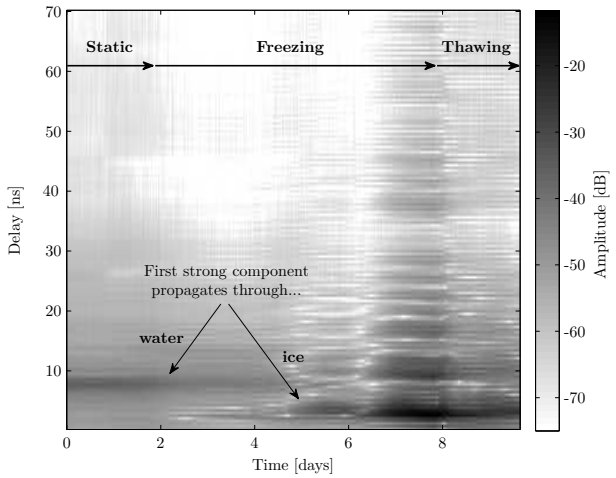

Figure 7: Impulse response (through IFFT) of the measured S_{21} parameter after calibration, for the full ten days of measurements.

5.2 Amplitude and Phase Variations versus Methane Emissions

Regarding methane emissions, these were only detected during the thawing phase, and therefore we now focus our attention to the results from day 7.6 to day 8.6. From Figs. 6 and 7, the amplitude variations in this period appear very smooth. However, when looking with more detail, several sharp small-scale variations (< 1 dB) are visible, see Fig. 8a. These sharp variations are both positive, i.e., increase of amplitude, and negative, i.e., decrease of amplitude. The phase of S_{21} shows similar variations as shown in Fig. 8b.

To better understand the relation between the variations of both the amplitude and phase with the emissions of methane, we plot their time derivatives together for comparison, see Fig. 9. A peak in the derivative of the methane flux, corresponds to a burst emission of methane from the soil sample. These derivatives were computed numerically by the approximation

$$\frac{d}{dt}s(t_n) \approx \frac{s(t_n) - s(t_{n-1})}{t_n - t_{n-1}} \tag{31}$$

where $s(t_n)$ denotes a time dependent function sampled at time instant t_n. In our case, the sampling interval, $t_n - t_{n-1}$ was one minute. To facilitate the

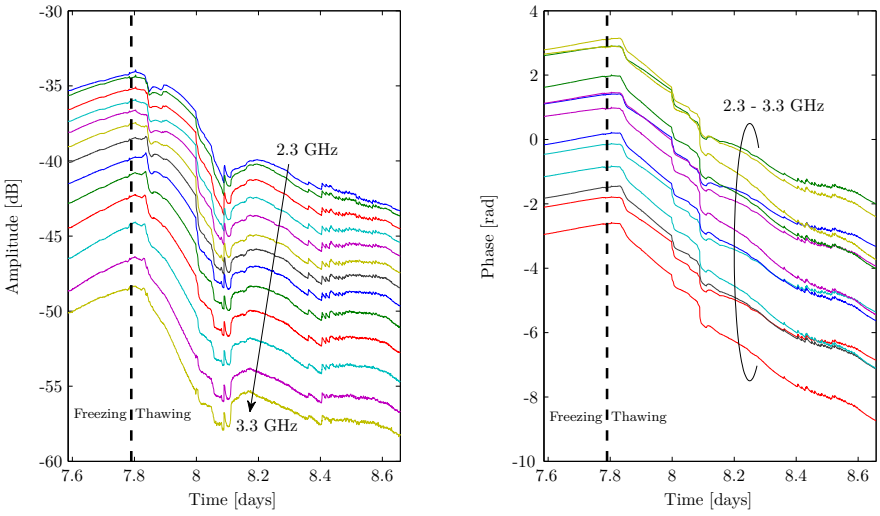

(a) S_{21} amplitude. **(b)** S_{21} phase.

Figure 8: Measured (uncalibrated) S_{21} parameter between the seventh and eighth day. The vertical dashed line indicates the time instant when the thawing phase was initiated. For clarity the figure only shows the frequency band from 2.3 to 3.3 GHz.

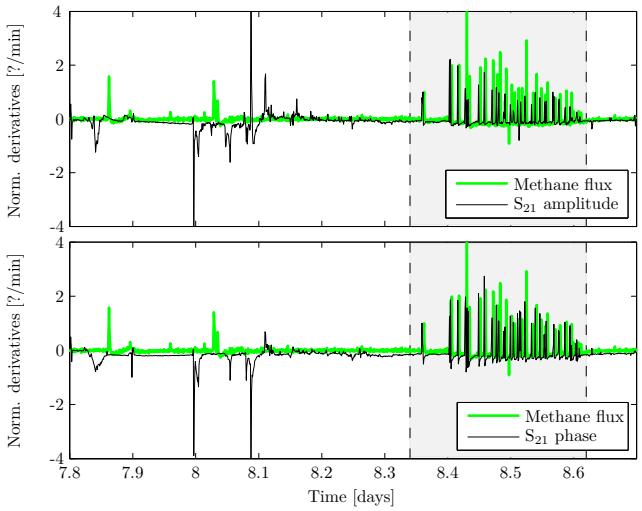

Figure 9: Normalized derivatives of both amplitude and phase of the S_{21} parameter compared against the derivative of methane flux versus time. The normalization was made in relation to the amplitude of the peak at 8.36 days. The shaded area indicates the time window during which the results from the two measurement techniques matched.

comparison, the curves were normalized to the peak amplitude at time instant 8.36 days. The derivatives in both subplots do not show a perfect match, some peaks appear to match well while others don't match at all. However, a more careful observation reveals an interesting characteristic:

at all the instants when both the amplitude and the phase increase, the methane flux at the surface also increases.

The shaded area in Fig. 9, indicates the time window during which the match between the two measurements techniques was very good. Fig. 10, shows the initial part of that time window in detail, for both amplitude and phase. There is also a visible delay of roughly two minutes between the two curves.[21]

It should be noted that a perfect match between the results of the two measurement devices was not expected since these were not measuring the

[21] At the time of the measurements, it was not possible to verify whether this delay was caused by the soil itself (a delay between a change in the lower layers of the soil, and the emission of methane at the surface), or if it was caused by a mismatch between the clock of the computer storing the S_{21} parameter and the clock of the computer storing the methane flux.

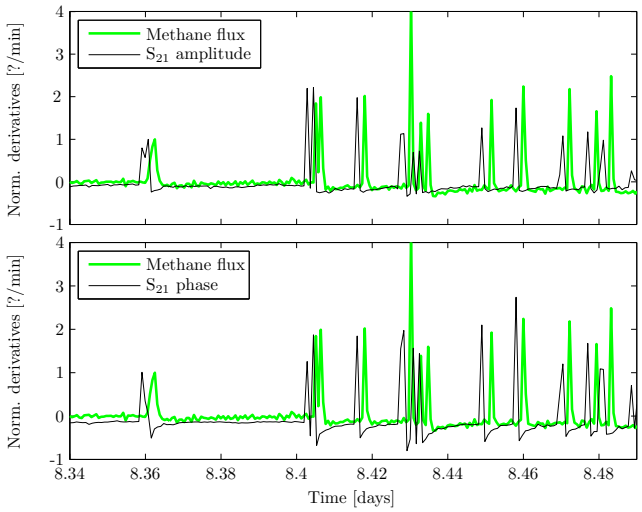

Figure 10: Normalized derivatives of both amplitude and phase of the S_{21} parameter compared against the derivative of methane flux versus time. The time between consecutive samples is one minute.

same physical volume. The VNA was measuring the transmission through the soil sample at a sub-surface level, and the methane detector was measuring the gas flux at the surface. Therefore, properties within the sample might change without resulting in any gas emission at the surface.

5.3 Volumetric Fractions and their Interpretation

Finally, we applied the method described in Section 4.2, to calculate the dielectric constant of all the frequencies for the different time instants. The corresponding volumetric fractions were calculated based on the formulations given in Section 4.4.

Fig. 11 shows the calculated volumetric fractions versus time. The two small subplots give a detail of the volumetric fraction of the solid and gas parts, for the time window when there was a good match between the derivative curves (i.e., the time window of Fig. 10). By comparing the time instants of the methane emissions with the calculated volumetric fractions, it is evident that each emission is characterized by a drop in the content of gas and corresponding increase in the content of the solid part. Furthermore, after each emission, the gas content within the soil appears to slowly increase with time until the

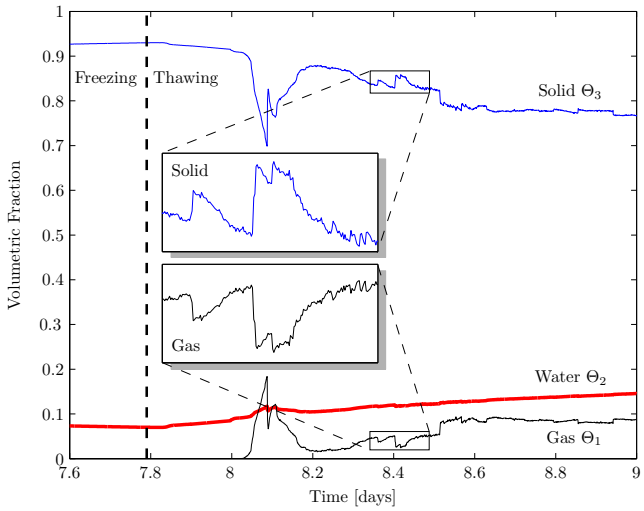

Figure 11: Calculated volumetric fractions as a function of time at 2.28 GHz. The detail plots are given for the same time window as Fig. 10, from day 8.34 to day 8.49.

next abrupt drop, or gas emission. One possible interpretation for these results is that, due to the depressure caused by the melting of the ice, the methane is allowed to move within the soil, where it accumulates in localized air pockets, until a channel to the surface becomes available, triggering the methane emission. It is however important to be careful when interpreting these results, since these are only taken from a single experiment.

6 Conclusions and Future Work

In this work we have performed a laboratory experiment on a sample of peat soil, where the temperature was controlled to induce freezing, and subsequently thawing, in a sample of peat soil. The aim was to simulate the yearly temperature changes experienced by the soil in Greenland at the onset of the autumn and spring, respectively. The microwave and methane measurements showed a good correlation during the time when both the amplitude and phase of the transmission coefficients had a positive derivative. This finding, if proven to be consistent and repeatable, might lead to the design of new techniques to detect gas bursts. In addition, we have described a method to calculate the bulk dielectric permittivity of the soil, and the volumetric fractions of the soil

constituents based on a mixing model. This is valuable information for the geology experts aiming to understand the mechanisms that trigger the emissions of methane from the soil.

While these results are very promising, there is still a lot of room for improvement. The improvements can be made at several levels, e.g., measurement setup, measurement equipment, algorithms for data analysis and modeling assumptions. In the list below, we specify some topics which can be the basis of future work:

- Our method to calculate the dielectric constant was shown to underestimate the attenuation (i.e., the imaginary part ε'') when measuring pure water, cf. Fig 1. Hence, new methods can be developed, and these should be also validated against materials with well known dielectric properties such as water. In this topic, the approach used in [11] should also be taken into account.

- In this work we only make use of the transmission coefficients, Eq. (1). The reflection coefficients, Eq. (2), also carry valuable information which can be included in the calculations of the dielectric constant.

- The method to calculate the dielectric constant can be further improved by using the information of the whole bandwidth simultaneously, instead of dividing the bandwidth in small sub-bands.

- The processing time of the presented results was rather long since the calculations were based on grid searches, and these are very heavy computationally. However, since the error surface within the considered bounds is convex, see Fig. 5, it should be possible to use iterative algorithms that converge to the solution within these bounds.

The findings of this work have prompted an immediate interest for future work by the all the participants. As a result of that, new spiral antennas have already been designed specially for the propagation in high permittivity mediums as wet soils, and a complete soil monitoring system has been created and transported to Zackenberg, Greenland, where it will be measuring real soil samples from September to November 2009, during the onset of freezing. The study of the data collected in Greenland will be the natural extension of this work. A recent photo of Zackenberg Valley showing the designed antennas buried in the soil and the microwave measurement device, is given in Fig. 12.

Figure 12: Photo of Zackenberg Valley in Greenland, taken on August 25th, 2009. The microwave measurement device is a Rohde&Schwarz FSH4 Handheld Network Analyzer.

Acknowledgements

The help of Norbert Pirk, Mikhail Mastepanov and Torben R. Christensen from the Department of Physical Geography and Ecosystem Analysis, Lund University, is greatly appreciated, both during the measurements and during the analysis of the data. The initial idea to use microwave measurements was Norbert's. We also thank LUNARC, the center for scientific and technical computing for research at Lund University, for providing the vital access to their cluster of computers. This work was financially supported, in part, by the Swedish Strategic Research Foundation (SSF) Center of High Speed Wireless Communications (HSWC) at Lund University and by the Swedish Vetenskapsrådet.

References

[1] O. A. Anisimov, "Potential feedback of thawing permafrost to the global climate system through methane emission," *Environmental Research Letters*, vol. 2, Nov. 2007.

[2] D. J. Wuebbles and K. Hayhoe, "Atmospheric methane and global change," *Earth-Science Reviews*, vol. 57, pp. 177 – 210, May 2002.

[3] M. Mastepanov, C. Sigsgaard, E. J. Dlugokencky, S. Houweling, L. Ström, M. P. Tamstorf, and T. R. Christensen, "Large tundra methane burst during onset of freezing," *Nature*, vol. 456, pp. 628–630, Dec. 2008.

[4] M. T. Hallikainen, F. T. Ulaby, M. C. Dobson, M. A. El-Rayes, and L.-K. Wu, "Microwave dielectric behavior of wet soil – part I: Empirical models and experimental observations," *IEEE Transactions on Geoscience and Remote Sensing*, vol. GE-23, pp. 25–34, Jan. 1985.

[5] E. H. Kansson, A. Amiet, and A. Kaynak, "Dielectric characterization of conducting textiles using free space transmission measurements: Accuracy and methods for improvement," *Synthetic Metals*, vol. 157, pp. 1054 – 1063, Dec. 2007.

[6] A. M. Nicolson and G. F. Ross, "Measurement of the intrinsic properties of materials by time-domain techniques," *IEEE Transactions on Instrumentation and Measurement*, vol. 19, pp. 377–382, Nov. 1970.

[7] K. Lichtenecker, "Dielectric constant of natural and synthetic mixtures," *Phys. Z*, 1926.

[8] Z. Tarik, L. Jean-Paul, and V. Michel, "Theoretical evidence for 'Lichtenecker's mixture formulae' based on the effective medium theory," *Journal of Physics D: Applied Physics*, vol. 31, no. 13, pp. 1589–1594, 1998.

[9] P. Debye, *Polar Molecules*. Chemical Catalog Co. New York; reprinted by Dover, New York, 1954, 1929.

[10] J. O. Curtis, "A durable laboratory apparatus for the measurement of soil dielectric properties," *IEEE Transactions on Instrumentation and Measurement*, vol. 50, pp. 1364–1369, Oct. 2001.

[11] A. Muqaibel, A. Safaai-Jazi, A. Bayram, and S. Riad, "Ultra wideband material characterization for indoor propagation," in *IEEE Antennas and Propagation Society International Symposium*, vol. 4, pp. 623–626, June 2003.

[12] D. Ballo, "Network analyzer basics – Back to basics seminar." Hewlett-Packard, 1998.

[13] N. Pirk, "Methane emission peaks from permafrost environments: Using ultra-wideband spectroscopy, sub-surface pressure sensing and finite element solving as means of their exploration," Master's thesis, Department of Physical Geography and Ecosystems Analysis, Lund University, June 2009.